Pressure-temperature-deformation-time (P-T-d-t) exhumation history of the Voltri Massif HP complex, Ligurian Alps, Italy

Gianluca Vignaroli,[1] Federico Rossetti,[1] Daniela Rubatto,[2] Thomas Theye,[3] Frank Lisker,[4] and David Phillips[5]

Received 8 October 2009; revised 22 June 2010; accepted 21 July 2010; published 10 December 2010.

[1] An integrated structural, petrological, and geochronological/thermochronological study was undertaken to constrain the tectonic controls on the exhumation of the Voltri Massif high-pressure (HP) complex, located in the Ligurian portion of the Western Alps (Italy). Petrotextural analyses were performed to identify the pressure-temperature interval of (1) peak metamorphism (the D_1-M_1 stage) to eclogitic/blueschist facies conditions and (2) the main retrogressive event (the D_2-M_2 stage) to greenschist facies conditions. U-Pb SHRIMP dating on a zircon rim (33.8 ± 0.8 Ma) and titanite grains (29 ± 5 Ma), coupled with ^{40}Ar-^{39}Ar analyses on phengite (~64 Ma to ~34 Ma) placed temporal constraints on the exhumation path from the D_1-M_1 to the D_2-M_2 stages at the Eocene-Oligocene boundary. Apatite fission track thermochronology, with older ages of 23.9 ± 4.9 Ma, confirms the existence of a regional, Late Oligocene to Miocene cooling/exhumation event for the Voltri Massif (the D_3-M_3 stage). The compilation of this pressure-temperature-deformation-time path supports a change in the exhumation history: (1) an initial stage, from the D_1-M_1 to the D_2-M_2, which was nearly isothermal with highly variable exhumation rates, and (2) a second stage, from D_2-M_2 to upper crustal levels, which was accomplished by cooling and moderate exhumation rates of ~1–2 mm yr^{-1}. This two-stage path can be reconciled with the dominant tectonic mechanisms responsible for exhumation of HP rocks in the Voltri Massif area. At the regional scale, this path is consistent with major geodynamic reorganization in the Mediterranean region at the Eocene-Oligocene time boundary, which involved a switch from synorogenic events during transpressive kinematics at the Alpine-Apennine plate boundaries, to postorogenic processes related to crustal thinning and opening of back-arc basins. **Citation:** Vignaroli, G., F. Rossetti, D. Rubatto, T. Theye, F. Lisker, and D. Phillips (2010), Pressure-temperature-deformation-time (P-T-d-t) exhumation history of the Voltri Massif HP complex, Ligurian Alps, Italy, *Tectonics*, *29*, TC6009, doi:10.1029/2009TC002621.

1. Introduction

[2] The exposure of high-pressure (HP) metamorphic suites in orogenic domains implies exhumation from deep-seated crustal levels at convergent plate margins. Whereas HP metamorphism is generally considered to be related to progressive burial during ongoing subduction, exhumation processes involved in bringing these rocks to surface are somewhat controversial and can be grouped into two main end-member mechanisms: (1) shortening and thrust faulting concomitant with erosion at the surface [*Platt*, 1993; *Stüwe and Barr*, 1998] during underplating in a subduction channel [e.g., *Cloos*, 1982; *Chemenda et al.*, 1995; *Burov et al.*, 2001; *Gerya et al.*, 2002] and (2) removal of the overburden produced by extensional detachment tectonics during synorogenic to postorogenic processes [*Platt*, 1986; *Jolivet et al.*, 1998]. The ongoing debate surrounding this issue mainly stems from the wide range of metamorphic peak conditions, timing, and rates of exhumation documented for paleosubduction environments [e.g., *Ernst*, 1988; *Platt*, 1993; *Jolivet et al.*, 1998, 2003; *Ring et al.*, 1999; *Agard et al.*, 2009].

[3] Reconstruction of the pressure-temperature-deformation-time (P-T-d-t) paths of exhumed HP domains is a prerequisite for constructing plausible geodynamic and tectonic scenarios for the mechanism(s) and processes leading to deep-seated rock exhumation in orogenic domains. A P-T-d-t path involves assigning an absolute age to a specific tectonic event by linking crystallization ages for specific minerals to a specific rock fabric, in addition to mineral thermobarometry [e.g., *Monié et al.*, 1991; *Agard et al.*, 2002; *Challandes et al.*, 2003; *Augier et al.*, 2005]. A multidisciplinary approach is necessary because of (1) the ambiguity in correlating ages with mineral crystallization events in a poly metamorphic fabric [e.g., *Vernon*, 1996; *Vavra et al.*, 1999; *Harley et al.*, 2007], (2) questions relating to the validity of isotopic parameters, such as the closure temperature concept [e.g., *Dodson*, 1973; *Villa*, 1998], and (3) the occurrence of external factors affecting the geochronological results (e.g., the gain or loss of isotopic components in presence of fluid phase [e.g., *Geisler et al.*, 2007]).

[1] Dipartimento di Scienze Geologiche, Università Roma Tre, Rome, Italy.
[2] Research School of Earth Sciences, Australian National University, Canberra, ACT, Australia.
[3] Institut für Mineralogie und Kristallchemie, Universität Stuttgart, Stuttgart, Germany.
[4] Fachbereich Geowissenschaften, University of Bremen, Bremen, Germany.
[5] School of Earth Sciences, University of Melbourne, Parkville, Victoria, Australia.

0278-7407/10/2009TC002621

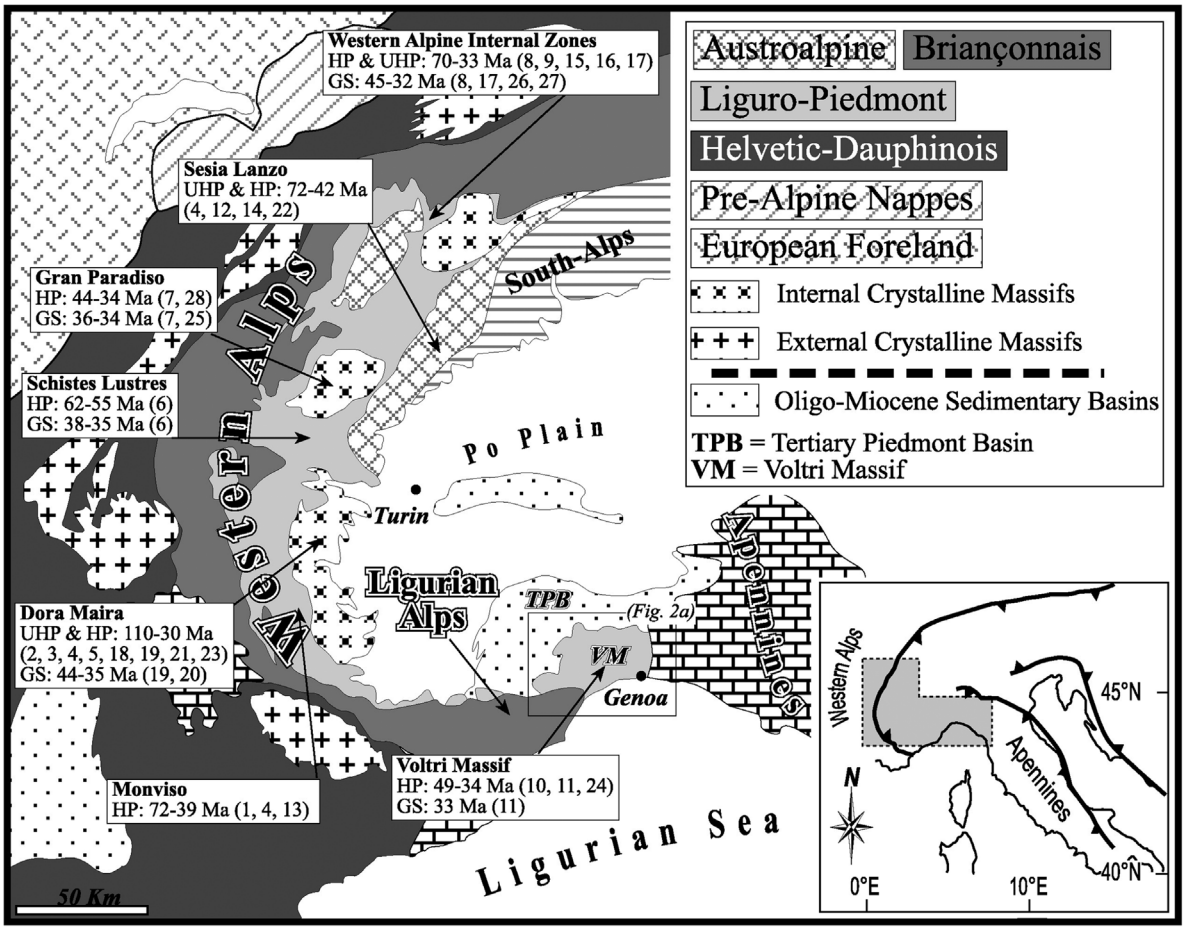

Figure 1. Geological map of the Western Alps with a compilation of published geochronological data showing a partial temporal overlap (at the Late Eocene-Early Oligocene boundary) existing between ages attributed to (U)HP metamorphism and ages attributed to the retrogressive metamorphism during exhumation [after *Agard et al.*, 2002; *Meffan-Main et al.*, 2004]. VM, Voltri Massif; TPB, Tertiary Piedmont Basin. Numbers refer to the following: 1, *Cliff et al.* [1998]; 2, *Tilton et al.* [1991]; 3, *Gebauer et al.* [1997]; 4, *Duchêne et al.* [1997]; 5, *Rubatto and Hermann* [2001]; 6, *Agard et al.* [2002]; 7, *Meffan-Main et al.* [2004]; 8, *Amato et al.* [1999]; 9, *Rubatto et al.* [1998]; 10, *Rubatto and Scambelluri* [2003]; 11, *Federico et al.* [2005]; 12, *Inger et al.* [1996]; 13, *Rubatto and Hermann* [2003]; 14, *Rubatto et al.* [1999]; 15, *Bowtell et al.* [1994]; 16, *Reddy et al.* [1999]; 17, *Cartwright and Barnicoat* [2002]; 18, *Paquette et al.* [1989]; 19, *Monié and Chopin* [1991]; 20, *Scaillet et al.* [1990]; 21, *Scaillet et al.* [1992]; 22, *Dal Piaz et al.* [2001]; 23, *Di Vincenzo et al.* [2006]; 24, *Federico et al.* [2007b]; 25, *Freeman et al.* [1997]; 26, *Reddy et al.* [2003]; 27, *Markley et al.* [1998]; 28, *Gabudianu Radulescu et al.* [2009].

[4] The Western Alps (Figure 1) represent an important natural laboratory to test modes of deep-seated rock exhumation in paleosubduction environments. The exhumed roots of the Western Alps were variably equilibrated at both ultra-HP [e.g., *Chopin*, 1984; *Reinecke*, 1998; *Rubatto and Hermann*, 2001] and eclogitic [e.g., *Messiga et al.*, 1983; *Schwartz et al.*, 2000; *Cartwright and Barnicoat*, 2002] peak conditions. In addition, a widespread retrograde greenschist facies metamorphic overprint accompanied the exhumation path [e.g., *Messiga and Scambelluri*, 1991; *Barnicoat et al.*, 1995; *Agard et al.*, 2002; *Reddy et al.*, 2003]. The wealth of available geochronological data, although somewhat heterogeneous and based on different dating techniques, suggests an overall younging of the orogenic belt from the external (Africa-derived units) to the internal (Europe-derived units) sector of the Alpine chain (see *Rosenbaum and Lister* [2005] for a review). Within this data set, a partial temporal overlap (at the Late Eocene-Early Oligocene boundary; see, e.g., *Agard et al.* [2002] and *Rosenbaum and Lister* [2005] for a review) exists between ages attributed to (U)HP metamorphism [*Duchêne et al.*, 1997; *Gebauer et al.*, 1997; *Rubatto and Hermann*, 2001; *Rubatto and Scambelluri*, 2003; *Di Vincenzo et al.*, 2006] and the retrogressive metamorphism during exhumation [*Freeman et al.*, 1997; *Agard et al.*, 2002; *Cartwright and Barnicoat*, 2002; *Reddy et al.*, 2003; *Meffan-Main et al.*, 2004; *Federico et al.*, 2005] (Figure 1). Fission track thermochronology on apatite and zircon have revealed episodic

erosion/denudation stages (assisted by tectonics) since 32 Ma along the length of the Western Alps axis [e.g., *Seward and Mancktelow*, 1994; *Fügenschuh et al.*, 1997; *Fügenschuh and Schmid*, 2003; *Malusà et al.*, 2005; *Malusà and Vezzoli*, 2006].

[5] The published geochronological data set also results in a large variations of estimated exhumation velocities for (U) HP units, spanning from < mm yr^{-1} to cm yr^{-1} [e.g., *Ernst*, 1988; *Rubatto and Hermann*, 2001; *Chopin*, 2003; *Agard et al.*, 2009]. This variation implies slow to ultrafast exhumation rates in orogenic domain, which appears to be inconsistent with plausible geodynamic and tectonic scenarios (see discussion by *Agard et al.* [2002]).

[6] The Voltri Massif (Ligurian Alps, Italy) is a key area to investigate the geological parameters and tectonic scenarios controlling exhumation of the Alpine HP complexes, because of (1) its particular geographic position at the junction between the Western Alps and the Apennines belt (Figure 1), (2) no general consensus exists about the P-T-d-t path followed by the exhumed HP units (see below), and (3) proposed exhumation rates vary about 1 order of magnitude [e.g., *Rubatto and Scambelluri*, 2003; *Federico et al.*, 2005]. In this context, we present a multidisciplinary study that integrates U-Pb, ^{40}Ar-^{39}Ar, and apatite fission track (AFT) geochronology with petrographical and structural analyses. The results allow proposing a unitary P-T-d-t path for the HP units in the Voltri Massif by connecting deformation/metamorphic stages to specific time intervals. The results are discussed in terms of timing, rates, and mechanisms of orogenic deformation in the Voltri area and provide important insights into the processes that caused exhumation of the HP domains in the Western Alps.

2. Geological Background of the Voltri Massif

2.1. Main Structural Subdivisions

[7] The Voltri Massif of the Ligurian Alps (Figure 2a) consists of an eclogite-bearing metaophiolitic complex and corresponds to a remnant of the Liguro-Piedmont oceanic domain subducted during plate convergence between Europe and Adria [e.g., *Chiesa et al.*, 1975; *Vanossi et al.*, 1984]. The massif is located at the boundary between the Western Alps and the northern Apennines (Figure 1) and is in contact with the Hercynian continental basement rocks (amphibolites, orthogneiss and associated intrusive granites) of the Savona Massif [*Vanossi et al.*, 1984], and the ophiolitic terranes of the Sestri-Voltaggio Zone [e.g., *Cortesogno and Haccard*, 1984] and the Montenotte Unit [e.g., *Beccaluva et al.*, 1979]. In the Voltri Massif, the eclogitic rocks occur as variably retrogressed boudins (up to one kilometer in size) embedded in a mafic sequence composed by serpentinites, metagabbros, metabasalts and minor metarodingites (the Beigua Unit). The associated metasediments (the Voltri-Rossiglione Unit) mainly consist of mica schists, calc-schists and quartz schists, locally enclosing serpentinites, metabasalts and continent-derived rocks in boudins. Finally, partly serpentinized lherzolites (the Erro-Tobbio Unit) belonging to a mantle sliver of the former Adriatic continental domain [e.g., *Ernst*, 1981; *Scambelluri et al.*, 1991] are placed at the top of the metaophiolite series. Some authors propose the presence of a distinctive unit (the Palmaro-Caffarella Unit [e.g., *Cortesogno and Haccard*, 1984; *Capponi and Crispini*, 2006b]) in the southeastern part of the Voltri Massif, tectonically interlayered between the Beigua Unit and the Voltri-Rossiglione Unit. In this work, the Palmaro-Caffarella Unit is considered part of the Voltri-Rossiglione Unit (see discussions by *Capponi et al.* [2009] and *Vignaroli et al.* [2009b]). The entire tectonic edifice is overlain by Oligo-Miocene sedimentary deposits of the Tertiary Piedmont Basin (TPB) [e.g., *Charrier et al.*, 1964; *Franceschetti*, 1967; *Gelati and Gnaccolini*, 1998], a transgressive succession characterized by a basal monogenic breccia (the Costa Cravara Breccias) and a conglomeratic formation (the Molare Formation) containing eclogitic clasts commonly attributed to denudation of the Voltri Massif [e.g., *Vanossi et al.*, 1984; *Federico et al.*, 2004].

2.2. P-T Data Set

[8] Detailed petrological works for the Voltri eclogites show maximum peak metamorphic conditions of 18–22 kbar and 500°C–600°C [e.g., *Messiga et al.*, 1983; *Liou et al.*, 1998; *Brouwer et al.*, 2002; *Vignaroli et al.*, 2005], followed by polyphase retrograde evolution through the blueschist and the amphibolite facies fields [*Messiga and Scambelluri*, 1991; *Vignaroli et al.*, 2005]. An eclogitic overprint has been also documented in the Erro-Tobbio lherzolites (20–25 kbar and 550°C–600°C) and is considered indicative of an Alpine subduction history [e.g., *Scambelluri et al.*, 1995]. Few petrological studies dealt with the metamorphic evolution of the metasediments (Voltri-Rossiglione Unit and Palmaro-Caffarella Unit). Peak metamorphic conditions are represented by relicts of garnet, paragonite, sodic amphibole and zoisite together with Si^{4+}-rich phengite (Si^{4+} > 3.5 atoms per formula unit (a.p.f.u.)), all preserved

Figure 2. (a) Simplified geological map of the Voltri Massif and surrounding area from integration of older [*Allasinaz et al.*, 1971; *Chiesa et al.*, 1975] and more recent maps [*Capponi and Crispini*, 2005, 2006a, 2006b, 2006c]. Sample locations are also shown. (b) Compilation of published geochronological data for the Voltri Massif units and for clasts from the Tertiary Piedmont Basin. Numbers refer to the following: 1, *Rubatto and Scambelluri* [2003]; 2, *Hoogerduijn Strating* [1991]; 3, *Barbieri et al.* [2003]; 4, *Carrapa et al.* [2004]; 5, *Charrier et al.* [1964] and *Gelati et al.* [1993]; 6, *Di Biase and Pandolfi* [1999]; 7, *Federico et al.* [2005]; 8, *Gelati and Gnaccolini* [1998]; 9, *Bertotti et al.* [2006]; 10, *Federico et al.* [2007b]. (c–f) Proposed tectonic models for exhumation in the Voltri Massif, simplified and redrawn after *Messiga and Scambelluri* [1991] (Figure 2c), *Federico et al.* [2007a] (Figure 2d), *Hoogerduijn Strating* [1994], with permission from Elsevier (Figure 2e), and *Vignaroli et al.* [2008] (Figure 2f). The asterisk indicates the supposed position of the Voltri Massif.

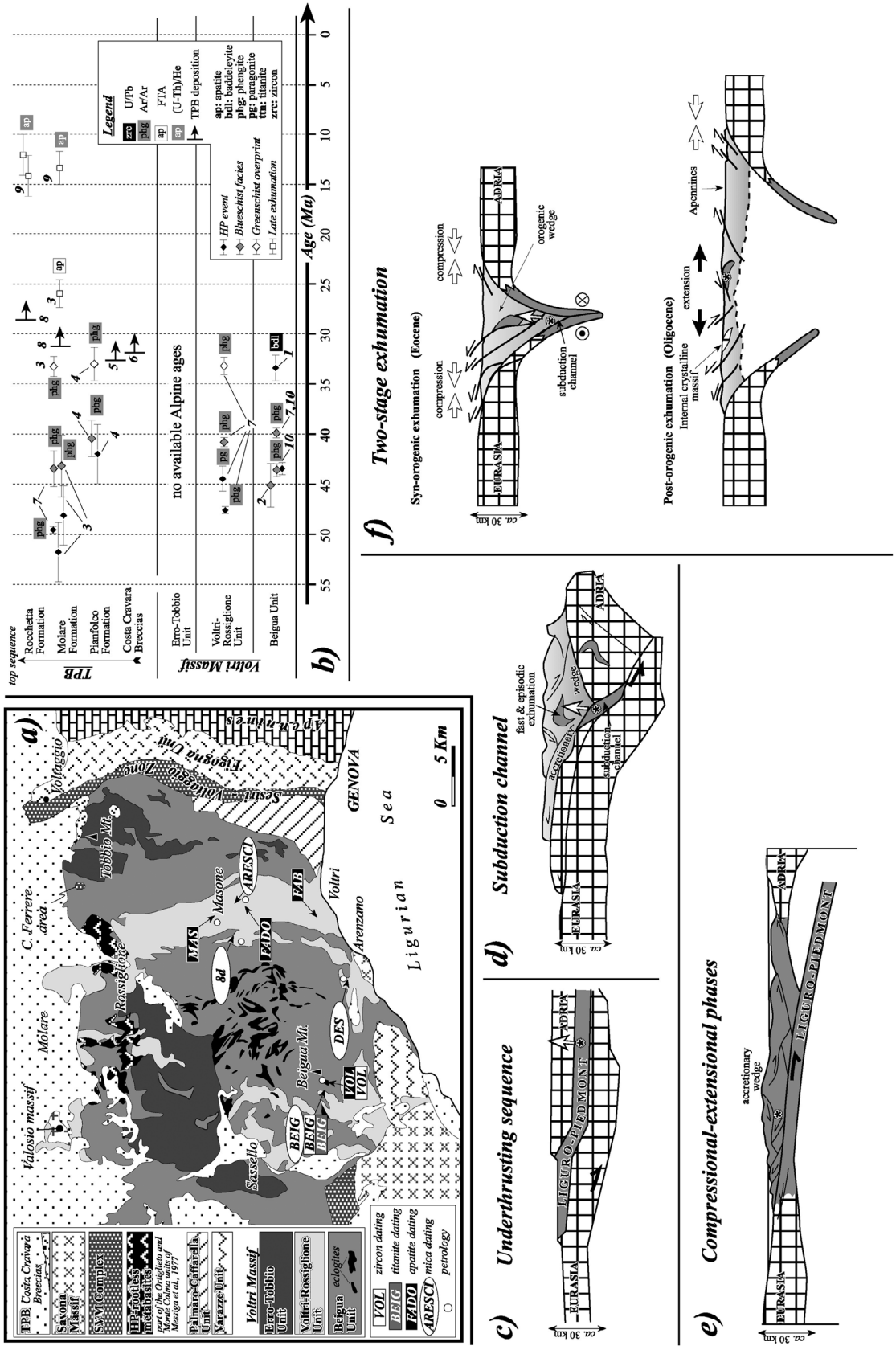
a)
Voltaggio
Molare
C. Ferrere area
Tobbio Mt.
Rossiglione
Masone
Voltri
Arenzano
GENOVA
Sea
Ligurian
0 5 Km
Sassello
Beigua Mt.
Palmaro-Caffarella Unit
Yarazzeri Unit
Voltri Massif
Erro-Tobbio Unit
Voltri-Rossiglione Unit
Beigua Unit
eclogites
zircon dating
titanite dating
apatite dating
mica dating
petrology
b)
top sequence
Rocchetta Formation
Molare Formation
Pianfolco Formation
Costa Cravara Breccias
TPB
Erro-Tobbio Unit
Voltri-Rossiglione Unit
Beigua Unit
Voltri Massif
no available Alpine ages
Age (Ma)
Legend
U/Pb
Ar/Ar
FTA
(U-Th)/He
TPB deposition
HP event
Blueschist facies
Greenschist overprint
Late exhumation
ap: apatite
bdl: baddeleyite
phg: phengite
pg: paragonite
ttn: titanite
zrc: zircon
c)
Underthrusting sequence
EURASIA
LIGURO-PIEDMONT
ADRIA
ca. 30 km
d)
Subduction channel
fast & episodic exhumation
accretionary wedge
subduction channel
e)
Compressional-extensional phases
accretionary wedge
f)
Two-stage exhumation
Syn-orogenic exhumation (Eocene)
compression
orogenic wedge
subduction channel
Post-orogenic exhumation (Oligocene)
Internal crystalline massif
extension
Apennines

Figure 2

in low-strain domains indicating temperatures of 450°C–550°C and pressures of 12–18 kbar [e.g., *Cimmino and Messiga*, 1979; *Hoogerduijn Strating*, 1991; *Federico et al.*, 2007a]. The polyphase decompression event involves a transition from blueschist facies conditions to greenschist facies conditions, as revealed by the occurrence of chloritoid, albite, chlorite, titanite and lower Si^{4+} phengite assemblages [*Cimmino and Messiga*, 1979; *Hoogerduijn Strating*, 1991].

2.3. Deformation Patterns

[9] The earliest deformation fabric recognized in the eclogites of the Beigua Unit is a penetrative synblueschist foliation developed during top-to-the-north/NNW shearing [*Vignaroli et al.*, 2005]. In the surrounding serpentinites, a polyphase fabric has been described and interpreted as recording the progressive evolution from ductile HP deformation to late, multistage, brittle structures [e.g., *Hoogerduijn Strating*, 1994; *Capponi and Crispini*, 2002]. In the Erro-Tobbio Unit, both presubduction [e.g., *Vissers et al.*, 1991; *Borghini et al.*, 2007] and subduction related structures have been observed [e.g., *Hoogerduijn Strating et al.*, 1993; *Scambelluri et al.*, 1995; *Hermann et al.*, 2000]. The deformation history is best preserved in the metasedimentary sequence of the Voltri-Rossiglione Unit, where the polyphase fabric shows evidence of progressively refolded mylonitic zones with superimposed brittle deformation features [e.g., *Hoogerduijn Strating*, 1994; *Capponi and Crispini*, 2002; *Federico et al.*, 2007a; *Vignaroli et al.*, 2009a], attesting for evolution of deformation during exhumation path.

2.4. Available Geochronological Data

[10] The available age constraints for deformation events affecting the units exposed in the Voltri Massif are mainly based on both stratigraphic constraints from the TPB sedimentary sequence and radiometric dating (Figure 2b).

[11] Stratigraphic correlations [*Charrier et al.*, 1964; *Franceschetti*, 1967; *Gelati et al.*, 1993; *Di Biase and Pandolfi*, 1999] propose an Early Oligocene age for the deposition of the lowermost formations of the TPB (the Costa Cravara Breccias and the Pianfolco Formation). ^{40}Ar-^{39}Ar dating, undertaken on detrital phengite grains separated from the basal formations of the TPB sequence [*Barbieri et al.*, 2003; *Carrapa et al.*, 2004; *Federico et al.*, 2005], provides two age clusters: a 45–48 Ma interval correlated with the time of peak metamorphism, and a 32–34 Ma cluster correlated with the first depositional stage of the TPB. Apatite (U-Th)/He and fission track thermochronology data, on Oligo-Miocene deposits and the Voltri units, indicate that the basin was exhumed above 4 km by ~26 Ma [*Bertotti et al.*, 2006].

[12] Concerning timing of tectonometamorphic events in the Voltri units, contrasting results have been provided by the application of thermochronometers with different closure temperatures. The first radiometric data were obtained by *Schamel* [1974], who measured whole rock K-Ar ages of circa 41 and 36 Ma from metasediments of the Voltri-Rossiglione Unit. Subsequent ^{40}Ar-^{39}Ar dating on phengite from Beigua metabasites yielded an age of 45.2 ± 1.8 Ma [*Hoogerduijn Strating*, 1991], considered to represent the timing of exhumation of the HP rocks. *Rubatto and Scambelluri* [2003] obtained a SHRIMP U-Pb age of 33.6 ± 1.0 Ma from baddeleyite crystals, in textural equilibrium with Ti-clinohumite porphyroblasts, in eclogites of the Beigua Unit. This result was interpreted as the time of HP metamorphism or as maximum estimate for blueschist reequilibration. More recently, *Federico et al.* [2005, 2007b] carried out ^{40}Ar-^{39}Ar analyses on phengite grains from both the Voltri units and eclogitic clasts of the TPB, and results support the hypothesis that eclogitic metamorphism occurred at ~49–43 Ma, blueschist metamorphism took place at ~43–40 Ma, and final greenschist retrogression occurred at ~33 Ma. The discrepancies between the above results have thus created debate on (1) the timing of the HP metamorphism and (2) the exhumation rates accompanying unroofing of the HP units.

2.5. Previous Tectonic Models

[13] The difficult task of reconciling and interpreting the available geological information has resulted in the formulation of contrasting tectonic models for the exhumation history of the Voltri Massif. Many published studies attribute the tectonic architecture of the Voltri units to a polyphase contractional regime, which caused both the early top-to-the-west/NW nappe emplacement [e.g., *Hoogerduijn Strating*, 1994; *Vissers et al.*, 2001; *Capponi and Crispini*, 2002] and the late-orogenic entrainment of lherzolite [e.g., *Chiesa et al.*, 1975; *Capponi et al.*, 1986, 1999] and limestone fragments [*Capponi et al.*, 1998] on top of the metaophiolites. Thrusting is also thought to explain the local deformation of the TPB sediments [e.g., *Capponi and Giammarino*, 1982; *Mutti et al.*, 1995; *Carrapa et al.*, 2004; *Piana et al.*, 2006]. These compressive structures have been related to a sequence of underthrusting events during the progression of subduction from the African to the European margin [*Messiga and Scambelluri*, 1991] (Figure 2c). The complete subduction-exhumation cycle of the HP units has been considered in the context of a subduction channel of serpentinites [*Scambelluri et al.*, 1995; *Hermann et al.*, 2000; *Federico et al.*, 2004, 2007b] (Figure 2d), providing for a return flow of buried material. This tectonic setting is also considered responsible for the subsequent rapid, but episodic, exhumation of deeply accreted buoyant material [*Rubatto and Scambelluri*, 2003]. As an alternative, *Hoogerduijn Strating* [1994] proposed the occurrence of extensional detachments causing tectonic elision and local metamorphic pressure gaps within the nappe pile. This scenario is linked to a succession of compressional and extensional tectonic phases in response to the dynamic evolution of the Ligurian accretionary wedge during Africa-Europe convergence (Figure 2e). Recently, *Vignaroli et al.* [2009a] emphasized the role of top-to-the-west/NW extensional detachment systems, which developed during retrogressive greenschist metamorphism and evolved toward brittle conditions. In this scenario, exhumation of the Voltri HP units is attributed to a two-stage tectonic process involving a transition from transpressive to extensional

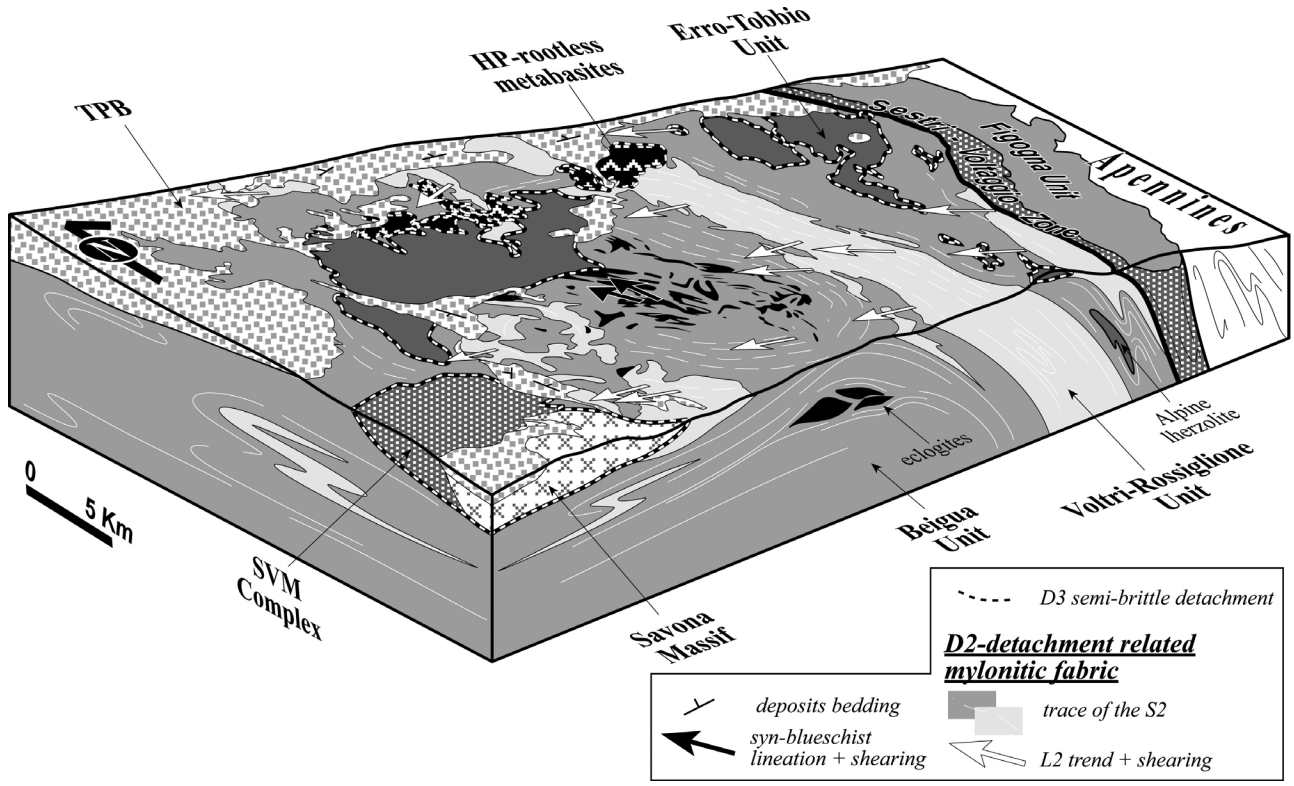

Figure 3. Simplified geological block diagram for the Voltri Massif and surrounding regions showing the main structural features from this study and *Vignaroli et al.* [2009a]. The metamorphic units are interpreted as arranged in a domal architecture defined by the syngreenschist, mylonitic foliation (D_2 fabric). The eclogitic domain (also projected on the X-Z section) represents the core of the overall structure. The *SL*, D_2-related fabric is shown together with the associated sense of shear (white arrows, indicating movement of the hanging wall block). The map does not include the Varazze Unit, while the Palmaro-Caffarella Unit is considered here as part of the Voltri-Rossiglione Unit. The geological block diagram does not contemplate the effects of the brittle deformation structures (fault systems offsets).

tectonic regimes at the Alps-Apennines junction [*Vignaroli et al.*, 2008] (Figure 2f).

3. Methods

[14] Our study is based on a revision of the existing structural and petrological data set available for the Voltri Massif area. The main geometric-structural relationships between the main tectonic units in the Voltri Massif follow those reported by *Vignaroli et al.* [2008, 2009a], with tectonic boundaries based on a reinterpretation of previous geological maps [e.g., *Allasinaz et al.*, 1971; *Cortesogno and Haccard*, 1984; *Capponi et al.*, 1994; *Capponi and Crispini*, 2005, 2006a, 2006b, 2006c]. Sampling for both petrological and geochronological studies was conducted across the entire Voltri Massif, with samples collected from both the eclogitic core (Beigua unit) and the enveloping metasediments of the Voltri-Rossiglione Unit (see Figure 2a for sample location). Petrological studies focused on the metasedimentary Voltri-Rossiglione Unit, which was used as a template to assess the exhumation P-T history of the HP domains. Geochronological studies integrate SHRIMP U-Pb measurements of zircon and titanite separates with ^{40}Ar-^{39}Ar dating of phengite separates on selected samples from the Beigua eclogites and the Voltri-Rossiglione Unit. Sample selection was based on detailed textural studies documenting the relationships between mineral blastesis and polyphase deformation fabrics. In addition, preliminary low-temperature thermochronological data (AFT dating) was also assessed, to constrain the near-surface T-t paths [see, e.g., *Fitzgerald et al.*, 2006] of the Voltri-Rossiglione Unit. The different analytical techniques were optimized on the basis of the mesoscale and microscale properties of the selected samples (see section 5), in order to provide a complete reconstruction of the P-T-d-t history recorded by the exhumed HP core of the Voltri Massif.

4. Structural Setting

[15] The ophiolite-bearing units of the Voltri Massif define a ~30 km wide, E-W elongated metamorphic complex with an eclogitic core (Figure 3). The domal architecture is expressed by the attitude of the main retrogressive foliation (S_2) within the Beigua and Voltri-Rossiglione units (the Lower Tectonic Complex of *Vignaroli et al.* [2009a]), which is steeply dipping in the

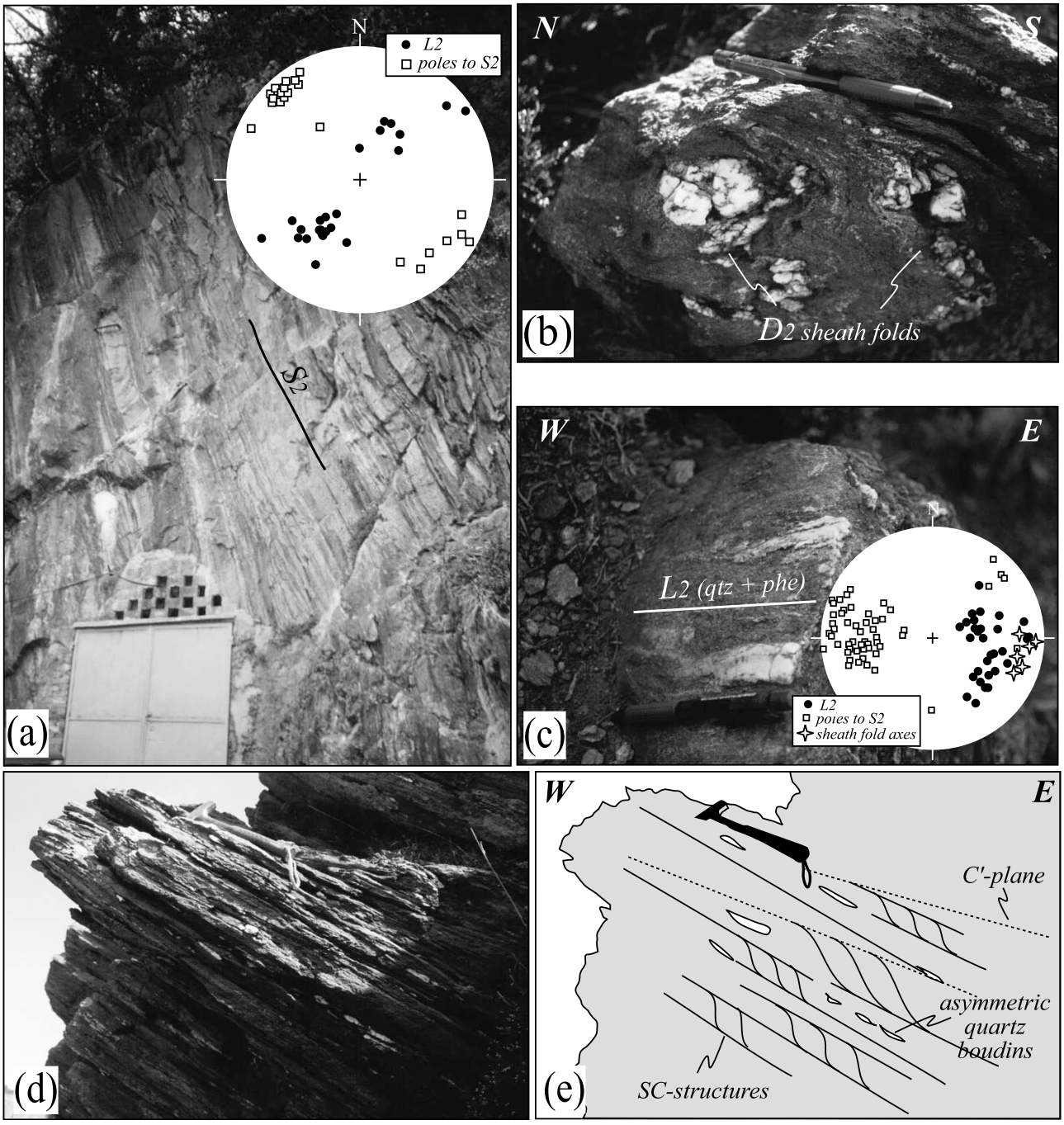

Figure 4. Mesoscale ductile D_2-related fabric. (a) Subvertical mylonitic foliation in the eastern side of the eclogitic core. (b) D_2 transpositive fabric producing sheath folds oriented parallel to the main L_2 stretching lineation (see stereoplot in Figure 4c). (c) D_2 planolinear fabric showing L_2 stretching lineation provided by the qtz + phg_2 assemblage. (d) Mesoscale tectonite in the Voltri-Rossiglione quartz schists characterized by noncoaxial, top-to-the-west shearing. (e) Line drawing of Figure 4d. All stereoplots are lower-hemisphere projections of the Schmidt net.

east (Figure 4a) and gently westward dipping in the west [see also *Capponi et al.*, 1994; *Capponi and Crispini*, 2002]. The Lower Tectonic Complex is juxtaposed against several rootless bodies of lherzolite [*Chiesa et al.*, 1975; *Capponi et al.*, 1986, 1999; *Vissers et al.*, 2001], limestones [*Cortesogno and Haccard*, 1984; *Capponi et al.*, 1998] and variably retrogressed HP metabasites [e.g., *Messiga et al.*, 1977] (constituting part of the Upper Tectonic Complex of *Vignaroli et al.* [2009a]), where the D_2 fabric is not pervasive (Figure 3).

[16] The Voltri-Rossiglione Unit shows three main syn-metamorphic deformation episodes (D_1-M_1, D_2-M_2 and D_3-M_3). The early D_1 fabric is observed only in microlithons preserved in D_2 low-strain domains (see section 5.1). The M_1 mineralogical assemblage consists of cld_1 + phg_1 + qtz ± chl_1 composite associations (mineral abbreviations are from *Kretz* [1983] and *Bucher and Frey* [2002], unless otherwise specified), together with accessory phases such as tourmaline and rutile. At the mesoscale, the D_2 fabric is associated with high-strain deformation structures, such as sheath folds [*Crispini and Capponi*, 1997] (Figure 4b) and reoriented folds [e.g., *Capponi*, 1991; *Vignaroli et al.*, 2009a] with axes parallel to the main (L_2) stretching lineation. The L_2 generally trends from WSW-ENE to WNW-ESE (Figures 4a and 4c). Mesoscale kinematic indicators (such as *SC* structures, C' shear planes, asymmetric quartz boudins [e.g., *Passchier and Trouw*, 2005]) indicate a general top-to-the-west sense of shear [*Vignaroli et al.*, 2009a] (Figures 3, 4c, and 4d). The M_2 metamorphic reequilibration is widespread and manifests as overgrowths of phg_2 onto pristine phg_1 and assemblages of phg_2 + chl_2 + ab + pg + qtz + cal, together with titanite porphyroblasts oriented along the S_2 foliation (Figure 4b). Albite and titanite also host inclusions of phg_1. Finally, the S_2 foliation is overprinted by the M_3 assemblage, consisting of texturally discordant crystallization of phg_3 + chl_3 on the S_2. The S_3 foliation is also associated with a F_3 folding event overprinting the D_2 ductile fabric. The F_3 hinge lines trend roughly parallel to the L_2 stretching lineation.

[17] Progressive ductile-to-brittle shear strain localization (D_3) is observed in the outer portions of the metamorphic dome, culminating in the development of subhorizontal cataclastic bands, which systematically overprint the D_2 mylonitic fabric. This cataclastic deformation corresponds both to major semibrittle contacts that control the tectonic juxtaposition of the Upper Tectonic Complex and to local normal-sense metamorphic gaps within the tectonic edifice [*Vignaroli et al.*, 2009a]. This tectonic scenario is complicated by the occurrence of the eclogite-bearing lherzolites of the Erro-Tobbio Unit on top of the Lower Tectonic Complex. Nevertheless, some have proposed that the Erro-Tobbio Unit was located at shallower structural depths during exhumation of the Lower Tectonic Complex, thus maintaining a structural/metamorphic break with the syn-greenschist D_2-M_2 fabric in the Lower Tectonic Complex (see discussions by *Capponi et al.* [2009] and *Vignaroli et al.* [2009b]). Extensional faults and tension gashes cut the mylonitic bands, indicating that shearing continued during progressive exhumation of the ophiolite dome. The brittle extensional structures strike subperpendicular to the L_2 stretching lineation in the underlying, ductile deformed units and show penetrative E-W trending striations, aligned with the ductile shear transport direction.

5. Structures, Petrography, and Mineral Composition of Selected Samples

[18] The metamorphic/deformation characteristics of samples used for the petrological, geochronological, and AFT studies are summarized in Tables 1a and 1b. Samples from the metasedimentary Voltri-Rossiglione Unit (samples 8D, ARESCI, BEIG, DES, and MAS) include calc-schists, mica schists, and quartz schists dispersed around the eclogitic core (Figure 2a). From a structural point of view, these samples correspond to second-phase *S-L* tectonites, locally evolving to *L* tectonites. A polyphase deformation fabric is recognized in all samples (from D_1-M_1 to D_2-M_2, to D_3-M_3), partitioned between domains of coaxial deformation produced during vertical shortening and E-W stretching, and domains of noncoaxial deformation associated with the development of meter-scale mylonitic shear zones. On the basis of dominant mesoscale and microscale fabrics we selected (1) samples showing the best preserved M_1 mineralogical assemblages (samples 8D, ARESCI, DES), (2) samples with prominent D_2 transpositive fabrics (samples BEIG, MAS), and (3) samples showing evidence of progressive ductile-to-brittle evolution of deformation characteristics (samples FAB, FADO). Eclogitic sample VOL was selected to ascertain the metamorphic ages of the inner core of the Voltri Massif. This sample also contains apatite suitable for AFT analysis. In the following sections, we detail the petrographic context of the studied samples. Representative mineral compositions are shown in Table 2 (see section A1 for analytical details).

5.1. Voltri-Rossiglione Metasediments

[19] *Sample ARESCI* is part of a calc-schist unit that crops out in the middle section of the N-S striking metasedimentary sequence, east of the eclogitic core (Figures 2 and 3). The microfabric of this sample is characterized by domains with preserved S_1 foliations locally overprinted by incipient S_2 crenulations (Figure 5a), and domains where the S_2 is well developed and forms mylonitized zones (Figure 5b). The D_1 fabric consists of cld_1, phg_1 and chl_1 (+qtz). Cld_1 (X_{Mg} = Mg/(Mg+Fe^{2+}+ Mn) = 0.13; Table 2) shows different textural relationships with respect to the surrounding foliation, as it grows along the D_1 foliation (Figure 5b) and also shows a fan-like structure surrounded by the S_2 foliation (Figure 5c). The latter is considered to result from progressive crystallization of cld from the D_1 fabric to D_2 schistosity. Backscattered electron (BSE) (Figure 5d) images provide evidence that cld_1 grows in microlithons wrapped by the D_2 fabric where, in turn, cld_2 is in textural equilibrium with the S_2 foliation. The S_2 fabric is defined by assemblages of phg_2, chl_2, ab, qtz in association with pg and cal. Phengite shows decreasing Si^{4+} contents (a.p.f.u.) from phg_1 (Si^{4+} = 3.4) to phg_2 (Si^{4+} = 3.2) to phg_3 (Si^{4+} = 3.0) (Table 2).

[20] *Sample DES* derives from a mylonitic horizon containing mica schists and quartz schists, embedded within a serpentinite matrix. At the scale of the outcrop, the rocks correspond to *SL* tectonites, locally evolved to *L* tectonites. This sample is characterized by a dominant D_2 fabric consisting of a pervasive S_2 foliation and a NW-SE trending stretching lineation defined by phg + qtz + cld. The transpositive character of the D_2 fabric can be recognized at the microscale, where the M_1 fabric is only represented by relicts of hinge folds inside the S_2 foliation. In the hinge folds, phg_1 (+qtz) and chl_1 are present. Porphyroclasts of cld_1 have been also recognized dispersed in the matrix. The relative timing of cld crystallization was ascertained from

Table 1a. Metamorphism/Deformation Relationships of the Analyzed Metasedimentary Samples[a]

Sample	Metamorphic Fabric			Accessories	Type of Analyses
		Retrogressive Stages			
	HP Climax M1	M2	M3		
8D	cld1, phg1, chl1(?), qtz	cld2, phg2, chl2, pg, cal, ab, ttn, qtz	phg3, chl3, cal, qtz	ttn, zrn	P
ARESCI	cld1, phg1, chl1(?), qtz	cld2, phg2, chl2, pg, cal, ab, qtz	phg3, qtz		P, Ar/Ar
BEIG	phg1, ttn(?), rt, qtz	phg2, chl2, pg, cal, ab, ttn, ep, qtz	phg3, chl3, cal, ab(?), ep, qtz	zrn	P, Ar/Ar, SHRIMP, La-ICPM
DES	cld1, phg1, chl1(?), tur, qtz	cld2, phg2, chl2, ab, tur, qtz	phg3, ab, qtz		P, Ar/Ar
FAB	phg1, rt, tur, qtz	phg2, chl2, cal, ab, ttn, tur, qtz	phg3, chl3, cal, qtz	ap, ttn, zrn	AFT
FADO	phg1, rt, tur, qtz	phg2, chl2, cal, ab, pg, ttn, tur, qtz	phg3, chl3, cal, qtz	ap, ttn, zrn	AFT
MAS	phg1, rt, tur, qtz	phg2, chl2, cal, ab, ttn, tur, qtz	phg3, chl3, cal, ab, qtz	ap, ttn, zrn	P, AFT
	D1	D2	D3		
Deformational features	relict, transposed; no kinematic data	*SL* and *L* tectonites; top-to-the-west shearing	static overgrowth; semibrittle to brittle top-to-the-west shearing		

[a]Mineral abbreviations are from *Kretz* [1983] and *Bucher and Frey* [2002]. P, petrological analyses.

textural relationships, enabling discrimination of porphyroclasts with irregular rims and internal brittle fractures (cld_1) from euhedral, elongated crystals along the D_2 foliation (cld_2). Where large cld grains are oriented along the foliation and show chl_2 pressure shadows at the edge, these are interpreted as pretectonic to syntectonic crystals with respect to the D_2 fabric (Figure 5e). Zoning of large chloritoid crystal is expressed by higher X_{Mg} contents in the cores (0.14–0.17) compared to the rims (0.11–0.13) (Figure 5f and Table 2). The S_2 schistosity is formed by phg_2, chl_2, ab, qtz and pg. Phengite shows decreasing Si^{4+} content (a.p.f.u.) from phg_1 (Si^{4+} = 3.3) to phg_2 (Si^{4+} = 3.1–3.0) (Table 2). Tourmaline is a common accessory mineral, and appears to be pretectonic to syntectonic with respect to S_2.

[21] *Sample 8D* originates from the *SL* tectonite shown in Figure 4d. The tectonite is part of a ~30 m thick mylonitic shear zone located in the eastern part of the eclogitic core. The main fabric consists of the S_2 foliation, with a roughly N-S strike and easterly dip ($30° < \phi < 75°$), and an E-W stretching lineation. The shear zone tectonically overlies the westernmost serpentinite that encloses the eclogites (Figures 2 and 3). The M_1 mineralogical assemblage was defined from microscale investigations on low-strain domains and constitutes cld_1, phg_1 (+qtz) and minor chl_1 that presumably grew during the D_2-M_2 stage. The transpositive S_2 schistosity is defined by the blastesis of phg_2, chl_2, ab and qtz, in association with pg, cal and cld_2. Kinematic indicators (such as oblique foliations, mica fish structures, *SC* structures, *C'* shear planes) in sections normal to S_2 and parallel to L_2 indicate a top-to-the-west sense of shear (Figures 5g and 5h). There are no appreciable compositional variations between rim and core regions of large cld crystals, nor between cld_1 (as relict in the D_2 fabric) and cld_2 (disposed along the S_2) grains (X_{Mg} = 0.10–0.11; Table 2). On the other hand, the Si^{4+} contents of phg decrease progressively from phg_1 (Si^{4+} = 3.4) to phg_2 (Si^{4+} = 3.2) to phg_3 (Si^{4+} = 3.1) (Table 2). The largest phg crystals (phg_3) are oriented across the main S_2 foliation, indicating static overgrowth.

[22] *Sample BEIG* derives from the western flank of Mount Beigua (Figures 2 and 3), where a 20 m thick mica schist tectonically overlies serpentinites along a gently westward dipping D_2 mylonitic shear zone. The main D_2-M_2 fabric is pervasive at the outcrop scale. The M_1 mineralogical association is recognized mainly from inclusions of phg_1 (Si^{4+} = 3.4) and subordinate rutile in titanite and feldspar porphyroclasts (Figure 5i). The M_2 metamorphic assemblage is dominated by phg_2 (Si^{4+} = 3.4–3.3), commonly associated with pg + chl_2 (X_{Mg} = 0.62) + qtz + ab + ttn ± cc ± oxides. Phg_2 shows recrystallization features and is zoned from core (Si^{4+} = 3.4) to rim (Si^{4+} = 3.2). Titanite porphyroblasts appear to be syntectonic with respect to the main D_2 fabric. This is evidenced by (1) the morphological shape of the elongated porphyroblasts oriented along the S_2 foliation and the development of phg_2 + chl_2 pressure shadows around titanite porphyroblasts (Figure 5i), (2) the occurrence of high-Si phg_1 as inclusions in titanite (Figure 5i), (3) continuity between the external and internal foliations in the matrix surrounding the porphyroblasts (Figure 5j), and (4) σ-type porphyroblasts, which indicate a top-to-the-west

Table 1b. Metamorphism Relationships of the Analyzed Eclogitic Sample[a]

Sample	Pre-HP	HP Climax E	Retrogressive Stages			Accessories	Type of Analyses
	Climax Pre-E		BS	AM	GS		
VOL	rt, ttn, ep, ap, pg, ab, hbl, brs, grt, qtz	grt, omp, rt	gln, ep, ab, pg, chl	brs, chl, ep, ab	act, win, chl, ab	ap, zrn	P [*Vignaroli et al.*, 2005], SHRIMP, AFT

[a]Mineral abbreviations are from *Kretz* [1983] and *Bucher and Frey* [2002] except for brs, barroisite; win, winchite. AM, amphibolite; BS, blueschist; E, eclogite; GS, greenschist; P, petrological analyses.

Table 2. Representative Microprobe Analyses of Minerals From the Voltri Massif[a]

	Chloritoid						Phengite										
Analysis	7	1	3	13	51	14	7	4	45	44	60	39	23	17	47	19	68
Microtextural site	a	b	a	b	a	b	c	c	c	c	c	d	b	b	b	b	b
Metamorphic stage	M1	M2	M1	M1-M2	M1	M2	M1 (?)	M1	M1	M1	M1	M1	M2	M2	M2	M2	M2
Sample	8D	8D	Aresci	Aresci	Des	Des	8D	Aresci	Beig	Des	Mas	Beig	8D	Aresci	Beig	Des	Mas
SiO_2	23.40	23.23	23.43	23.65	24.10	23.94	49.58	51.21	51.66	49.68	52.55	51.63	46.87	48.84	49.83	46.79	49.64
TiO_2	0.00	0.02	0.04	0.06	0.00	0.01	0.08	0.10	0.15	0.21	0.16	0.13	0.20	0.18	0.18	0.18	0.18
Al_2O_3	40.59	40.59	41.52	41.17	40.82	40.00	27.08	26.81	27.22	29.37	23.75	27.95	32.57	32.07	29.31	35.21	28.00
Cr_2O_3	0.00	0.00	0.00	0.00	0.02	0.01	0.00	0.00	0.02	0.02	0.01	0.00	0.00	0.00	0.00	0.01	0.01
MgO	1.85	1.72	2.04	2.27	2.67	1.71	3.16	3.63	3.64	2.36	3.25	3.42	1.53	1.68	2.93	0.85	2.19
CaO	0.02	0.03	0.00	0.00	0.00	0.00	0.12	0.05	0.02	0.14	0.00	0.02	0.03	0.00	0.00	0.11	0.06
MnO	0.16	0.32	2.38	1.58	0.36	0.50	0.00	0.01	0.01	0.01	0.05	0.06	0.00	0.08	0.02	0.00	0.00
FeO	25.88	25.69	23.71	23.93	24.14	25.63	3.02	2.57	2.28	2.58	4.30	1.98	2.39	2.37	1.97	1.14	3.17
Na_2O	0.00	0.01	0.01	0.00	0.00	0.00	0.17	0.20	0.30	0.33	0.03	0.36	0.49	0.46	0.36	1.10	0.27
K_2O	0.07	0.01	0.01	0.01	0.02	0.01	9.94	9.31	9.81	9.68	10.40	9.74	9.68	9.68	9.79	8.77	9.48
Total	91.98	91.66	93.14	92.71	92.13	91.81	93.15	93.89	95.31	94.37	94.82	95.43	93.76	95.36	94.56	94.15	93.25
F. Struct.	12 ox	12 ox	12 ox	12 ox	12 ox	12 ox	11 ox	11 ox	11 ox	11 ox	11 ox	11 ox	11 ox	11 ox	11 ox	11 ox	11 ox
Si	1.96	1.95	1.94	1.96	2.00	2.01	3.39	3.44	3.42	3.33	3.54	3.41	3.17	3.24	3.32	3.12	3.37
Ti	0.00	0.00	0.00	0.00	0.00	0.00	0.00	0.01	0.01	0.01	0.01	0.01	0.01	0.01	0.01	0.01	0.01
Al	4.01	4.02	4.04	4.02	3.98	3.96	2.18	2.12	2.12	2.32	1.88	2.17	2.60	2.51	2.30	2.76	2.24
Cr	0.00	0.00	0.00	0.00	0.00	0.00	0.00	0.00	0.00	0.00	0.00	0.00	0.00	0.00	0.00	0.00	0.00
Mg	0.23	0.22	0.25	0.28	0.33	0.21	0.32	0.36	0.36	0.24	0.33	0.34	0.15	0.17	0.29	0.08	0.22
Ca	0.00	0.00	0.00	0.00	0.00	0.00	0.01	0.00	0.00	0.01	0.00	0.00	0.00	0.00	0.00	0.01	0.00
Mn	0.01	0.02	0.17	0.11	0.03	0.04	0.00	0.00	0.00	0.00	0.00	0.00	0.00	0.00	0.00	0.00	0.00
Fe^{3+}	0.00	0.00	0.00	0.00	0.02	0.04	0.00	0.00	0.00	0.00	0.12	0.00	0.00	0.00	0.00	0.00	0.00
Fe^{2+}	1.81	1.81	1.64	1.66	1.67	1.80	0.17	0.14	0.13	0.14	0.24	0.11	0.14	0.13	0.11	0.06	0.18
Na	0.00	0.00	0.00	0.00	0.00	0.00	0.02	0.03	0.04	0.04	0.00	0.05	0.06	0.06	0.05	0.14	0.04
K	0.01	0.00	0.00	0.00	0.00	0.00	0.87	0.80	0.83	0.83	0.89	0.82	0.84	0.82	0.83	0.75	0.82
XMg	0.11	0.11	0.13	0.14	0.16	0.11	0.65	0.72	0.74	0.62	0.57	0.75	0.53	0.56	0.72	0.57	0.55

	Phengite			Chlorite							Paragonite		Albite	
Analysis	19	18	50	13	7	16	19	49	23	63	9	11	37	10
Microtextural site	e	e	e	c	c	b	b	b	b	b	b	b	b	b
Metamorphic stage	M3	M3	M3	M1 ?	M1 ?	M2	M2	M2	M2	M2	M2	M2	M2	retrogr. b-schist
Sample	8D	Aresci	Beig	8D	Aresci	8D	Aresci	Beig	Des	Mas	8D	Aresci	Beig	Vol
SiO_2	45.65	45.72	46.72	23.48	24.19	22.92	23.33	26.21	24.07	24.65	45.87	46.28	69.50	68.64
TiO_2	0.20	0.09	0.27	0.06	0.04	0.13	0.06	0.06	0.04	0.04	0.04	0.03	0.00	0.04
Al_2O_3	36.65	37.26	29.44	22.54	21.91	22.72	22.58	22.65	23.19	22.21	39.17	40.49	19.73	20.17
Cr_2O_3	0.00	0.00	0.00					0.03	0.02	0.00	0.00	0.00	0.00	0.04
MgO	0.39	0.57	2.37	11.22	11.61	10.47	11.05	18.49	12.92	13.66	0.18	0.14	0.00	0.01
CaO	0.06	0.00	0.09	0.01	0.04	0.03	0.05	0.02	0.09	0.05	0.07	0.08	0.36	0.56
MnO	0.00	0.03	0.07	0.15	1.10	0.13	1.28	0.10	0.08	0.12	0.00	0.02	0.06	0.11
FeO	1.17	1.13	5.36	30.05	29.51	31.52	28.59	20.74	27.71	26.71	1.50	0.36	0.03	0.12
Na_2O	1.17	1.17	0.41	0.03	0.03	0.02	0.02	0.02	0.02	0.00	7.31	7.22	11.69	10.90
K_2O	9.02	8.95	9.26	0.06	0.08	0.03	0.07	0.02	0.00	0.00	0.69	0.55	0.08	0.02
Total	94.30	94.92	94.03	87.64	88.51	88.00	87.03	88.34	88.15	87.54	94.83	95.17	101.58	100.61
F. Struct.	11 ox	11 ox	11 ox	14 ox	14 ox	14 ox	14 ox	14 ox	14 ox	14 ox	11 ox	11 ox	8 ox	8 ox
Si	3.05	3.03	3.20	2.55	2.60	2.50	2.55	2.67	2.56	2.62	2.91	2.90	2.99	2.98
Ti	0.01	0.00	0.01	0.01	0.00	0.01	0.01	0.00	0.00	0.00	0.00	0.00	0.00	0.00
Al	2.88	2.91	2.38	2.88	2.78	2.92	2.91	2.72	2.90	2.78	2.93	2.99	1.00	1.02

Table 2. (continued)

	Phengite			Chlorite							Paragonite		Albite	
Analysis	19	18	50	13	7	16	19	49	23	63	9	11	37	10
Cr	0.00	0.00	0.00	0.00	0.00	0.00	0.00	0.00	0.00	0.00	0.00	0.00	0.00	0.00
Mg	0.04	0.06	0.24	1.82	1.86	1.70	1.80	2.80	2.05	2.16	0.02	0.01	0.00	0.00
Ca	0.00	0.00	0.01	0.00	0.00	0.00	0.01	0.00	0.01	0.01	0.00	0.01	0.02	0.03
Mn	0.00	0.00	0.00	0.01	0.10	0.01	0.12	0.01	0.01	0.01	0.00	0.00	0.00	0.00
Fe^{3+}	0.00	0.00	0.00	0.00	0.00	0.00	0.00	0.00	0.00	0.00	0.00	0.00	0.00	0.00
Fe^{2+}	0.07	0.06	0.31	2.73	2.65	2.87	2.61	1.76	2.46	2.37	0.08	0.02		
Na	0.15	0.15	0.05	0.01	0.01	0.00	0.00	0.00	0.00	0.00	0.90	0.88	0.98	0.92
K	0.77	0.76	0.81	0.01	0.01	0.00	0.01	0.00	0.00	0.00	0.06	0.04	0.00	0.00
XMg	0.37	0.47	0.44	0.40	0.41	0.37	0.41	0.61	0.45	0.48	0.18	0.42		
XAb													0.98	0.97
XAn													0.02	0.03

	Titanite			Epidote		Garnet			Clinopyroxene		Amphibole			
Analysis	2c	41	42	1a	9	1	2	3	22	7	8in	8	9	5
Microtextural site	a	b	b	b	f	-core	-interm	-rim	-core	-rim	f	b, -core	b, -rim	e
Metamorphic stage	M1	M2	M2		progr.	progr.	peak	retrogr. b-schist	progr.	peak	progr.	retrogr. b-schist	retrogr. amphib	retrogr. g-schist
Sample	Beig	Beig	Beig	Beig	Vol	Vol	Vol	Vol	Vol	Vol	Vol	Vol	Vol	Vol
SiO_2	29.91	30.86	31.10	38.02	37.66	35.66	35.63	36.26	54.65	55.44	48.69	56.44	43.37	52.53
TiO_2	40.78	38.68	37.46	0.14	0.10	0.15	0.09	0.15	0.04	0.11	0.09	0.01	0.29	0.06
Al_2O_3	1.33	0.84	1.42	27.46	24.64	20.96	20.62	20.72	3.70	9.03	5.09	9.85	11.36	4.61
Cr_2O_3	n.a.	0.05	0.00	0.00	n.d.	n.d.	n.d.	n.d.	0.00	0.05	0.00	0.04	0.00	
MgO	n.a.	0.00	0.00	0.07	0.01	0.72	0.49	0.39	8.36	5.59	5.89	8.91	6.52	14.29
CaO	28.16	28.49	28.42	23.11	22.61	4.42	5.61	6.30	14.92	11.71	10.73	1.18	8.63	9.28
MnO	n.a.	0.00	0.04	0.50	0.29	0.43	2.35	6.92	0.12	0.00	0.56	0.16	0.18	0.00
FeO	0.24	0.34	0.35	6.74	11.95	38.83	35.51	30.29	13.01	11.30	25.70	14.33	23.53	13.54
Na_2O	n.a.	0.02	0.03	0.01	0.00	0.01	0.00	0.02	5.67	7.80	1.13	6.62	4.00	2.48
K_2O	n.a.	0.00	0.00	0.01	0.00	0.00	0.00	0.00	0.00	0.00	0.19	0.05	0.52	0.06
Total	100.80	99.74	99.35	96.04	97.26	101.19	100.36	101.04	100.47	101.02	97.97	97.59	98.41	96.62
F. Struct.	1 ct	1 ct	1 ct	12.5 ox	12.5 ox	8 ct	8 ct	8 ct	6 ox	6 ox	23 ox	23 ox	23 ox	23 ox
Si	1.00	1.01	1.02	2.99	2.97	5.63	5.68	5.76	2.00	1.99	7.45	7.87	6.28	7.62
Ti	0.98	0.96	0.93	0.01	0.01	0.02	0.01	0.02	0.00	0.00	0.01	0.00	0.03	0.01
Al	0.06	0.03	0.06	2.55	2.29	3.90	3.87	3.88	0.16	0.38	0.92	1.62	1.94	0.79
Cr		0.00	0.00	0.00	0.00				0.00	0.00	0.00	0.00	0.00	0.00
Mg				0.01	0.00	0.17	0.12	0.09	0.46	0.30	1.34	1.85	1.41	3.06
Ca	0.99	1.00	1.00	1.95	1.91	0.75	0.96	1.07	0.58	0.45	1.76	0.18	1.34	1.44
Mn		0.00	0.00	0.03	0.02	0.06	0.32	0.93	0.00	0.00	0.07	0.02	0.02	0.00
Fe^{3+}				0.44	0.79	0.10	0.13	0.12	0.25	0.18	0.19	0.42	2.46	0.23
Fe^{2+}	0.01	0.01	0.01			5.02	4.61	3.90	0.15	0.16	3.07	1.25	0.39	1.39
Na		0.00	0.00	0.00	0.00	0.00	0.00	0.00	0.40	0.54	0.34	1.79	1.12	0.70
K		0.00	0.00	0.00	0.00	0.00	0.00	0.00	0.00	0.00	0.02	0.01	0.10	0.01
XGrs						0.12	0.16	0.18						
XPrp						0.03	0.02	0.02						
XAlm						0.84	0.77	0.65						
XSps						0.01	0.05	0.16						
XDi									0.43	0.29				
XHd									0.14	0.15				
XJd									0.15	0.36				

[a]Abbreviations are as follows: a, relict; b, along foliation; c, S1 relict hinge; d, inclusion in titanite; e, static overgrowth; f, inclusion in garnet; n.a., not analyzed; n.d., not detected; XMg = (Mg/(Mg+Fe^{2+}+Mn)).

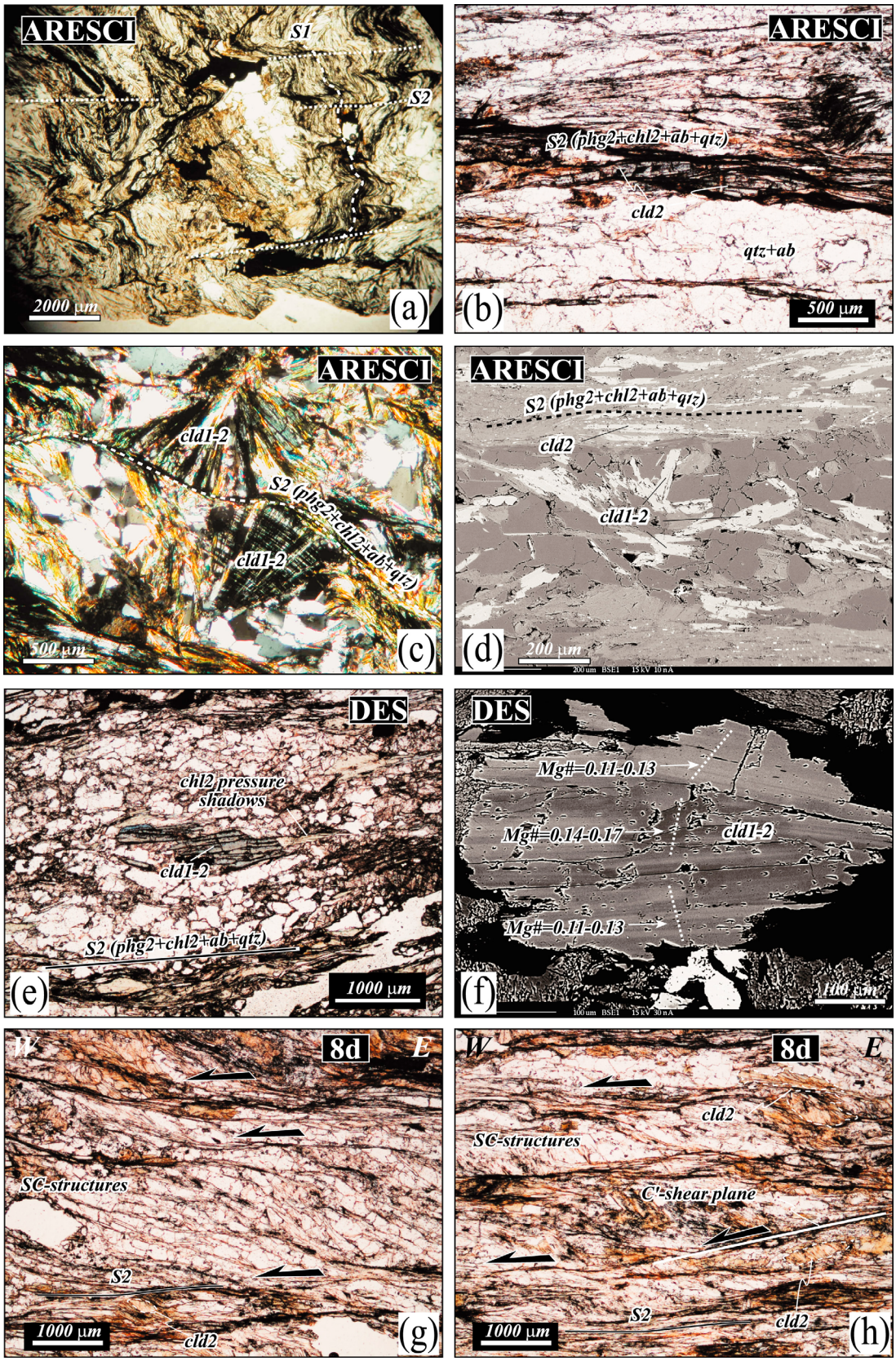
ARESCI
S1
S2
2000 µm
(a)
ARESCI
S2 (phg2+chl2+ab+qtz)
cld2
qtz+ab
500 µm
(b)
ARESCI
cld1-2
S2 (phg2+chl2+ab+qtz)
cld1-2
500 µm
(c)
ARESCI
S2 (phg2+chl2+ab+qtz)
cld2
cld1-2
200 µm
(d)
DES
chl2 pressure shadows
cld1-2
S2 (phg2+chl2+ab+qtz)
1000 µm
(e)
DES
Mg#=0.11-0.13
Mg#=0.14-0.17
cld1-2
Mg#=0.11-0.13
100 µm
(f)
W
8d
E
SC-structures
S2
1000 µm
cld2
(g)
W
8d
E
cld2
SC-structures
C'-shear plane
S2
1000 µm
cld2
(h)

Figure 5

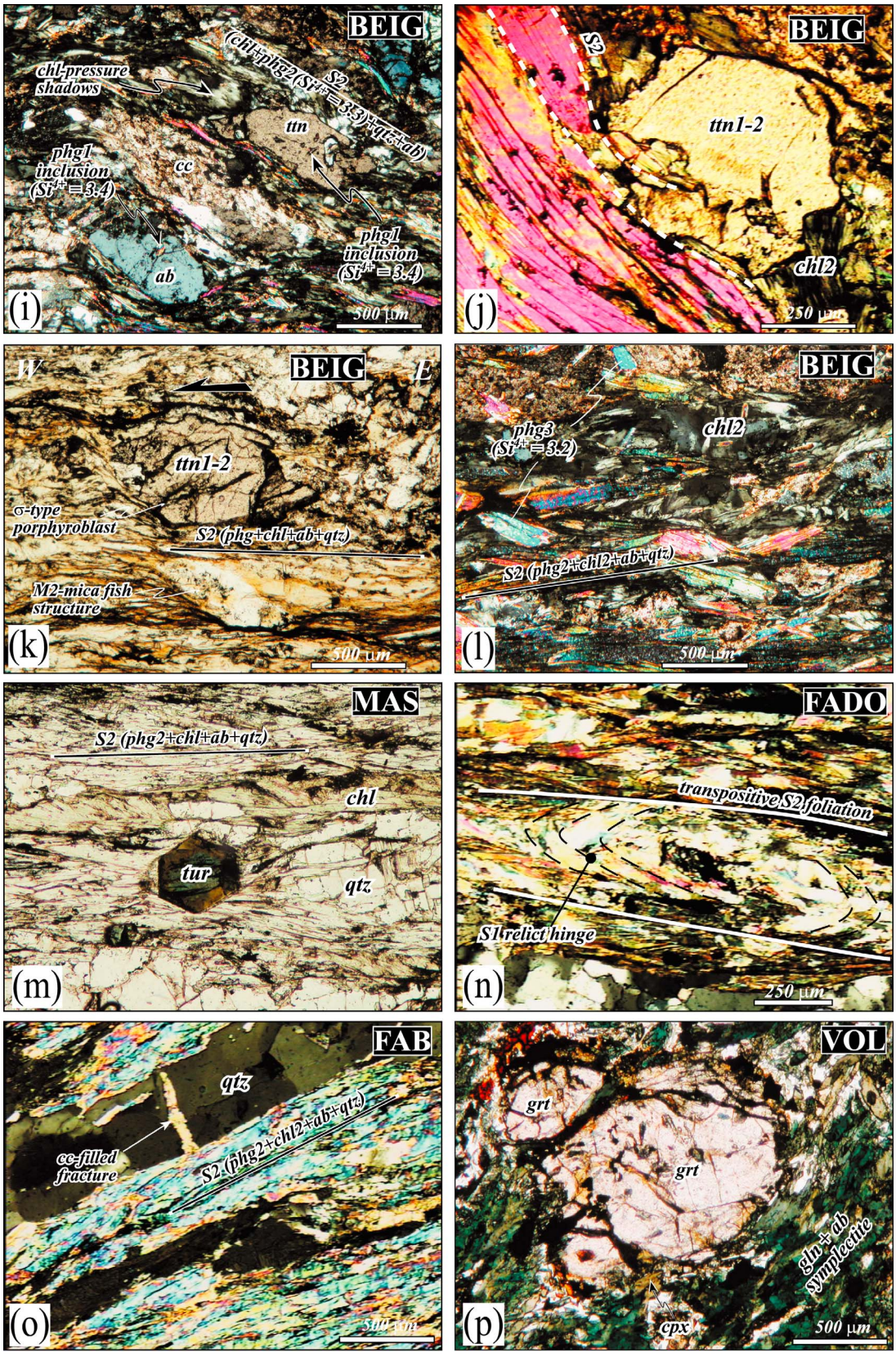

Figure 5. (continued)

sense of shear in accord with other kinematic indicators (oblique foliations, mica fish structures; Figure 5k). The youngest metamorphic stage (M_3) is mainly represented by the static growth of phg_3 (Si^{4+} = 3.2–3.1) and oxides, commonly oriented across the main S_2 foliation (Figure 5l). Calcite-filled veins are also observed cutting the S_2 foliation. This mineralogical assemblage is not associated with a detectable structural fabric.

[23] *Sample MAS* was collected from a mylonitic horizon characterized by a steeply dipping main foliation, at the east of the eclogitic core (Figures 2 and 3). This outcrop is characterized by a composite fabric showing a continuum from ductile to brittle deformation, as revealed by the superimposition of different ab + qtz veins that record progressive vertical orientation of the main S_2 foliation [see also *Crispini and Frezzotti*, 1998; *Vignaroli et al.*, 2009a]. Microscale observations reveal that the S_1 fabric is extensively overprinted, with only phg_1 relicts (Si^{4+} = 3.5–3.6) recognized. The S_2 schistosity is defined by composite assemblages of phg_2 + chl_2 + ab + qtz. Mylonitization produces mineralogical repartition between phyllosilicates (defined by fine-grained phg_2 and large flakes of chl_2) and qtz + ab-rich levels (Figure 5m). Compositionally, phg_2 has low Si^{4+} contents (3.3–3.4). Large crystals of tourmaline are widespread in the sample. The tourmaline crystals show euhedral shapes, with sharp boundaries and clear chemical zoning (Figure 5m), suggesting textural equilibrium with the D_2 fabric. Titanite and apatite are common accessory minerals.

[24] *Samples FAB and FADO* were selected from calc-schist unit showing structural, textural, and petrographic characteristics similar to those of sample MAS. At the outcrop scale, the main fabric is composed by a near vertical S_2 foliation and a weak stretching lineation (L_2). The L_2 is defined by cal and phg_2. D_3 folds refold the D_2 fabric, with axes trending near parallel to L_2. Calcite-filled fractures are widespread, indicating brittle deformation during exhumation. At the microscale, the D_1 fabric is defined by relict fold hinges in which phg_1 and chl_1 (plus qtz and cal) are present (Figure 5n). A mineralogical repartition between phyllosilicate-rich levels and qtz-rich levels defines the S_2 foliation (Figure 5o). Fine-grained phg_2 (in association with chl_2 and cal) forms the phyllosilicate-rich zones. Sets of calcite-filled fractures occur perpendicular to S_2, indicating extension parallel to the foliation. The D_2 fabric exhibits a dominant coaxial deformation style. Accessory minerals include titanite and zircon, of uncertain textural association.

[25] Mineral chemistry data obtained for the metasediments show that cld compositions range between $0.10 < X_{Mg} < 0.16$, with low Mn contents (Figure 6). In sample DES, a clear compositional variation from Mg-rich cores to Mg-poor rims is present in large cld grains. This zonation suggests a decrease of P-T conditions from core to rim, and it seems reasonable to consider the rim composition as chemically equilibrated during the transition from the M_1 to the M_2 metamorphic stage (compare with stage C of *Cimmino and Messiga* [1979]). The Si^{4+} substitution in phg can be correlated with the metamorphic stage at which crystallization occurred [e.g., *Massonne and Schreyer*, 1987; *Oberhänsli et al.*, 1995]. For each sample, decreasing Si^{4+} contents were observed from phg_1 to phg_2, to phg_3. The decrease of the Si^{4+} is accompanied by a concomitant decrease in Mg levels and an increase of the Al content due to celadonite substitution (Figure 6) [see also *Cimmino and Messiga*, 1979; *Barbieri et al.*, 2003; *Carrapa et al.*, 2004; *Federico et al.*, 2005]. Finally, chl shows significant chemical variations, even in single samples (Figure 6).

5.2. Beigua Eclogite

[26] *Sample VOL* was collected from an eclogitic lens on the southwestern flank of Mount Beigua (Figure 2a), below the mylonitic shear zone represented by sample BEIG. The enveloping serpentinite matrix shows a *SL* fabric equilibrated under retrogressive greenschist facies conditions. This retrogressive structural fabric is not pervasive within the eclogitic boudins. The sample is characterized by a massive texture and is composed of garnet and omphacite. Garnet (up to 1 mm) is almandine-rich with Mn-rich cores, and contains inclusions of calcic amphibole, sodic/calcic amphibole, epidote and paragonite. Both garnet and omphacite were extensively altered by the retrogressive metamorphic overprint (forming amphibole + plagioclase symplectites). The retrogressive polyphase assemblages indicate an evolution from epidote blueschist to low-grade

Figure 5. Microscale composite ductile fabric observed in the selected samples. Sample ARESCI: (a) D_2 crenulation of the S_1 foliation, (b) elongated cld_2 porphyroblast aligned along the S_2 mylonitic foliation, (c) cld_{1-2} flake intergrown with phg_2+chl+qtz+ab foliation, and (d) backscattered electron (BSE) image showing orthogonal (cld_{1-2}) and parallel (cld_2) chloritoid growth with respect to the S_2 foliation. Sample DES: (e) cld_{1-2} porphyroblast within the S_2 foliation, showing chl_2 pressure shadows, and (f) BSE image of chemically zoned cld_{1-2}. Sample 8D: (g, h) noncoaxial, top-to-the-west shearing of D_2-related fabric as indicated by *SC* structures, *C'* planes, and oblique foliations. Chloritoid tends to be oriented along the shear planes. Sample BEIG: (i) syngreenschist S_2 foliation showing albite and titanite porphyroblasts containing M_1 inclusions of phg_1; (j) pre-D_2 to syn-D_2 titanite porphyroblast along the S_2 main foliation as indicated by geometric relationships between external and internal foliations in titanite; (k) σ-type titanite porphyroblasts, mica fish structure, and oblique foliations indicating top-to-the-west shearing; and (l) static crystallization of large phg_3 grains oblique to the S_2 foliation. Sample MAS: (m) basal section of tourmaline crystal enveloped by the S_2 foliation, which consists of phg_2 and chl_2 zones (together with albite and quartz). Sample FADO: (n) S_1 relict foliation folded and transposed along S_2. Sample FAB: (o) D_2 mylonitic foliation composed of alternating phyllosilicates-rich and qtz-dominant layers. Calcite-filled fractures are common. Sample VOL: (p) eclogitic texture consisting of large garnet and omphacite relicts overprinted by polyphase retrogressive Na- and Na/Ca-amphibole bearing assemblages. Microphotographs in Figures 5a, 5b, 5e, 5g, 5h, 5k, and 5m were taken in natural light; microphotographs in Figures 5c, 5i, 5j, 5l, 5n, 5o, and 5p were taken using crossed polars.

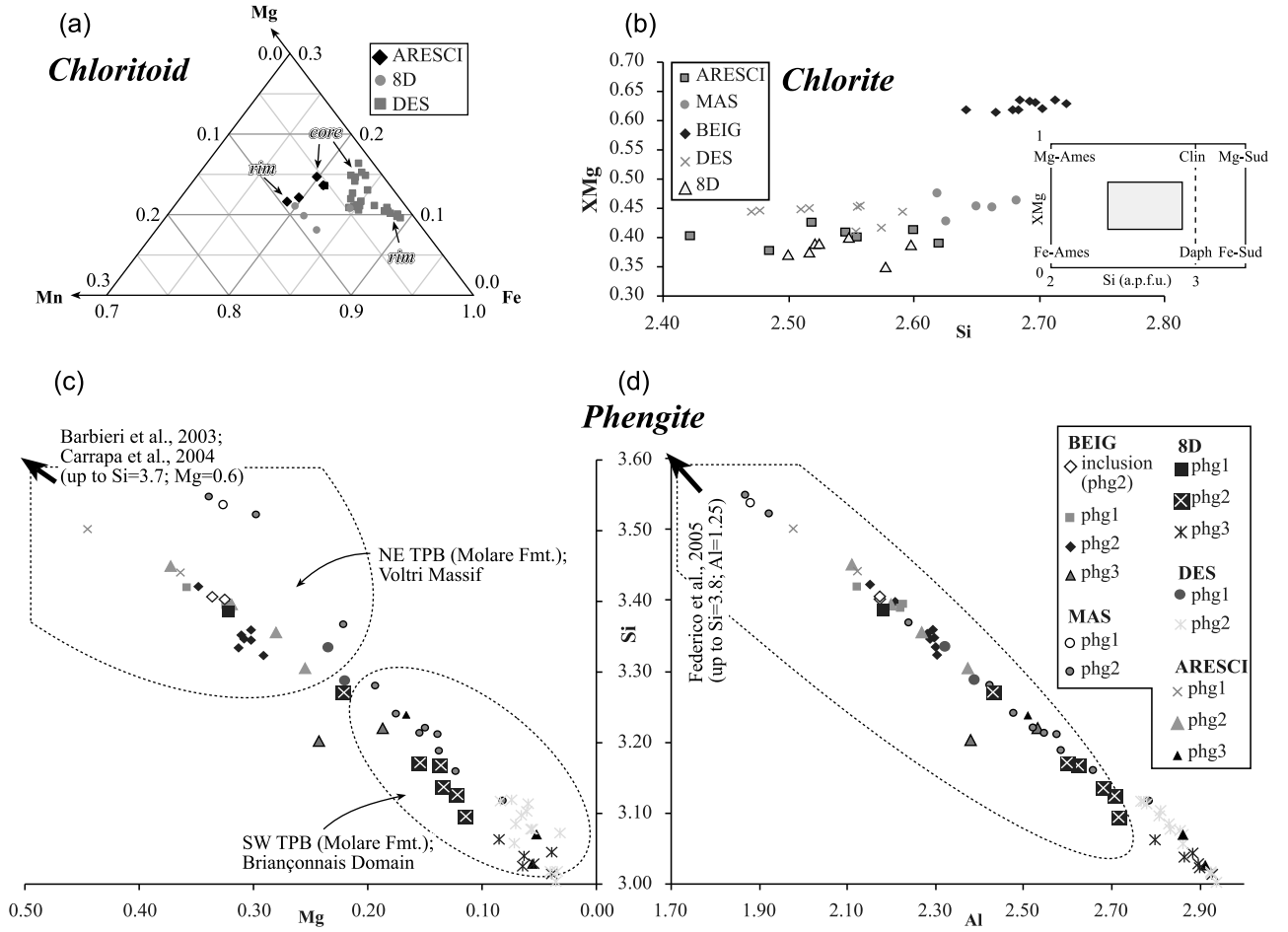

Figure 6. Chemical composition of (a) chloritoid, (b) chlorite, and (c, d) phengite from the Voltri-Rossiglione metasediments. Chloritoid shows a low Mg#, increasing from core to rim in all samples. Chlorite is characterized by a wide range of Si content. The higher Mg# and Si values in chlorite from sample BEIG are interpreted as indicating a higher degree in recrystallization. The chemical trend of phengite is characterized by progressively decreasing Mg# and Si, with increasing Al, from phg_1 to phg_2, to phg_3.

greenschist facies conditions (Figure 5p). The mesotextural and microtextural characteristics, mineral chemistry and metamorphic evolution of the eclogites are described in detail by *Vignaroli et al.* [2005].

6. Metamorphic Petrology

[27] Depending on the parageneses, metamorphic equilibria were calculated for two independent compositional systems: (1) the K_2O-FeO-MgO-Al_2O_3-SiO_2-H_2O (KFMASH) system, in the case of cld-bearing assemblages (samples 8D, ARESCI, DES), and (2) the Na_2O-K_2O-FeO-MgO-Al_2O_3-SiO_2-H_2O (NKFMASH) system, in the case of cld-absent assemblages considering Na phase components (samples BEIG, MAS) (Figure 7). In these calculations, pressure estimates mainly depend on the Tschermak content of muscovite (expressed as the Si^{4+} a.p.f.u. content), which can be expressed by the equilibria for cld bearing and the assemblages considering Na phase components, respectively [e.g., *Massonne and Schreyer*, 1987; *Oberhänsli et al.*, 1995; *Bousquet et al.*, 2002]:

$$3\mathrm{Cld} + 2\mathrm{Phg} = 2\mathrm{W} + 5\mathrm{Qtz} + \mathrm{Chl} + 2\mathrm{Ms},$$

$$\mathrm{Phg} + \mathrm{Pg} = \mathrm{Chl} + \mathrm{Ms} + \mathrm{Ab}.$$

For cld-bearing assemblages, temperatures were also estimated on the basis of Fe-Mg exchange between chl-cld pairs, following the equilibrium reaction [*Vidal et al.*, 1999]:

$$\mathrm{Cln} + 5\mathrm{Fe} - \mathrm{Cld} = \mathrm{Dph} + 5\mathrm{Mg} - \mathrm{Cld}.$$

[28] The variation in P-T conditions attained during progressive exhumation of the Voltri Rossiglione Unit was estimated from calculations with the thermodynamic data set of the TWQ database [*Berman*, 1988] (see also software version 2.02 of *Berman* [1991]). An updated TWQ database

implements the nonideal solution models of *Vidal et al.* [2001] for chlorite, and the *Parra et al.* [2002] model for phengite. Evaluation of ferric iron contents in chlorite and phengite was achieved according to the activity models after *Vidal et al.* [2005]. The calculation was conducted on the cld-chl-phg-qtz (cld-bearing) and the chl-phg-qtz (cld-absent) assemblages, with specific attention given to (1) the textural relationships at the thin section scale (Figure 5) and (2) the chemical zoning of the minerals (Figure 6) [see also *Rimmelé et al.*, 2005]. In particular, the core composition of chloritoid was systematically associated with the composition of phg_1 (higher-Si^{4+} content) found in relic transposed structures or as inclusions (Figure 5). Lower-Si^{4+} phengite was considered to have crystallized during growth of chloritoid rims. Within each sample, the chemical variation of chlorite affected the temperature estimates by about ± 50°C. Where there was ambiguity in the textural interpretation (e.g., chl_1 or chl_2), we assumed that chlorite with higher Si^{4+} content crystallized during the M_1 stage, together with cld_1 and phg_1.

[29] For cld-bearing assemblages (samples 8D, ARESCI, DES), the considered end-members are (1) Fe- and Mg-chloritoid; (2) daphnite (daph: $Fe_5Al_2Si_3O_{10}[OH]_8$), clinochlore (cln: $Mg_5Al_2Si_3O_{10}[OH]_8$), for chlorite; and (3) Mg-Al-celadonite (Al-cel: $KMgAlSi_4O_{10}[OH]_2$) and muscovite (ms: $KAl_3Si_3O_{10}[OH]_2$) for micas. For the calculation for cld-absent assemblages (samples BEIG, MAS), the considered end-members are (1) daphnite, clinochlore, Fe-Al-amesite (Fe-am: $Fe_4Al_4Si_2O_{10}[OH]_8$) and Mg-Al-amesite (Al-am: $Mg_4Al_4Si_2O_{10}[OH]_8$) for chlorite; and (2) Fe-celadonite (Fe-cel: $KFeAlSi_4O_{10}[OH]_2$), Mg-Al-celadonite, muscovite and pyrophyllite (prp: $Al_2Si_4O_{10}[OH]_2$) for micas. Due to the difficulty in estimating the Fe^{2+}/Fe^{3+} in the pyrophyllite and Fe-Al-celadonite in white K-mica as well as amesite in chlorite, the uncertainty of P-T calculation involving these components is also larger. The P-T values (Figure 7) resulted from the intersections of univariant equilibria in the P-T field. The uncertainties of the P-T data were calculated using the InterSX program included in TWQ package. Intersections outside 1.5σ error windows were discarded. This resulted in two linearly independent univariant equilibria for the cld-bearing assemblages and three linearly independent curves for the cld-absent assemblages.

[30] For samples 8D and ARESCI, application of the TWQv2.02 method to the cld-chl-phg assemblages provides a section of a partial P-T loop ranging from 17 kbar/500°C to 3 kbar/400°C (Figure 7a) and 19 kbar/555°C to 8.5 kbar/470°C (Figure 7b), respectively. Systematically, higher P and T values were obtained when using high Si^{4+} phengites (corresponding to phg_1) in association with the core compositions of relict chloritoid (cld_1) or the core compositions of chloritoid oriented along the S_2 foliation. Conversely, lower P-T estimates result when low-X_{Mg} (rim compositions of) chloritoid was associated with phg_2 (marking the S_2 foliation). For sample DES, a limited number of intersections were achieved when phg_1 was combined with chloritoid core compositions, giving results in the range of 480°C–520°C and 12–14 kbar (Figure 7c). For samples BEIG and MAS, the best P-T constraints were provided by the chlorite white mica multiequilibria and range from 360°C to 500°C over 10 to 4.5 kbar (Figures 7d and 7e). As above, higher pressure values depend of the high-Si phengite used in the computation (phg_1; Table 2) in association with the compositions of adjacent chlorite (Figure 5). Higher temperature values resulted from higher-Mg chlorites. Equilibria intersections at T > 500°C were discarded because of the very low pyrophyllite content in white micas [*Agard et al.*, 2001].

7. Geochronology

7.1. U-Pb SHRIMP Geochronology and Trace Elements

[31] Zircon and titanite crystals were separated on the basis of their magnetic properties and density. Separated grains were mounted in epoxy and polished down to expose the grain centers. Zoning of zircon was investigated by cathodoluminescence (CL), using a HITACHI S2250-N scanning electron microscope at the Electron Microscope Unit (Australian National University), and operating conditions of 15 kV, ~ 60 μA and ~ 20 mm working distance. Titanite internal structures were revealed by backscattered electron (BSE) images using a Cambridge S360 scanning electron microscope operated at 20 kV, 3 nA and 20 mm working distance. Selected domains were analyzed for U, Th and Pb using the sensitive high-resolution ion microprobe (SHRIMP II) at the Research School of Earth Sciences (ANU), with the instrumental conditions and data acquisition described by *Compston et al.* [1992] and *Rubatto and Hermann* [2001]. Details of the analytical protocols are provided in section A2; analytical results are shown on Tables 3 and 4.

7.1.1. Metasedimentary Zircons

[32] Sample BEIG contains large (≤600 μm) zircon crystals that are yellowish, clear, inclusion-free and euhedral to subeuhedral. CL images revealed two types of domains (Figure 8a). The majority of the crystals exhibit weak polygonal, oscillatory to sector zoning. Rare, discontinuous, unzoned, dark CL domains located at the rims of crystals crosscut the oscillatory zoning. Both domains were analyzed for U-Pb dating (Table 3). The zoned domains have low U and Th contents (5–44 and 2–14 ppm, respectively). The low amount of radiogenic Pb measured was variably contaminated by common Pb (2–20%). Five analyses on zoned domains yielded ages between 148 and 160 Ma with a mean $^{206}Pb/^{238}U$ age of 153 ± 4 Ma (95% c.l.; MSWD = 0.85). Two other analyses yielded Late Cretaceous ages and are suspected of having undergone Pb loss.

[33] The crosscutting dark rims are much richer in U and have similar Th content with respect to the zoned domains, resulting in a low Th/U of 0.02–0.01. Six analyses returned ages between 34 and 36 Ma with limited common Pb contamination (<5%). In a *Tera and Wasserburg* [1972] diagram, uncorrected data define a regression line with a mean age intersection of 33.8 ± 0.8 Ma (MSWD = 0.5) and an initial $^{207}Pb/^{206}Pb$ of 0.39 (Figure 8c). This low $^{207}Pb/^{206}Pb$ value implies that the initial Pb was a mixture of common and radiogenic Pb, and confirms that intrinsic initial Pb was

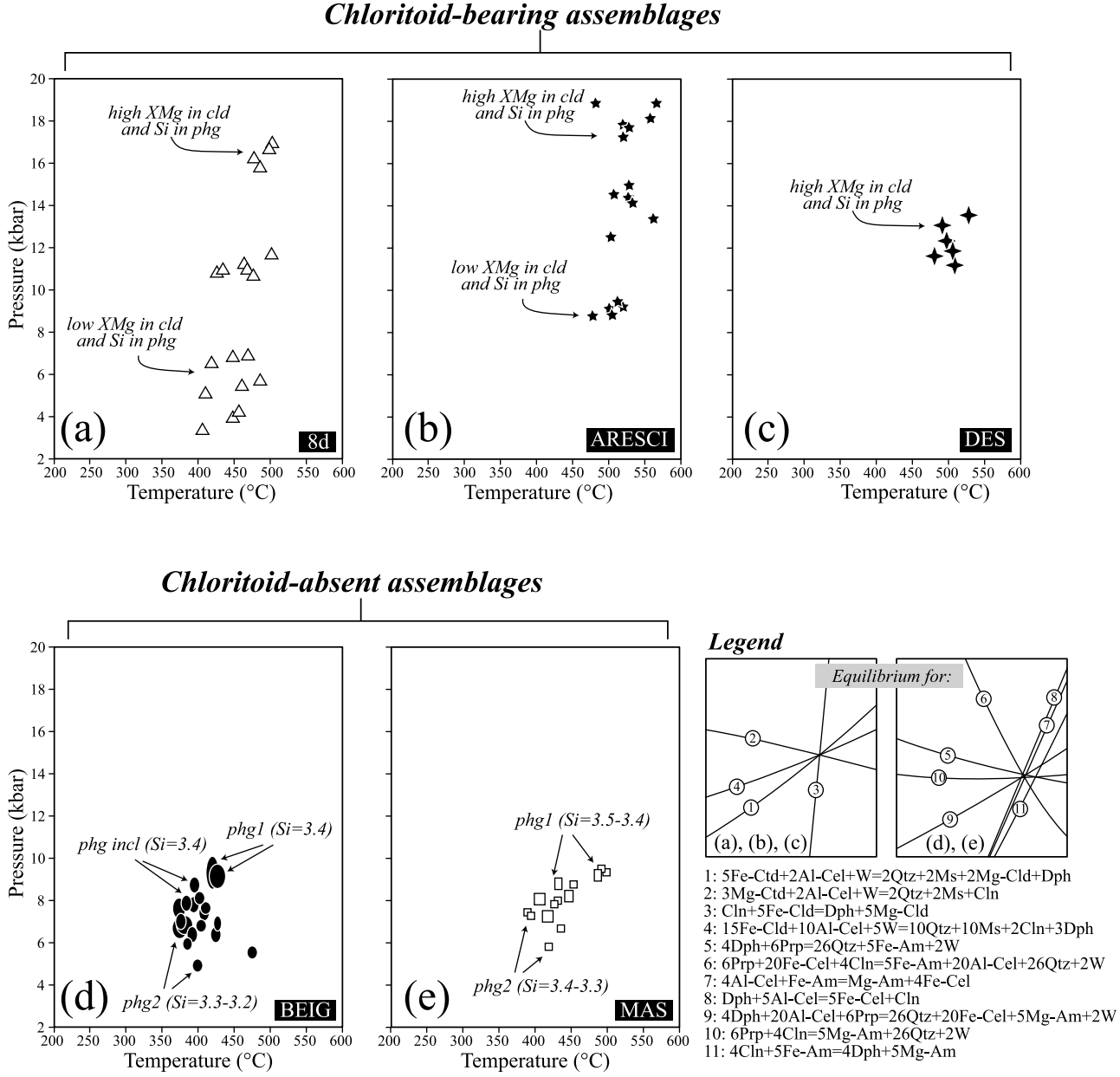

Figure 7. P-T quantitative thermobarometry obtained from chl-phg univariant equilibria using the TWQ software [*Berman*, 1991] for both (a–c) cld-bearing and (d, e) cld-absent assemblages. Symbols in the P-T diagrams represent the midpoints of the equilibrium intersections. See text for details on mineral parageneses and end-members.

hosted in zircon. The presence of initial Pb in the zircon rims is in line with the measurement of larger absolute amounts of "common" Pb in this domain with respect to the common Pb-free standard. A regression forced to 35 Ma common Pb [*Stacey and Kramers*, 1975] would result in a poor MSWD of 4.8 and an age of 35.2 ± 1.1 Ma, which is still within error of the preferred age of 33.8 ± 0.8 Ma.

[34] Trace element analyses performed on the zircon cores yielded high Th/U (0.20–0.43), low content of U (4–37 ppm), Ti between 6 and 20 ppm, and elevated values of Y (1001–4501 ppm). The chondrite-normalized patterns show a positive Ce anomaly and a negative Eu anomaly (Table 4). The general pattern is characterized by a moderate enrichment from LREE to HREE (Lu/Gd normalized: 13–30; Figure 8d). The zircon rims, in contrast, have lower contents in all the trace elements measured with the exception of U, which is significantly higher than in the cores (586–798 ppm); for example, P and Y are very low (26–31 and 106–149 ppm, respectively), Ti is mostly at or below the detection limit of 3 ppm, and the LREE could not be detected. The REE pattern from the rims is characterized by a very strong enrichment in HREE with respect to MREE (Lu/Gd 314–997;

Table 3. U, Th, and Pb SHRIMP Analyses on Zircon and Titanite

	U (ppm)	Th (ppm)	$^{232}Th/^{238}U$	Common ^{206}Pb (%)	Total $^{238}U/^{206}Pb$	err (%)	Total $^{207}Pb/^{206}Pb$	err (%)	Corr $^{206}Pb/^{238}U$	err (%)	Age ^{207}Pbcorr $^{206}Pb/^{238}U$ (Ma)	err (1σ)
Zircon												
From metasediments: magmatic core												
BEIG_1.2	5	2	0.31	13	34.90	4.3	0.15	9.4	0.0287	4.3	160	8
BEIG_3.1	11	5	0.44	19	34.74	5.5	0.20	15	0.0287	5.5	148	11
BEIG_5.1	36	14	0.41	7	37.68	2.2	0.11	7.9	0.0265	2.2	157	4
BEIG_5.2	40	11	0.30	6	40.40	2.2	0.10	13	0.0248	2.2	148	4
BEIG_9.1	31	11	0.38	5	40.19	2.3	0.09	12	0.0249	2.3	151	4
BEIG_4.1	40	9	0.22	11	59.45	2.7	0.13	9.1	0.0168	2.7	98[a]	4
BEIG_4.2	44	8	0.19	8	59.87	3.1	0.11	14	0.0167	3.1	98[a]	4
From metasediments: metamorphic rim												
BEIG_1.1	714	10	0.014	4.5	170.4	1.0	0.082	3.3	0.0059	1.0	36.1	0.4
BEIG_1.3	935	8	0.0084	0.77	188.0	1.0	0.053	4.3	0.0532	1.0	33.9	0.3
BEIG_1.4	824	9	0.011	1.2	183.9	1.5	0.056	3.7	0.0544	1.5	34.6	0.5
BEIG_3.2	377	7	0.0203	4.8	169.9	1.5	0.085	5.4	0.0589	1.5	36.0	0.6
BEIG_6.1	712	3	0.0045	3.2	172.5	1.5	0.072	2.7	0.0579	1.5	36.1	0.5
BEIG_8.1	488	10	0.022	3.4	175.1	1.6	0.073	7.3	0.0571	1.6	35.5	0.6
From eclogite: magmatic core												
VOL_1.1	5	1	0.22	59	38.35	5.2	0.31	11	0.0261	5.2	112[a]	10
VOL_2.1	5	2	0.31	34	36.66	4.9	0.29	13	0.0273	4.9	122[a]	10
VOL_2.2	11	4	0.35	13	35.82	3.5	0.17	13	0.0279	3.5	151	7
VOL_3.1	13	4	0.32	65	10.30	6.6	0.76	5.4	0.0971	6.6	63[a]	34
VOL_4.1	3	1	0.22	23	33.19	11	0.33	8.2	0.0301	11	124[a]	15
VOL_5.1	17	2	0.11	46	58.62	3.2	0.24	14	0.0171	3.2	82[a]	5
VOL_6.1	16	2	0.12	66	20.05	2.8	0.67	2.7	0.0499	2.8	70[a]	9
VOL_7.1	18	1	0.072	6.4	61.60	3.3	0.34	6.2	0.0162	3.3	66[a]	4
VOL_8.1	4	1	0.19	190	27.78	5.8	0.28	14	0.0359	5.8	162	15
VOL_9.1	6	1	0.27	76	30.66	7.7	0.31	10	0.0326	7.7	142	13
Titanite From Metasediments: Metamorphic Growth												
BEIG_1.1	23	14	0.63	96	3.787	2.7	0.82	0.8				
BEIG_2.1	11	4	0.42	97	2.305	2.8	0.83	0.6				
BEIG_4.1	12	22	1.81	90	21.59	3.3	0.76	1.7				
BEIG_7.1	150	51	0.35	93	13.06	1.3	0.79	0.5				
BEIG_8.1	23	12	0.54	96	2.383	2.1	0.83	0.4				
BEIG_9.1	41	25	0.64	97	3.849	2.7	0.82	0.5				
BEIG_10.1	32	21	0.66	97	4.598	1.7	0.82	0.4				
BEIG_11.1	42	27	0.66	96	4.749	1.6	0.82	0.4				
BEIG_13.1	49	42	0.89	96	5.586	12	0.82	0.4				
BEIG_14.1	16	8	0.53	96	2.244	2.3	0.82	0.4				
BEIG_16.1	33	18	0.56	97	4.808	2.6	0.82	0.5				
BEIG_18.1	15	11	0.76	96	1.708	2.8	0.83	0.5				

[a]Data excluded from the average age calculation.

Figure 8d). Ce and Eu anomalies could not be quantified because these elements are below detection limits. However, if the limit of detection for Eu is used as a maximum concentration, values for Eu/Eu* as low as 0.28 and 0.56 can be calculated for the two analyses.

7.1.2. Metasedimentary Titanite

[35] Titanite crystals recovered from sample BEIG are up to 200 μm in size and are elongated. BSE imaging reveals that titanite displays minimal zoning with only a few grains having brighter sectors (Figure 8b). SHRIMP analyses yielded low U and Th contents (mostly < 50 ppm) with Th/U between 0.3 and 1.8 (Table 3). The 13 analyses contained high levels of common lead (90–97%), which together with the low amount of radiogenic Pb produced large analytical errors. Nevertheless, because the common initial Pb component is well defined, the uncorrected analyses can be plotted on a *Tera and Wasserburg* [1972] diagram where they define a single mixing line with a radiogenic component corresponding to an age of 29 ± 5 Ma (95% c.l.; MSWD = 0.82; Figure 8c). Despite the analytical problems associated with these analyses, the results, even though imprecise, are sufficient to indicate an Oligocene age for the formation of the titanite.

[36] Laser ablation analyses of titanite show little variation in Ca and Al, indicating a homogenous population. Measured Th and U are comparable to SHRIMP analyses and confirm that bright BSE domains are richer in these elements. Chondrite-normalized patterns (Figure 8e) show a general depletion of the LREE with respect to the other REE, which define a fairly flat pattern. A couple of analyses on dated Eocene titanite have higher REE and dome-shaped profiles with higher values for the MREE (Lu/Gd 0.2–0.3).

Table 4. Laser Ablation ICPMS Trace Elements Analyses of Titanite and Zircon (Values in ppm)

	Ti	Y	Zr	Nb	La	Ce	Pr	Nd	Sm	Eu	Gd	Tb	Dy	Ho	Er	Tm	Yb	Lu	Hf	Ta	Th	U
Zircons																						
BEIG1rim	<3.40	143	-	3.78	<0.02	0.13	<0.01	<0.09	<0.07	<0.02	0.28	0.25	5.75	3.76	28.7	9.13	136	34.5	10257	0.69	8.38	770
BEIG2rim	3.23	107	-	4.47	<0.02	0.14	<0.01	<0.09	0.16	<0.02	0.27	0.22	4.36	2.92	20.9	7.43	109	28.5	9680	0.65	9.00	798
BEIG3rim	<2.50	149	-	3.28	<0.02	0.10	<0.01	<0.09	<0.07	0.04	0.36	0.28	5.81	3.93	28.8	9.50	142	35.9	9575	0.54	5.68	586
BEIG4rim	6.26	139	-	3.32	<0.02	0.40	<0.01	<0.09	0.24	<0.02	0.65	0.39	7.35	4.07	26.7	8.05	104	25.2	10796	1.35	4.23	753
BEIG10core	13.8	1433	-	0.49	<0.02	2.40	0.07	1.41	4.44	1.38	28.3	10.7	136	50.3	221	46.5	440	68.9	7072	0.19	1.87	5.21
BEIG11core	4.68	4501	-	1.31	2.87	24.8	2.21	18.1	18.1	3.20	91.2	34.2	422	159	692	142	1275	191	9611	0.61	15.9	37.8
BEIG12core	16.7	1335	-	0.47	<0.02	2.86	0.06	1.31	3.91	1.17	24.5	9.68	124	46.9	211	45.4	435	68.0	7874	0.20	2.09	5.79
BEIG13core	16.5	1088	-	0.38	<0.02	1.61	0.03	0.89	3.13	1.06	20.0	8.02	101	38.4	172	37.0	352	56.4	6584	0.15	1.11	3.59
BEIG1core	11.2	1001	-	0.40	<0.02	2.30	0.02	0.60	2.21	0.65	16.1	6.82	90.1	35.0	160	35.3	340	54.9	8241	0.15	1.06	4.51
BEIG4core	6.34	2756	-	1.01	0.57	11.7	0.93	9.52	15.3	5.65	73.9	26.0	301	106	472	90.0	821	118	10194	0.47	19.8	31.1
BEIG5core	19.5	1450	-	1.13	0.02	6.04	0.05	1.10	3.36	0.64	21.0	9.05	124	49.8	234	51.9	503	77.3	10416	0.55	5.36	26.7
Titanites																						
BEIG1	-	314	1.14	333	13.7	84.4	18.8	109	43.9	11.7	47.9	8.92	61.5	11.8	34.7	4.96	32.6	3.58	0.10	18.3	6.16	11.2
BEIG2	-	226	1.27	149	5.89	37.2	8.12	50.6	24.5	7.73	30.1	6.22	44.1	8.62	25.1	3.74	23.8	2.68	0.16	12.2	2.21	6.84
BEIG3	-	388	35.0	2222	10.7	53.6	10.7	59.0	28.1	11.6	36.1	8.23	64.5	13.6	42.3	6.51	41.9	4.44	8.39	229	0.02	3.94
BEIG4	-	1043	16.8	2129	99.0	667	138	756	259	56.2	238	43.6	264	45.8	118	15.5	87.9	8.28	1.56	197	119	78.0
BEIG5	-	408	3.96	486	16.3	97.5	21.0	119	47.8	14.6	55.2	10.9	75.7	14.6	44.6	6.57	39.6	4.38	0.45	33.4	7.46	13.9
BEIG6	-	410	1.62	467	12.7	74.1	15.8	89.9	40.3	14.4	48.1	10.4	77.3	15.4	45.1	6.39	38.2	3.86	0.13	18.7	1.27	5.74
BEIG7	-	1602	113	3014	44.6	326	76.7	523	293	74.7	397	72.2	423	69.1	165	20.3	112	11.4	14.4	298	19.0	60.8
BEIG8	-	652	171	3057	11.1	60.6	13.6	87.4	45.5	21.2	69.5	15.2	114	23.8	71.2	10.4	66.1	7.59	21.6	278	7.34	16.3
BEIG9	-	833	52.0	2563	19.8	101	21.3	125	58.9	24.8	84.6	18.1	137	28.9	88.6	13.3	85.0	9.78	10.9	239	13.0	23.3
BEIG10	-	722	292	3636	24.1	129	27.9	170	79.2	26.4	104	20.5	144	28.5	79.4	11.3	70.8	7.52	27.8	254	24.9	44.1
BEIG11	-	534	118	2975	19.8	117	25.0	149	68.3	20.4	80.9	15.5	107	20.6	57.8	8.38	52.5	5.66	20.3	347	16.3	29.7
BEIG12	-	388	106	2837	9.25	48.6	10.1	57.6	27.5	11.1	36.0	8.26	66.1	14.0	42.7	6.70	42.9	4.64	16.9	240	<0.02	3.50
BEIG13	-	898	12.4	2902	44.2	232	47.9	265	104	29.4	118	22.8	162	32.9	99.5	15.1	98.9	11.2	1.49	152	59.4	80.1
BEIG14	-	611	199	3423	23.3	141	31.1	183	77.5	21.3	88.5	16.7	115	23.3	67.9	9.97	62.8	6.86	21.7	306	6.15	14.0
BEIG15	-	404	29.7	2280	14.2	73.7	14.5	77.1	32.9	12.9	38.3	8.64	67.7	14.1	44.3	6.70	42.2	4.56	7.77	264	0.18	3.96
BEIG16	-	703	42.2	1745	17.0	110	25.1	157	77.9	25.1	96.0	20.2	141	28.2	80.1	11.9	72.6	7.58	11.0	382	13.39	27.2
BEIG17	-	404	272	2885	7.56	38.1	7.48	40.7	19.6	11.0	27.2	7.24	60.7	13.7	43.1	6.78	42.9	4.64	24.0	210	<0.02	1.76
BEIG18	-	448	46.9	2593	22.0	127	25.3	138	51.3	16.1	56.3	11.1	79.7	16.2	47.9	7.06	43.1	4.50	10.4	246	5.26	8.32
BEIG19	-	119	1.20	117	7.58	46.2	9.19	51.3	19.4	5.71	21.2	3.73	23.7	4.49	12.3	1.89	12.1	1.45	0.14	5.28	2.83	6.80
BEIG20	-	417	2.27	266	8.69	56.6	13.4	83.4	41.0	14.2	54.4	11.3	81.4	16.2	47.2	6.62	41.4	4.61	1.18	15.6	4.30	10.7
BEIG21	-	334	1.14	319	5.98	34.8	7.91	46.1	23.1	9.11	30.3	7.22	57.2	12.1	39.2	6.66	47.4	5.67	0.11	27.8	2.78	14.7
BEIG22	-	353	1.15	276	8.65	52.5	11.5	66.0	31.5	10.0	37.6	8.57	67.5	14.1	43.0	6.46	42.0	4.47	0.15	16.5	4.46	12.9

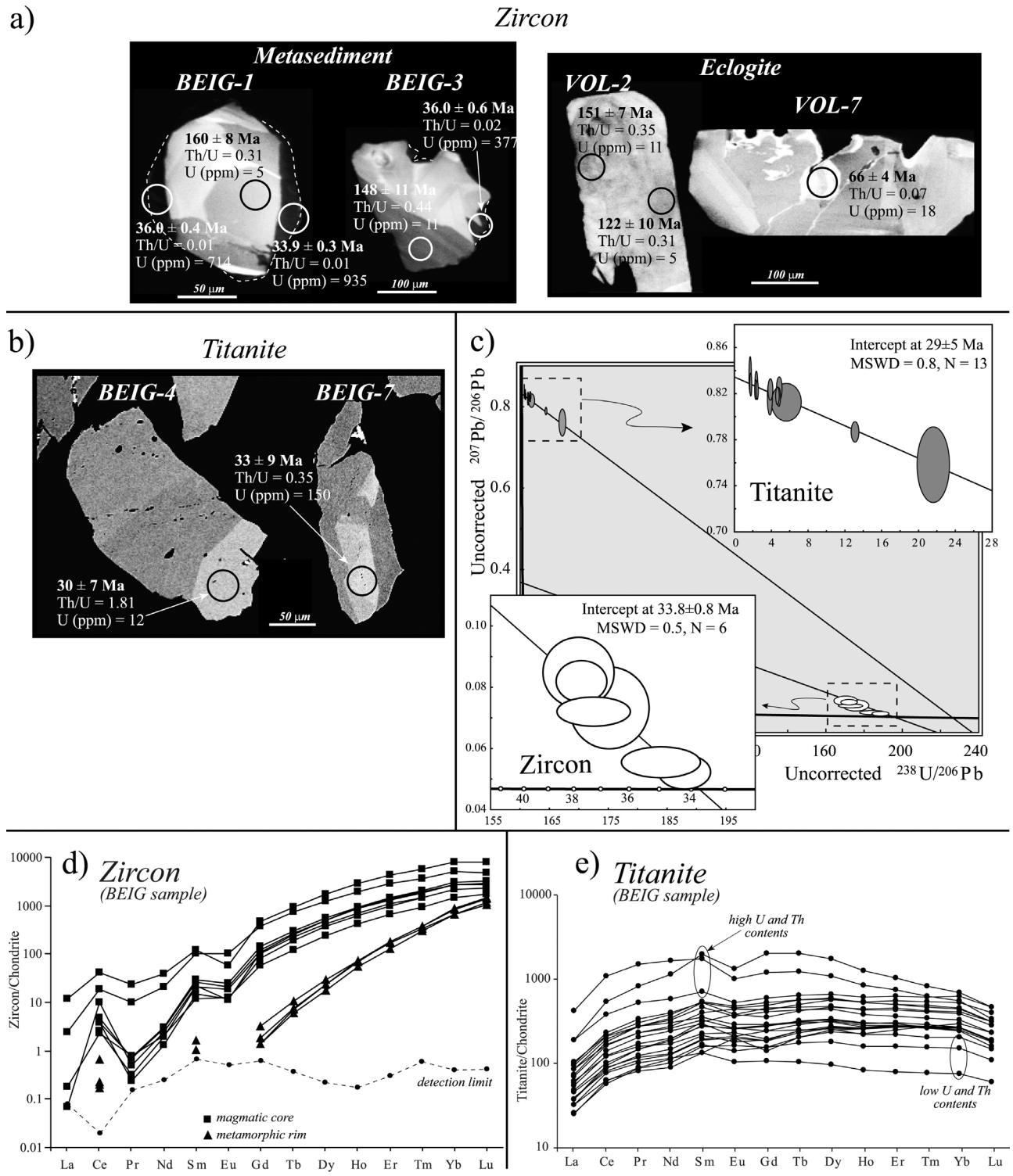

Figure 8. (a) CL image of representative zircon crystals analyzed, showing zoned (magmatic) core surrounded by a dark, discontinuous, unzoned rim of metamorphic origin. (b) BSE image of representative titanite grains analyzed. Circles represent loci of SHRIMP analysis pits. Ages are given with 1σ errors. (c) U-Pb diagram for metamorphic rims and titanite (Isoplot-Ex [*Ludwig*, 2000]); *y* axis intercepts indicate the common $^{207}Pb/^{206}Pb$ composition for the population. Average ages are reported at the 95% confidence level, and single data points are represented with 2σ ellipses. (d, e) Chondrite-normalized REE patterns with normalizing values according to *Sun and McDonough* [1989].

These analyses also have slightly negative Eu anomalies (Eu/Eu* 0.7).

7.1.3. Eclogite Zircon

[37] Zircons from the VOL sample are large (up to 600 μm), clear and elongated with preserved crystal faces. CL images reveal the presence of oscillatory and sector zoning, parallel to the crystal faces, often showing evidence of disturbance (VOL-2 in Figure 8a). Unzoned, CL bright zircon forms along fractures and around inclusions (VOL-7 in Figure 8a). Three analyses of domains that preserve zoning yielded very low U (<20 ppm) and Th contents, and Th/U of 0.19–0.35; the average $^{206}Pb/^{238}U$ age is 151 ± 11 Ma (MSWD = 0.5). A number of analyses were attempted on domains where the zoning appeared disturbed or on unzoned zircon with the intent of dating metamorphism: these analyses have U and Th compositions similar to the zoned domains, but yielded younger ages ranging between 124 and 63 Ma, without any significant clustering. Isolated ages at this level of precision cannot be proven to be analytically concordant and are interpreted as geologically insignificant. The scatter and the altered CL zoning suggest that these are apparent ages resulted from disturbance of the U-Pb system after magmatic crystallization at ~ 150 Ma. The disturbance likely occurred during Alpine metamorphism; however, no robust age constraints can be obtained from the studied sample in relation to this event.

7.2. The ^{40}Ar-^{39}Ar Geochronology

[38] The ^{40}Ar-^{39}Ar dating was performed on phengite separated from both cld-bearing (ARESCI and DES) and cld-absent (BEIG) samples. The presence of fine-grain-size white micas formed along microscale shear bands necessitated the use of bulk mineral separates for ^{40}Ar-^{39}Ar step heating and in situ laser probe analyses were not attempted. Analytical procedures are described in section A2. The step heating analyses yielded discordant age spectra for all samples (Figure 9). The age spectrum for sample ARESCI (Figure 9a) shows an overall convex downward shape with apparent ages initially increasing (steps 1–6) from 43.4 ± 3.6 Ma to 63.4 ± 0.6 Ma; Table 5), before declining to a minimum value of 28.3 ± 3.0 Ma (Table 5). Sample DES (Figure 9b) exhibits a similar spectrum with apparent ages initially increasing (steps 1–7) from 34.1 ± 4.2 Ma to 48.2 ± 0.2 Ma (Table 5) before decreasing to a minimum value of 22.1 ± 5.3 Ma (step 14; Table 5). The discordant age spectra of samples ARESCI and DES are consistent with the presence of mixed mica populations as observed in thin section (see section 5.1), although the possible presence of extraneous argon cannot be totally discounted.

[39] Two age spectra were obtained for separate fragments of sample BEIG (Figures 9c and 9d). Both spectra are characterized by similar, broadly saddle-shaped profiles, with most apparent ages being younger than those from samples ARESCI and DES (Table 5). In the case of aliquot BEIG-A, apparent ages decrease from a maximum value of 55.2 ± 7.6 Ma to a minimum value of 34.6 ± 0.2 Ma. For aliquot BEIG-B, apparent ages decrease from a maximum value of 39.9 ± 0.4 Ma to a minimum of 34.2 ± 0.3 Ma. The discordance of the two age spectra again suggests presence of multiple mica populations and/or the presence of extraneous argon. The minimum apparent ages (steps 8–9 for both spectra), which average 34.7 ± 0.3 Ma and 34.3 ± 0.4 Ma, respectively (Table 5), are considered to represent maximum estimates for the time of Alpine mica crystallization.

8. AFT Thermochronology

[40] Apatite fission track analytical procedures are reported in section A2. Four samples were selected for analysis and the results are listed in Table 6 and illustrated in Figure 10. The metasedimentary samples of the Voltri-Rossiglione Unit (FAB, FADO and MAS) produced ages between 9.3 ± 2.6 and 23.9 ± 4.9 Ma. Samples FADO and MAS have identical ages of ~23 Ma, within the analytical uncertainties. The mean track lengths of the two samples are 14.5 ± 0.6 and 14.2 ± 7 μm, with 1σ standard deviations of 1.7 and 1.0 μm, respectively. The high χ^2 values for these samples demonstrate that all grains within each sample belong to one homogeneous age population. Consequently the mean track lengths of > 14 μm indicate that the two samples cooled rapidly from temperatures above 110°C to below 60°C. Although the low number of track lengths measured does not permit thermal history modeling, the adoption of a simplified closure temperature model applicable to rapidly cooled apatites [cf. *Wagner and Van den Haute*, 1992] suggests that cooling occurred at ~23 Ma. The topographically lowermost sample (FAB) has a younger average AFT age of 9.3 ± 2.6 Ma, composed by a broad spectrum of single grain ages. The low χ^2 probability of 29% and an age dispersion of 11% indicate slower cooling of this sample or a later reheating event to temperatures above 60°C. The eclogite sample VOL from the Beigua Unit yielded the youngest average AFT age of 2.5 ± 0.6 Ma, with individual ages all younger than 10 Ma. A χ^2 probability of 87% (statistically more relevant for low track densities) and an age dispersion of 0% indicate cooling from > 110°C to surface temperatures since the Late Pliocene.

9. Discussion

[41] The new petrological data presented above document the exhumation history of the Voltri-Rossiglione Unit, initially characterized by a nearly isothermal retrogressive P-T path to ~8 kbar and 500°C, followed by a cooling trajectory to lower greenschist facies conditions at ~3.5 kbar and 350°C (Figure 11). The interpretation of the P-T results in terms of an exhumation path is supported by both chemical (zoning of chloritoid and phengite grains) and textural (overgrowth of the main composite D_2 fabric on the pristine phg_1-cld_1 assemblages) relationships. Despite uncertainties in thermobarometric estimates, the cooler T estimates (~ 50°C) systematically obtained for sample 8D can be reconciled with the proximity of the selected sample to the mylonitic shear zone marking the boundary between the Beigua serpentinites and the Voltri-Rossiglione metasediments (Figures 2 and 3), where refrigeration by fluid circulation may acted [e.g., *Morrison and Anderson*, 1998; *Trotet et al.*, 2001].

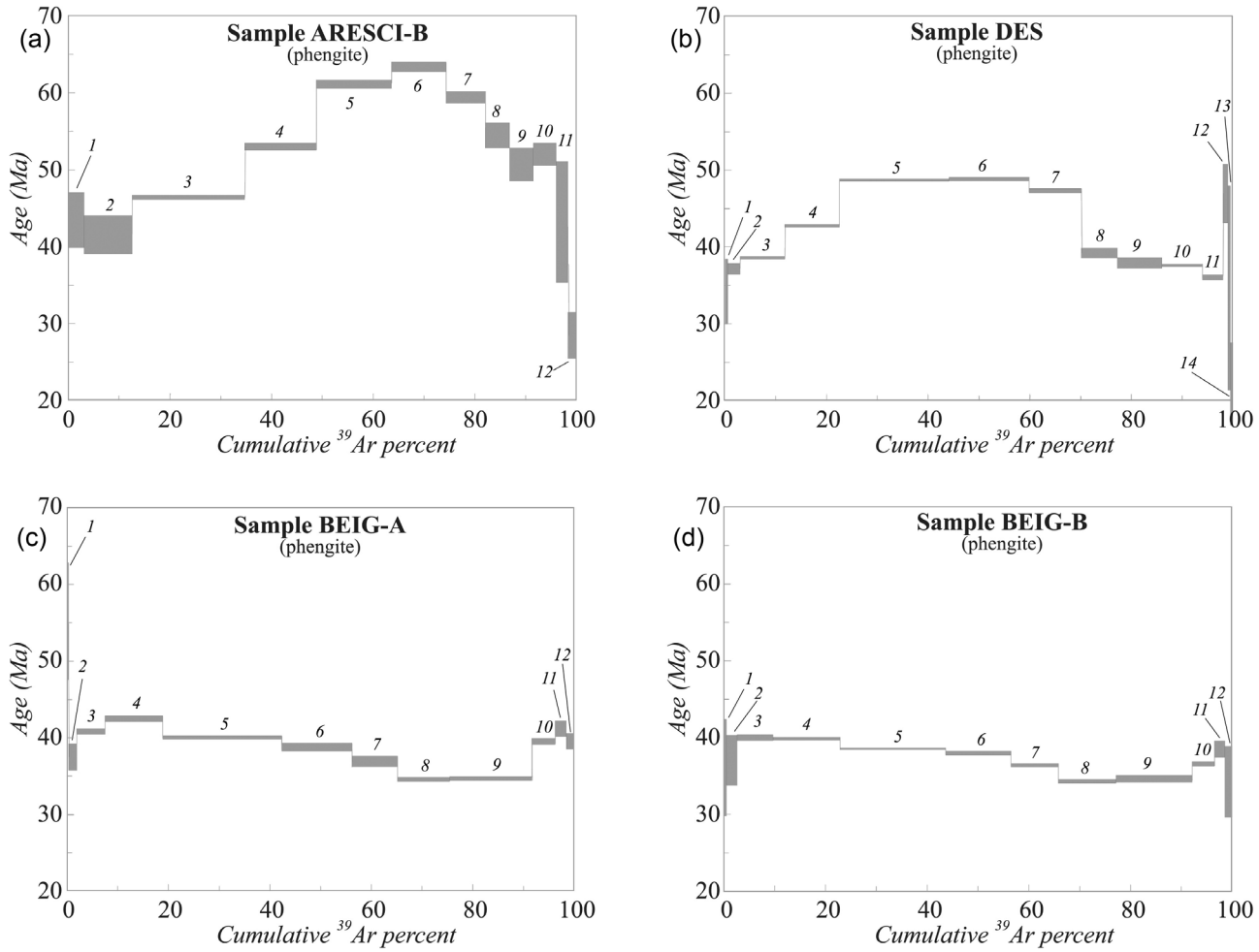

Figure 9. (a–d) The ^{40}Ar-^{39}Ar age spectra for phengite separates from selected metasedimentary samples (box heights represent ± 1σ uncertainties).

[42] The present work shows that the metasedimentary rock units underwent similar (slightly lower) P-T peak metamorphic conditions to those determined for eclogitic bodies within the Beigua Unit [e.g., *Messiga et al.*, 1983; *Liou et al.*, 1998; *Brouwer et al.*, 2002; *Vignaroli et al.*, 2005]. Moreover, in comparison to the retrogressive P-T path reconstructed for the eclogites [e.g., *Messiga and Scambelluri*, 1991; *Vignaroli et al.*, 2005], there is concordance both in terms of relative P-T conditions and P/T gradients (Figure 11).

9.1. Age Data Interpretation

9.1.1. Jurassic SHRIMP Ages

[43] For eclogite sample VOL, an age of 151 ± 11 Ma was obtained for zircons with preserved oscillatory and sector zoning, and moderate Th/U. These features are indicative of an igneous origin for these zircons [cf. *Vavra et al.*, 1999; *Hoskin and Schaltegger*, 2003]. Consequently, we interpret the 151 ± 11 Ma age as dating the gabbroic protolith of the eclogite. The scattered ages of the unzoned domains are most likely due to Pb loss during Alpine metamorphism. The Jurassic age for the protolith is in agreement with other protolith ages of 160 ± 1 Ma and 161 ± 3 Ma reported by *Rubatto and Scambelluri* [2003] for a metagabbro and a metarodingite from the Beigua Unit. Middle to Late Jurassic gabbroic intrusions are widespread across the Western Alps [e.g., *Rubatto et al.*, 1998; *Bucher et al.*, 2005] and are considered to be related to opening of the Liguro-Piedmont oceanic domain.

[44] Zircons of similar Jurassic age (153 ± 4 Ma) were found in the metasedimentary BEIG sample. These zircons display the same magmatic zoning as those from the eclogite sample. Furthermore, zircons from the metasediments have a HREE-enriched trace element pattern, with a marked negative Eu anomaly, indicative of formation in equilibrium with a plagioclase-bearing igneous rock [e.g., *Hoskin and Schaltegger*, 2003]. From these data we conclude that the metasediments were deposited in a marine setting from detritus that consisted mainly of locally sourced gabbroic rocks. A similar conclusion was reached for qtz-rich metasediments in another slice of the Liguro-Piedmont oceanic domain (the Zermatt ophiolites), which also contains Jurassic magmatic zircons [*Rubatto et al.*, 1998]. The presence of

Table 5. The $^{40}Ar/^{39}Ar$ Furnace Step Heating Analytical Results

Temp (°C)	Cum. % ^{39}Ar	^{40}Ar (x10^{-13} moles)	^{39}Ar (x10^{-14} moles)	^{38}Ar (x10^{-16} moles)	^{37}Ar (x10^{-16} moles)	^{36}Ar (x10^{-16} moles)	Ca/K	% $^{40}Ar^*$	$^{40}Ar^*/^{39}Ar$	Age (Ma)
					Sample ARESCI-B (J Value = 0.004746 ± 0.000013)					
700	3.03	0.6229 ± 0.0013	0.2161 ± 0.0004	0.2828 ± 0.0197	0.5494 ± 0.5494	1.7330 ± 0.0314	0.044 ± 0.044	17.8	5.127 ± 0.434	43.37 ± 3.62
800	12.47	0.5562 ± 0.0011	0.6724 ± 0.0010	0.0295 ± 0.0830	0.5498 ± 0.5498	0.7688 ± 0.0675	0.014 ± 0.014	59.2	4.894 ± 0.297	41.42 ± 2.49
900	34.72	1.2012 ± 0.0027	1.5853 ± 0.0025	0.1455 ± 0.1281	0.5501 ± 0.5501	1.1249 ± 0.0171	0.006 ± 0.006	72.3	5.480 ± 0.037	46.32 ± 0.31
930	48.78	0.7814 ± 0.0017	1.0013 ± 0.0018	0.0079 ± 0.0900	0.5503 ± 0.5503	0.5176 ± 0.0190	0.010 ± 0.010	80.4	6.277 ± 0.060	52.96 ± 0.50
960	63.58	0.8899 ± 0.0019	1.0544 ± 0.0012	0.0111 ± 0.0975	0.5506 ± 0.5506	0.4211 ± 0.0231	0.009 ± 0.009	86.0	7.260 ± 0.068	61.11 ± 0.56
990	74.42	0.6613 ± 0.0016	0.7724 ± 0.0011	0.0178 ± 0.0740	0.5509 ± 0.5509	0.2684 ± 0.0194	0.012 ± 0.012	88.0	7.534 ± 0.078	63.38 ± 0.64
1020	82.01	0.4391 ± 0.0009	0.5408 ± 0.0007	0.0330 ± 0.0525	0.5512 ± 0.5512	0.1952 ± 0.0168	0.018 ± 0.018	86.9	7.052 ± 0.094	59.39 ± 0.77
1050	86.92	0.2597 ± 0.0006	0.3499 ± 0.0004	0.0004 ± 0.0542	0.5515 ± 0.5515	0.1144 ± 0.0232	0.028 ± 0.028	87.0	6.455 ± 0.197	54.43 ± 1.64
1100	91.67	0.2530 ± 0.0005	0.3387 ± 0.0004	0.0004 ± 0.0357	0.5518 ± 0.5518	0.1687 ± 0.0294	0.029 ± 0.029	80.3	5.998 ± 0.257	50.64 ± 2.14
1150	96.12	0.2440 ± 0.0006	0.3168 ± 0.0005	0.0004 ± 0.0277	0.5521 ± 0.5521	0.1658 ± 0.0190	0.031 ± 0.031	79.9	6.157 ± 0.178	51.96 ± 1.48
1200	98.45	0.1309 ± 0.0003	0.1663 ± 0.0004	0.0599 ± 0.0332	0.5524 ± 0.5524	0.1563 ± 0.0534	0.058 ± 0.058	64.7	5.096 ± 0.949	43.12 ± 7.94
1450	100.00	0.1363 ± 0.0008	0.1101 ± 0.0020	0.1194 ± 0.0289	0.5527 ± 0.5527	0.3372 ± 0.0128	0.088 ± 0.088	26.9	3.327 ± 0.358	28.26 ± 3.02
					Sample DES (J Value = 0.004749 ± 0.000014)					
700	0.55	0.2078 ± 0.0006	0.1030 ± 0.0004	0.1082 ± 0.0195	0.5383 ± 0.5383	0.5635 ± 0.0175	0.091 ± 0.091	19.9	4.012 ± 0.505	34.05 ± 4.24
800	2.96	0.3166 ± 0.0007	0.4522 ± 0.0007	0.0175 ± 0.0383	0.5385 ± 0.5385	0.4030 ± 0.0130	0.021 ± 0.021	62.4	4.368 ± 0.087	37.04 ± 0.73
900	11.73	0.9224 ± 0.0019	1.6448 ± 0.0008	0.0111 ± 0.1353	5.3883 ± 5.3883	0.5966 ± 0.0091	0.057 ± 0.057	80.9	4.536 ± 0.020	38.45 ± 0.17
930	22.50	1.1906 ± 0.0024	2.0182 ± 0.0029	0.0004 ± 0.1629	5.3912 ± 5.3913	0.5888 ± 0.0131	0.047 ± 0.047	85.4	5.037 ± 0.024	42.65 ± 0.20
960	44.10	2.5694 ± 0.0052	4.0506 ± 0.0013	0.0281 ± 0.3288	5.3941 ± 5.3942	0.8117 ± 0.0147	0.023 ± 0.023	90.7	5.751 ± 0.017	48.61 ± 0.14
990	59.91	1.8745 ± 0.0038	2.9633 ± 0.0024	0.0004 ± 0.2419	5.3970 ± 5.3971	0.5594 ± 0.0219	0.032 ± 0.032	91.2	5.768 ± 0.026	48.75 ± 0.21
1020	70.25	1.1802 ± 0.0024	1.9385 ± 0.0023	0.0004 ± 0.1569	5.3999 ± 5.3999	0.3298 ± 0.0197	0.049 ± 0.049	91.7	5.586 ± 0.033	47.23 ± 0.28
1050	77.34	0.6756 ± 0.0015	1.3285 ± 0.0023	0.0004 ± 0.1123	5.4028 ± 5.4028	0.2123 ± 0.0343	0.071 ± 0.071	90.7	4.613 ± 0.078	39.10 ± 0.65
1100	86.08	0.7842 ± 0.0016	1.6401 ± 0.0008	0.0004 ± 0.1406	5.4058 ± 5.4058	0.1805 ± 0.0460	0.058 ± 0.058	93.2	4.456 ± 0.083	37.78 ± 0.70
1150	94.08	0.7057 ± 0.0014	1.5000 ± 0.0008	0.0004 ± 0.1253	5.4086 ± 5.4087	0.1451 ± 0.0099	0.063 ± 0.063	93.9	4.419 ± 0.022	37.47 ± 0.18
1200	98.14	0.3563 ± 0.0008	0.7609 ± 0.0005	0.0004 ± 0.0817	0.5412 ± 0.5412	0.1163 ± 0.0104	0.012 ± 0.012	90.3	4.230 ± 0.042	35.88 ± 0.35
1250	99.10	0.1025 ± 0.0002	0.1792 ± 0.0007	0.0004 ± 0.0258	0.5414 ± 0.5414	0.0108 ± 0.0280	0.053 ± 0.053	96.9	5.544 ± 0.463	46.88 ± 3.86
1350	99.51	0.0598 ± 0.0002	0.0778 ± 0.0003	0.0004 ± 0.0190	0.5417 ± 0.5417	0.0954 ± 0.0419	0.122 ± 0.122	52.9	4.067 ± 1.592	34.51 ± 13.38
1450	100.00	0.0867 ± 0.0004	0.0912 ± 0.0008	0.0454 ± 0.0216	0.5420 ± 0.5420	0.2135 ± 0.0191	0.104 ± 0.104	27.3	2.593 ± 0.621	22.08 ± 5.26
					Sample BEIG-A (J Value = 0.004741 ± 0.000016)					
700	0.32	0.4182 ± 0.0009	0.0638 ± 0.0006	0.2251 ± 0.0419	0.6300 ± 0.6300	1.2738 ± 0.0195	0.173 ± 0.173	10.0	6.554 ± 0.916	55.20 ± 7.60
800	1.85	0.3987 ± 0.0008	0.2998 ± 0.0007	0.1567 ± 0.0285	0.6304 ± 0.6304	0.8997 ± 0.0206	0.037 ± 0.037	33.3	4.432 ± 0.205	37.51 ± 1.71
900	7.49	0.8312 ± 0.0017	1.1097 ± 0.0023	0.1458 ± 0.0914	6.3071 ± 6.3072	0.9986 ± 0.0153	0.099 ± 0.099	64.5	4.832 ± 0.045	40.86 ± 0.37
930	18.90	1.3851 ± 0.0029	2.2426 ± 0.0022	0.1955 ± 0.1843	6.3106 ± 6.3106	0.8730 ± 0.0346	0.049 ± 0.049	81.4	5.026 ± 0.048	42.48 ± 0.40
960	42.39	2.4409 ± 0.0050	4.6189 ± 0.0035	0.0004 ± 0.3744	6.3139 ± 6.3140	0.8565 ± 0.0354	0.024 ± 0.024	89.6	4.737 ± 0.025	40.06 ± 0.21
990	56.33	1.4128 ± 0.0030	2.7409 ± 0.0030	0.0004 ± 0.2232	6.3173 ± 6.3174	0.5247 ± 0.0573	0.040 ± 0.040	89.0	4.589 ± 0.063	38.83 ± 0.53
1020	65.29	0.8723 ± 0.0018	1.7617 ± 0.0020	0.0004 ± 0.1458	6.3207 ± 6.3207	0.3500 ± 0.0489	0.063 ± 0.063	88.1	4.365 ± 0.083	36.95 ± 0.69
1050	75.66	0.9186 ± 0.0019	2.0385 ± 0.0012	0.0004 ± 0.1697	6.3242 ± 6.3242	0.2911 ± 0.0209	0.054 ± 0.054	90.6	4.084 ± 0.032	34.60 ± 0.27
1100	91.77	1.4081 ± 0.0029	3.1674 ± 0.0025	0.0004 ± 0.2589	6.3275 ± 6.3276	0.3720 ± 0.0314	0.035 ± 0.035	92.2	4.099 ± 0.031	34.72 ± 0.26
1150	96.39	0.4733 ± 0.0010	0.9084 ± 0.0015	0.0004 ± 0.0776	0.6331 ± 0.6331	0.1651 ± 0.0144	0.012 ± 0.012	89.7	4.673 ± 0.049	39.53 ± 0.41
1200	98.48	0.2125 ± 0.0005	0.4114 ± 0.0012	0.0004 ± 0.0372	0.6334 ± 0.6334	0.0409 ± 0.0170	0.027 ± 0.027	94.3	4.873 ± 0.124	41.21 ± 1.04
1450	100.00	0.1887 ± 0.0004	0.2980 ± 0.0013	0.0385 ± 0.0314	0.6338 ± 0.6338	0.1671 ± 0.0121	0.037 ± 0.037	73.8	4.675 ± 0.122	39.55 ± 1.02

Table 5. (continued)

Temp (°C)	Cum. % ^{39}Ar	^{40}Ar (x10^{-13} moles)	^{39}Ar (x10^{-14} moles)	^{38}Ar (x10^{-16} moles)	^{37}Ar (x10^{-16} moles)	^{36}Ar (x10^{-16} moles)	Ca/K	% ^{40}Ar*	^{40}Ar*/^{39}Ar	Age (Ma)
Sample BEIG-B (J Value = 0.004742 ± 0.000015)										
700	0.42	0.2841 ± 0.0006	0.0844 ± 0.0006	0.1276 ± 0.0174	0.6189 ± 0.6189	0.8400 ± 0.0214	0.128 ± 0.128	12.6	4.245 ± 0.753	35.95 ± 6.32
800	2.52	0.4033 ± 0.0010	0.4170 ± 0.0007	0.1148 ± 0.0395	0.6192 ± 0.6192	0.7496 ± 0.0551	0.026 ± 0.026	45.1	4.359 ± 0.391	36.91 ± 3.28
900	9.60	0.9816 ± 0.0020	1.4074 ± 0.0009	0.1110 ± 0.1154	6.1952 ± 6.1953	1.0769 ± 0.0212	0.077 ± 0.077	67.6	4.714 ± 0.047	39.88 ± 0.39
930	22.79	1.4678 ± 0.0030	2.6235 ± 0.0024	0.0004 ± 0.2150	6.1986 ± 6.1987	0.7973 ± 0.0171	0.041 ± 0.041	83.9	4.697 ± 0.023	39.74 ± 0.19
960	43.62	2.0948 ± 0.0043	4.1450 ± 0.0047	0.0004 ± 0.3362	6.2019 ± 6.2020	0.7204 ± 0.0145	0.026 ± 0.026	89.8	4.540 ± 0.016	38.42 ± 0.13
990	56.48	1.2713 ± 0.0026	2.5575 ± 0.0028	0.0004 ± 0.2082	6.2053 ± 6.2053	0.4339 ± 0.0274	0.042 ± 0.042	89.9	4.470 ± 0.034	37.83 ± 0.28
1020	65.91	0.8868 ± 0.0018	1.8744 ± 0.0022	0.0004 ± 0.1549	6.2086 ± 6.2086	0.2852 ± 0.0172	0.058 ± 0.058	90.5	4.281 ± 0.029	36.26 ± 0.24
1050	77.25	1.0059 ± 0.0020	2.2574 ± 0.0023	0.0004 ± 0.1827	6.2119 ± 6.2120	0.3253 ± 0.0247	0.048 ± 0.048	90.4	4.030 ± 0.034	34.15 ± 0.28
1100	92.18	1.3474 ± 0.0028	2.9686 ± 0.0027	0.0004 ± 0.2398	6.2153 ± 6.2154	0.4706 ± 0.0526	0.037 ± 0.037	89.7	4.070 ± 0.053	34.49 ± 0.45
1150	96.57	0.4456 ± 0.0012	0.8742 ± 0.0026	0.0128 ± 0.0729	6.2186 ± 6.2187	0.2341 ± 0.0086	0.124 ± 0.124	84.5	4.306 ± 0.035	36.46 ± 0.29
1200	98.72	0.2149 ± 0.0005	0.4264 ± 0.0005	0.0004 ± 0.0384	0.6222 ± 0.6222	0.0733 ± 0.0188	0.026 ± 0.026	89.9	4.532 ± 0.131	38.36 ± 1.10
1450	100.00	0.1757 ± 0.0013	0.2550 ± 0.0012	0.0004 ± 0.0387	0.6225 ± 0.6225	0.2472 ± 0.0475	0.043 ± 0.043	58.4	4.026 ± 0.553	34.12 ± 4.64

Jurassic detrital zircons in the metasediment implies that this sediment was deposited in the Mesozoic, after ~160 Ma and before onset of the Alpine orogeny. It follows that all the structures and metamorphism observed in the Voltri-Rossiglione metasediments are Alpine in origin.

9.1.2. Alpine SHRIMP Ages

[45] U-Pb SHRIMP dating yielded Alpine Eocene-Oligocene ages for zircon rims (33.8 ± 0.8 Ma) and titanite (29 ± 5 Ma) from the metasedimentary sample BEIG. The textural and geochemical signatures of the zircon rims (crosscutting of magmatic zoning, low Th/U, low trace element content) indicate a metamorphic origin [e.g., *Hoskin and Schaltegger*, 2003]. In particular, the trace element pattern of the zircon rims is similar to metamorphic zircons investigated by *Spandler et al.* [2004] formed during peak metamorphism (400°C–600°C and 12–18 kbar) in the absence of garnet. The low Ti content of the BEIG zircon rims is in line with growth at $T \leq 650$°C [*Watson et al.*, 2006]. Petrological evidence shows that the Voltri-Rossiglione Unit, during its metamorphic evolution (from burial to exhumation), never experienced temperatures in excess of ~550°C [*Cimmino and Messiga*, 1979; *Hoogerduijn Strating*, 1991; *Federico et al.*, 2007a] (see also this study). The euhedral shape and the sharp boundaries with the magmatic zircon core suggest that the rims represent new growth and not recrystallized domains. It is thus important to note that zircon growth must have occurred under low-grade metamorphic conditions with temperatures below ~550°C. At these low temperatures, new zircon growth is unusual, and has only rarely been documented in metamorphic veins [*Rubatto et al.*, 1999; *Liati and Gebauer*, 1999] and more recently in prehnite-pumpellyite rocks where temperatures were on the order of ~250°C [*Rasmussen*, 2005]. Given the low-grade conditions, fluid circulation is likely to have favored zircon growth during rock exhumation [*Geisler et al.*, 2007]. The presence of zircon rims with abundant initial Pb, as a mixture of common and radiogenic components, is consistent with growth in a fluid-dominated environment. Pb strongly partitions into fluids and initial radiogenic Pb from another source could have been contained in the fluid. The presence of a negative Eu anomaly in zircon from the BEIG metasediment suggests that the zircon rims formed in equilibrium with retrograde albite, rather than at the HP peak metamorphism [*Rubatto*, 2002]. Therefore, we propose that the metamorphic rims of metasedimentary zircons reflect a fluid enhanced tectonic process during the exhumation of the unit.

[46] Within analytical uncertainty, the Alpine U-Pb age obtained from titanite (29 ± 5 Ma) overlaps those of the zircon rims. Key textural observations described above, such as the occurrence of phg_1 as inclusions in titanite (Figure 5i) and the continuity of S_2 foliations in titanite porphyroblasts (Figures 5j and 5k), suggest that titanite growth was pretectonic to syntectonic with respect to S_2 development and, hence, greenschist retrogressive metamorphism. Therefore, the zircon rim and titanite ages are interpreted to represent the time of the D_2 fabric development in the metapelites, which is related to greenschist facies exhumation of the Voltri-Rossiglione Unit.

Table 6. Apatite Fission Track Data From the Voltri Massif[a]

Sample	Tectonic Unit	Lat., Long.	Elev. (m)	ρ_D[b] (10^6 cm^{-2})	ρ_S[c] (10^6 cm^{-2})	ρ_I[d] (10^6 cm^{-2})	P(χ^2)[e] (%)	AFT Age[f] (Ma)	MTL[g] (μm)	SD (μm)
FADO	VRU (ms)	44°28′58″N, 8°44′01″E	473	1.261 (9520)	0.011 (27)	0.106 (250)	95 (0)	23.9 ± 4.9 (29)	14.46 ± 0.65 (7)	1.71
MAS	VRU (ms)	44°30′10″N, 8°42′18″E	413	1.261 (9520)	0.012 (21)	0.116 (203)	100 (0)	22.9 ± 5.3 (30)	14.22 ± 0.71 (2)	1.00
FAB	VRU (ms)	44°26′07″N, 8°44′20″E	97	1.261 (9520)	0.029 (14)	0.705 (338)	29 (0.11)	9.3 ± 2.6 (16)	–	–
VOL	BU (e)	44°26′20″N, 8°33′18″E	783	1.261 (9520)	0.016 (17)	1.395 (1521)	87 (0)	2.5 ± 0.6 (19)	–	–

[a]VRU, Voltri-Rossiglione Unit (ms, metasedimentary rock); BU, Beigua Unit (e, eclogite); Lat., latitude; Long., longitude; Elev., elevation; ρ_D, ρ_S, and ρ_I, density of counted dosimeter, spontaneous, and induced tracks, respectively; P(χ^2), χ^2 probability; AFT age, apatite fission track (central) age; MTL, mean track length; SD, standard deviation.
[b]Values in parentheses are number of counted dosimeter tracks.
[c]Values in parentheses are number of counted spontaneous tracks.
[d]Values in parentheses are number of counted induced tracks.
[e]Values in parentheses are correlation coefficients.
[f]Values in parentheses are number of counted grains.
[g]Values in parentheses are number of measured tracks.

9.1.3. The ^{40}Ar-^{39}Ar Ages

[47] The ^{40}Ar-^{39}Ar analyses produced a large range of apparent ages, from ~64 Ma (sample ARESCI) to ~34 Ma (excluding the 1450°C steps of samples ARESCI and DES; Table 5). Similar variations in apparent ages have been previously reported from Alpine rocks and several explanations can be considered, including (1) the presence of multiple generations of phengite in polyphase metamorphic fabrics [e.g., *Agard et al.*, 2002], (2) the possible effects of argon loss or extraneous (excess ± inherited) argon [e.g., *Scaillet et al.*, 1992; *Kelley*, 2002], (3) recoil loss/redistribution of ^{39}Ar [e.g., *Di Vincenzo et al.*, 2006], and (4) the attribution of samples to different tectonic units within the Voltri Massif. The latter factor seems to be unrealistic given the similarities between samples in terms of rock type, structure, texture and petrology. Recoil loss/redistribution of ^{39}Ar is also not considered to be a factor here, as phengite grains are relatively coarse (>100 μm) and few grains exhibit evidence of alteration (e.g., chloritization) that could reduce effective grain dimensions. The presence of variable quantities of extraneous argon (either argon inherited from an older protolith or as excess argon introduced during retrogression) has been documented in polymetamorphic basement rocks in the Western Alps and is attributed to low fluid fluxes, resulting in limited grain recrystallization, penetrative deformation, fluid contamination, and compositional exchanges [e.g., *Di Vincenzo et al.*, 2006, and references therein]. In the Voltri Massif, pre-Alpine mica appears to be very rare or absent from the metasediments. Moreover, the occurrence of a multiple array of synmetamorphic veins [*Crispini and Frezzotti*, 1998; *Vignaroli et al.*, 2009a] suggests large-scale fluid mobility during progressive ductile-to-brittle deformation; thus arguing against excess argon retention within the Alpine micas. Therefore, we suggest that the range in apparent ages is more likely due to the presence of different phengite populations formed by the M_1, M_2, and M_3 metamorphic stages. Samples hosting better preserved and larger proportions of M_1 phengite (ARESCI and DES), give older ages and more disturbed age spectra than the sample in which the M_2 fabric is dominant (BEIG). We also suggest that the variation in the ^{40}Ar/^{39}Ar spectra reflect progressive chemical equilibration of phengite during progressive exhumation [e.g., *Lips et al.*, 1998; *Brunet et al.*, 2000]. If correct, the maximum ^{40}Ar/^{39}Ar ages should represent minimum estimates for the formation of the oldest micas (phg_1) and the minimum ages should reflect maximum estimates for crystallization of the youngest micas (phg_{2-3}). In this context, the ~60 Ma ages in sample ARESCI and the ~50 Ma ages in sample DES should be considered as minimum ages for peak metamorphism, in accord with temporal constraints on similar metasedimentary units in the Western Alps [*Agard et al.*, 2002]. Within this age range, the main ^{40}Ar/^{39}Ar age population detected in the detrital sediments of the TPB is ~45 Ma [*Barbieri et al.*, 2003] and an age interval of 43–40 Ma has been proposed for HP metamorphism recorded in mafic eclogitic and blueschist facies blocks enclosed in metasedimentary units of the Voltri Massif [*Federico et al.*, 2007b]. Furthermore, the 45–36 Ma postpeak metamorphic cooling ages obtained by *Schamel* [1974] and *Hoogerduijn Strating* [1991] can be reconciled

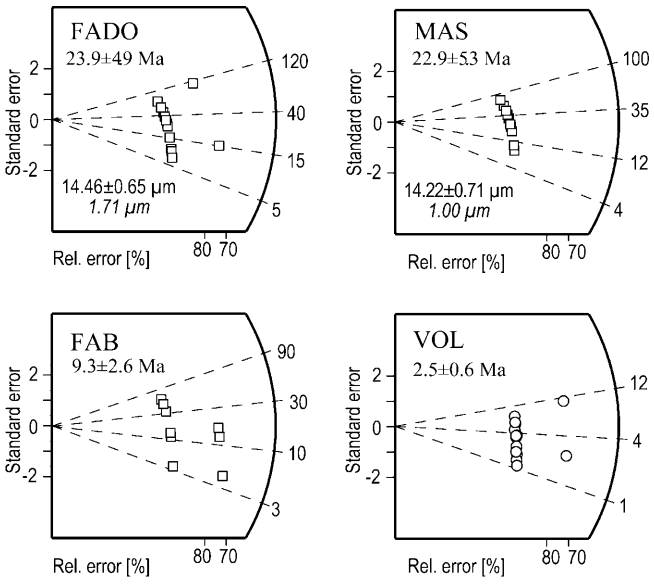

Figure 10. Radial plots showing apatite fission track ages for the Voltri-Rossiglione Unit (FAB, FADO, MAS) and Beigua Unit (VOL).

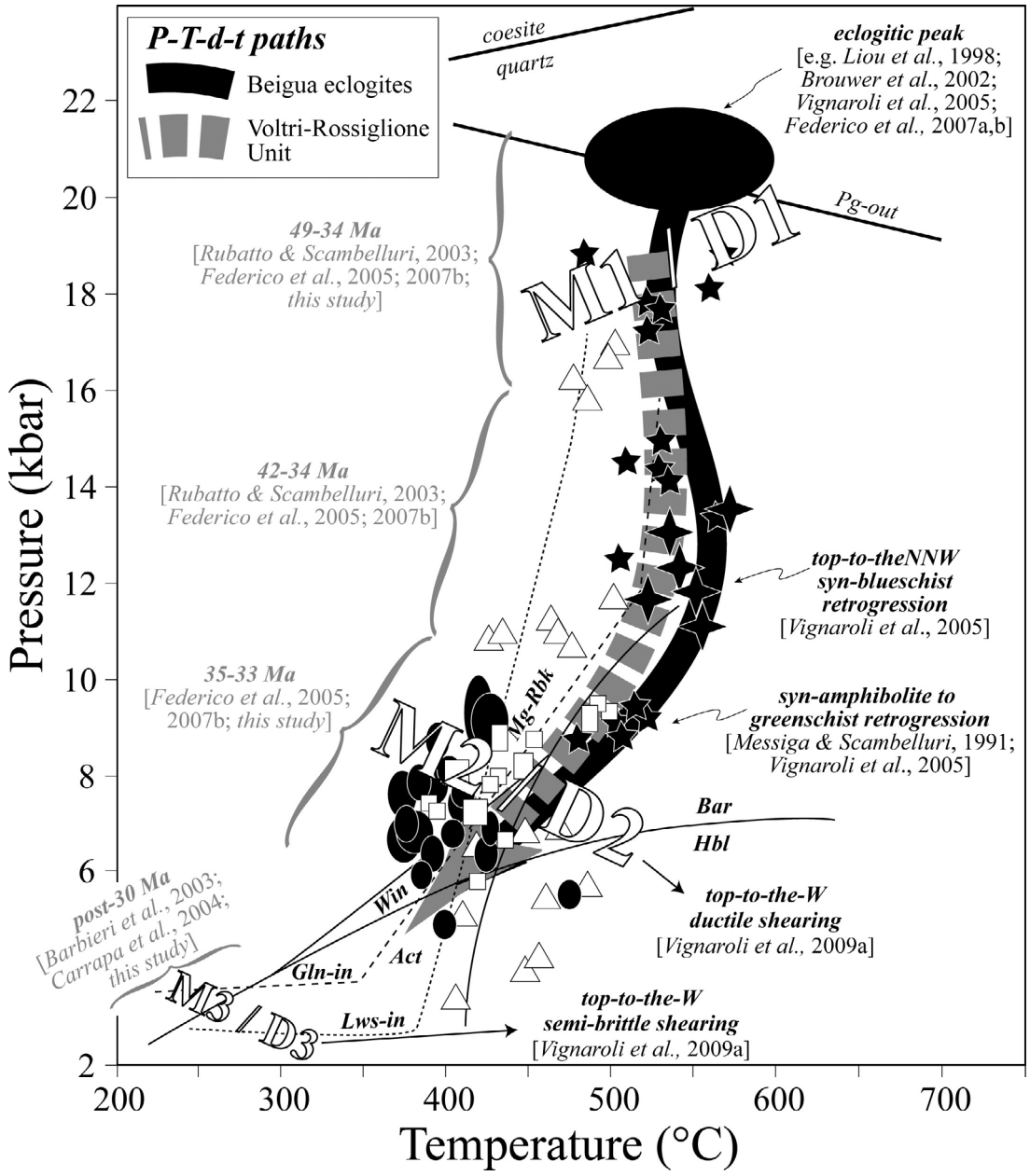

Figure 11. Reconstructed P-T-d-t paths for both the Voltri-Rossiglione and Beigua units, obtained by integrating published geological data sets (for kinematics, thermobarometry, and radiometric ages) with results from this study. Breakdown of paragonite (pg-out) and the stability fields of lawsonite (lws-in) and glaucophane (gln-in) are after *Parra et al.* [2002]. P-T stability fields for amphibole after *Otsuki and Banno* [1990].

with the 43–40 Ma interval attributed to the blueschist metamorphism in the Voltri Massif [*Federico et al.*, 2005, 2007b].

[48] The ^{40}Ar-^{39}Ar age spectra obtained from the syn-greenschist mylonitic samples BEIG-A and BEIG-B are less discordant, with apparent ages confined between 34 and 40 Ma. The minimum apparent ages of ~34 Ma are consistent with the ~33 Ma ages obtained by *Federico et al.* [2005] for the greenschist facies metamorphic stage of the Voltri mica schists.

[49] Despite some uncertainties, the above discussion allows to bracket the HP stage in the Voltri area between two end-members: the ~50 Ma (or older) ages from detrital white micas hosted in metamorphic clasts from the TPB [*Federico et al.*, 2005], and the 33.6 ± 1.0 Ma age proposed by *Rubatto and Scambelluri* [2003] for eclogitic metamorphism of the Beigua Unit. As already discussed by *Federico et al.* [2005], this discrepancy may be reconciled by considering that the eclogite bodies likely formed a distinctive tectonic unit within the Voltri Massif and underwent HP

metamorphism when the metasedimentary cover was equilibrating at greenschist facies conditions, with subsequent, ultrafast exhumation. Further detailed geological constraints are nevertheless needed to better assess this crucial scenario.

9.1.4. AFT Data

[50] The AFT ages (between 2.5 ± 0.6 and 23.9 ± 4.9 Ma) and the track length data from the Voltri samples are within error of existing data from the adjacent Briançonnais domain [*Barbieri et al.*, 2003]. The AFTA ages are younger than the protolith ages of the samples and the U-Pb ages reported here and elsewhere, and are consistent with the regional AFT age distribution of the Western Alps [*Hurford et al.*, 1991; *Seward and Mancktelow*, 1994; *Fügenschuh et al.*, 1997; *Fügenschuh and Schmid*, 2003; *Malusà et al.*, 2005; *Malusà and Vezzoli*, 2006]. In particular, the AFT ages from the samples FADO and MAS (Table 6) indicate that some parts of the Voltri-Rossiglione Unit were already cooled/exhumed by the Late Oligocene-Early Miocene.

[51] The AFT ages from the Voltri-Rossiglione Unit correlate with current topographic altitudes. However, this trend contrasts with the young age of the Beigua sample, which was collected from the highest altitude. This AFT age conundrum suggests substantial postorogenic faulting and/or differential erosion of kilometer scale between the Beigua and Voltri-Rossiglione units. Above all, the AFT data suggest possible resetting of the AFT system by postdepositional thermal overprinting as a result of burial following subsidence in the TPB since the Oligocene-Late Miocene and final Pliocene-Quaternary uplift [see also *Barbieri et al.*, 2003; *Bertotti et al.*, 2006]. Alternatively, final exhumation may have commenced slowly already in the late Miocene, and substantially increased during the last 3 Ma as reported from the northern Apennines [e.g., *Ventura et al.*, 2001]. In any case, the limited number of samples and track lengths measured and the unknown composition of the analyzed apatite crystals, do not allow further quantification. To resolve this problem, a more detailed thermochronological study including both fission track and (U-Th-Sm)/He analysis on apatites would be recommended.

9.2. A Refined P-T-d-t Path for the Voltri Massif HP Complex

[52] Based on the above data, combined with published geological information (in terms of P-T paths, deformation fabric and geochronology), we suggest a unique P-T-d-t path for the tectonic evolution of the Voltri Massif, as follows (Figure 11).

[53] 1. D_1-M_1 stage corresponds to peak metamorphism under blueschist to eclogitic facies conditions [e.g., *Liou et al.*, 1998; *Brouwer et al.*, 2002; *Vignaroli et al.*, 2005; *Federico et al.*, 2007a, 2007b], which is assigned to the time interval between ~34 and ~50 Ma [see also *Rubatto and Scambelluri*, 2003; *Federico et al.*, 2005, 2007b]. The D_1 fabric has been extensively overprinted and no structural/kinematics data could be obtained. However, kinematic data are available for the blueschist facies retrogressive stage recorded in the eclogites, where a major top-to-the-north shearing event is documented [*Vignaroli et al.*, 2005].

[54] 2. D_2-M_2 stage corresponds to the main retrogressive event and is represented by syngreenschist *S-L* fabric development in the Voltri-Rossiglione metasediments [e.g., *Cimmino and Messiga*, 1979; *Hoogerduijn Strating*, 1991; *Messiga and Scambelluri*, 1991; *Hoogerduijn Strating*, 1994; *Hermann et al.*, 2000; *Vissers et al.*, 2001; *Capponi and Crispini*, 2002; *Federico et al.*, 2007a; *Vignaroli et al.*, 2009a]. This stage is assigned to the 33–35 Ma time interval [see also *Federico et al.*, 2005, 2007b] and is characterized by top-to-the-west/NW noncoaxial shearing [e.g., *Hoogerduijn Strating*, 1994; *Hermann et al.*, 2000; *Vissers et al.*, 2001; *Capponi and Crispini*, 2002; *Federico et al.*, 2007a; *Vignaroli et al.*, 2009a].

[55] 3. D_3-M_3 stage represents continuous exhumation into the brittle-dominated deformation regime [see also *Hoogerduijn Strating*, 1994; *Capponi and Crispini*, 2002; *Vignaroli et al.*, 2009a]. This stage is considered to have taken place post ~30 Ma, an event that overlaps with the onset of TPB deposition [*Charrier et al.*, 1964; *Gelati et al.*, 1993; *Gelati and Gnaccolini*, 1998] and its polyphase denudation/subsidence [*Barbieri et al.*, 2003; *Carrapa et al.*, 2004; *Federico et al.*, 2005; *Bertotti et al.*, 2006].

[56] The exhumation trajectory is documented in the T-t diagram presented in Figure 12, where we integrate data from both the Voltri units and the metamorphic clasts of the TPB. The exhumation rates were calculated by considering the mean ages of individual tectonometamorphic stages (peak HP, greenschist, and postgreenschist) and the age constraints discussed above (Figure 2b). Following *Bertotti et al.* [2006] a constant geothermal gradient of 25°C km^{-1} was assumed for the postgreenschist facies evolution, and an average lithostatic gradient of 30 MPa km^{-1} [e.g., *Spear*, 1993] was utilized. Figure 12 shows that the majority of the metamorphic samples is compatible with having followed a common two-step T-t path involving slow cooling (10°C–15°C Ma^{-1}) from the D_1-M_1 (~50 Ma) to the D_2-M_2 stage, followed by an increased cooling rate (32°C to 40°C Ma^{-1}) down to the apatite partial annealing zone (APAZ). These cooling rates can be converted into exhumation velocities of ~0.7–1.0 mm yr^{-1} for the HP greenschist step, and ~1–2 mm yr^{-1} for the greenschist-APAZ step. These data are compatible with previously proposed low (0.6–1.5 mm yr^{-1} [*Hoogerduijn Strating*, 1991]) to moderate (3.3–3.9 mm yr^{-1} [*Federico et al.*, 2005]) exhumation rates. A higher exhumation rate (18 mm yr^{-1}) is obtained when considering a ~34 Ma age for eclogite peak metamorphism in the Beigua Unit as proposed by *Rubatto and Scambelluri* [2003]. This again argues for an "exotic" origin for the eclogitic unit studied by *Rubatto and Scambelluri* [2003] and for a different P-T history of burial, exhumation and assembly within the Voltri realm.

[57] Our rates are an order of magnitude higher than velocities attributed to Eocene-Oligocene erosion in the Alpine area [e.g., *Schlunegger and Willett*, 1999] and are more in line with velocities ascribed to tectonic-assisted exhumation within the orogenic wedge [e.g., *Agard et al.*, 2002; *Fügenschuh et al.*, 1997; *Malusà and Vezzoli*, 2006]. This confirms that tectonics was the dominant mechanism responsible for exhumation of HP rocks in the Voltri Massif area, in agreement with what already documented for other

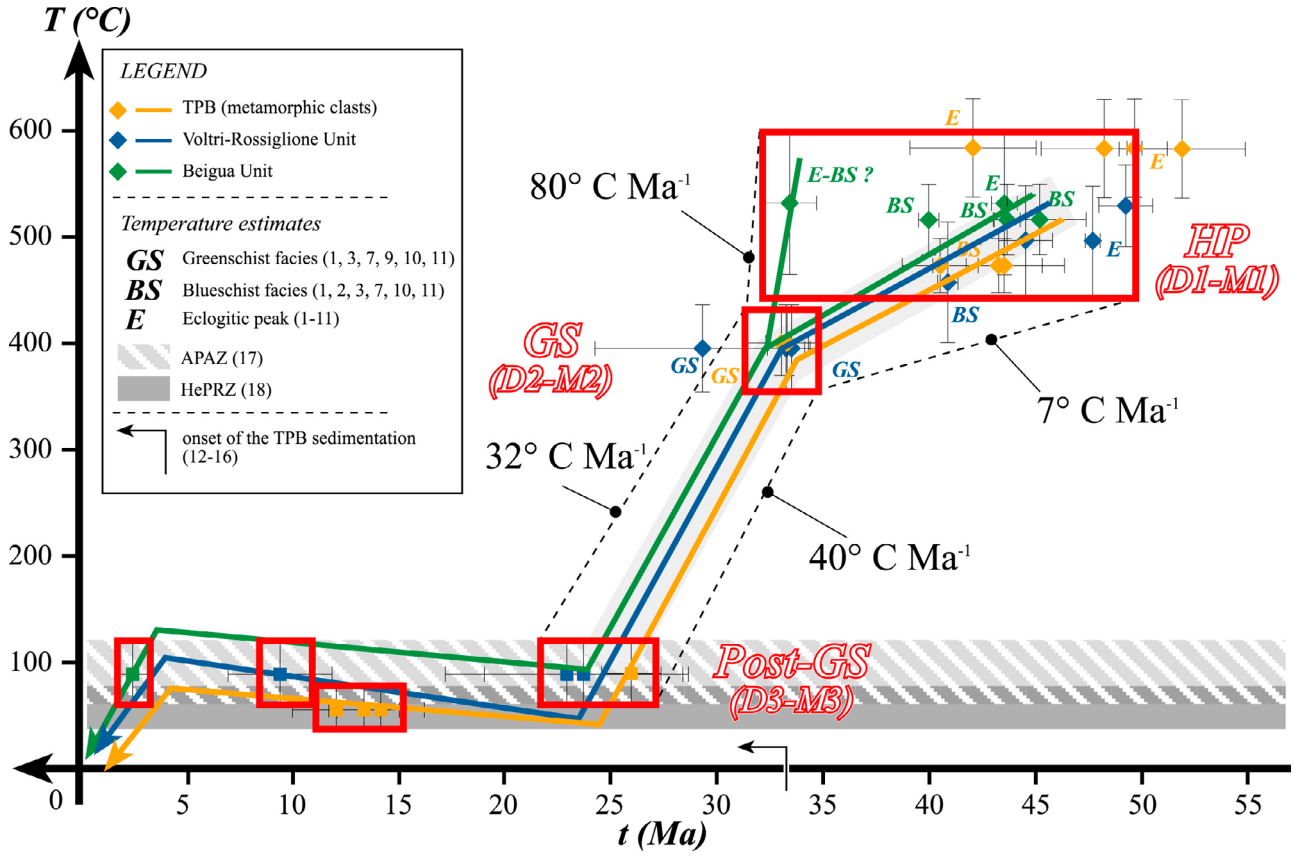

Figure 12. Cooling paths for the Voltri-Rossiglione Unit, the Beigua Unit, and metamorphic clasts from the Tertiary Piedmont Basin. All samples show similar return paths characterized by nonuniform exhumation rates. References are as follows: 1, *Federico et al.* [2007a]; 2, *Federico et al.* [2007b]; 3, *Vignaroli et al.* [2005]; 4, *Brouwer et al.* [2002]; 5, *Liou et al.* [1998]; 6, *Federico et al.* [2004]; 7, *Messiga and Scambelluri* [1991]; 8, *Messiga et al.* [1989]; 9, *Cimmino and Messiga* [1979]; 10, *Hoogerduijn Strating* [1991]; 11, this work; 12, *Charrier et al.* [1964]; 13, *Franceschetti* [1967]; 14, *Gelati et al.* [1993]; 15, *Gelati and Gnaccolini* [1998]; 16, *Di Biase and Pandolfi* [1999]; 17, *Green et al.* [1989]; 18, *Wolf et al.* [1998].

(U)HP units of the Alps [e.g., *Rubatto and Hermann*, 2001]. An exhumation scenario controlled by coupled, steady state, compression-erosion mechanism thus appears to be inadequate to reconcile the complete exhumation of the Voltri Massif HP complex. In particular, our T-t diagram implies for an exhumation process that was variable through time, with a sudden change in the cooling rate at the D_2-M_2 stage (Figure 12). In the field, this change can be linked to the pervasive development of the D_2 syngreenschist retrogressive fabric in the Lower Tectonic Complex, which corresponds to the major metamorphic/structural break within the tectonic edifice.

9.3. Proposal for an Exhumation Scenario

[58] We propose a two-stage process exhumation scenario (Figure 2f) for the Voltri Massif HP complex framed within the Tertiary tectonic convergence between the Eurasian and Adriatic plates, after closure of the interposed Liguro-Piedmont oceanic domain followed by Neogene back-arc extension [e.g., *Alvarez et al.*, 1974; *Dewey et al.*, 1989; *Jolivet et al.*, 2003]. This scenario includes (1) an early synorogenic stage (i.e., within the growing orogenic wedge) to enable exhumation from eclogitic and blueschist facies conditions and (2) a subsequent, postorogenic stage, responsible for cooling and exhumation from greenschist facies conditions to upper crustal levels. The synorogenic exhumation stage is related to the dynamic evolution of the subduction zone developed along the Alpine-Apennine convergence zone. In the Middle Eocene, strike-slip motion occurred at the boundary between the two plates [*Laubscher*, 1988; *Schumacher and Laubscher*, 1996; *Vignaroli et al.*, 2008] and produced an along-strike circulation of the accreted material at depth, imposed by the rigid boundaries of the subducting slabs. This resulted in a noncoaxial (top-to-the-north/NNW), synblueschist facies, flow pattern roughly parallel to the axis of the HP belt, and now represented by the HP remnants of the Liguro-Piedmont oceanic domain in the hinterland of the northern Apennines (Voltri area [*Vignaroli et al.*, 2005]; Alpine Corsica [*Daniel et al.*, 1996]; Gorgona Island [*Rossetti et al.*, 2001]). This tectonic scenario is considered to be the first step in the exhumation of the Voltri

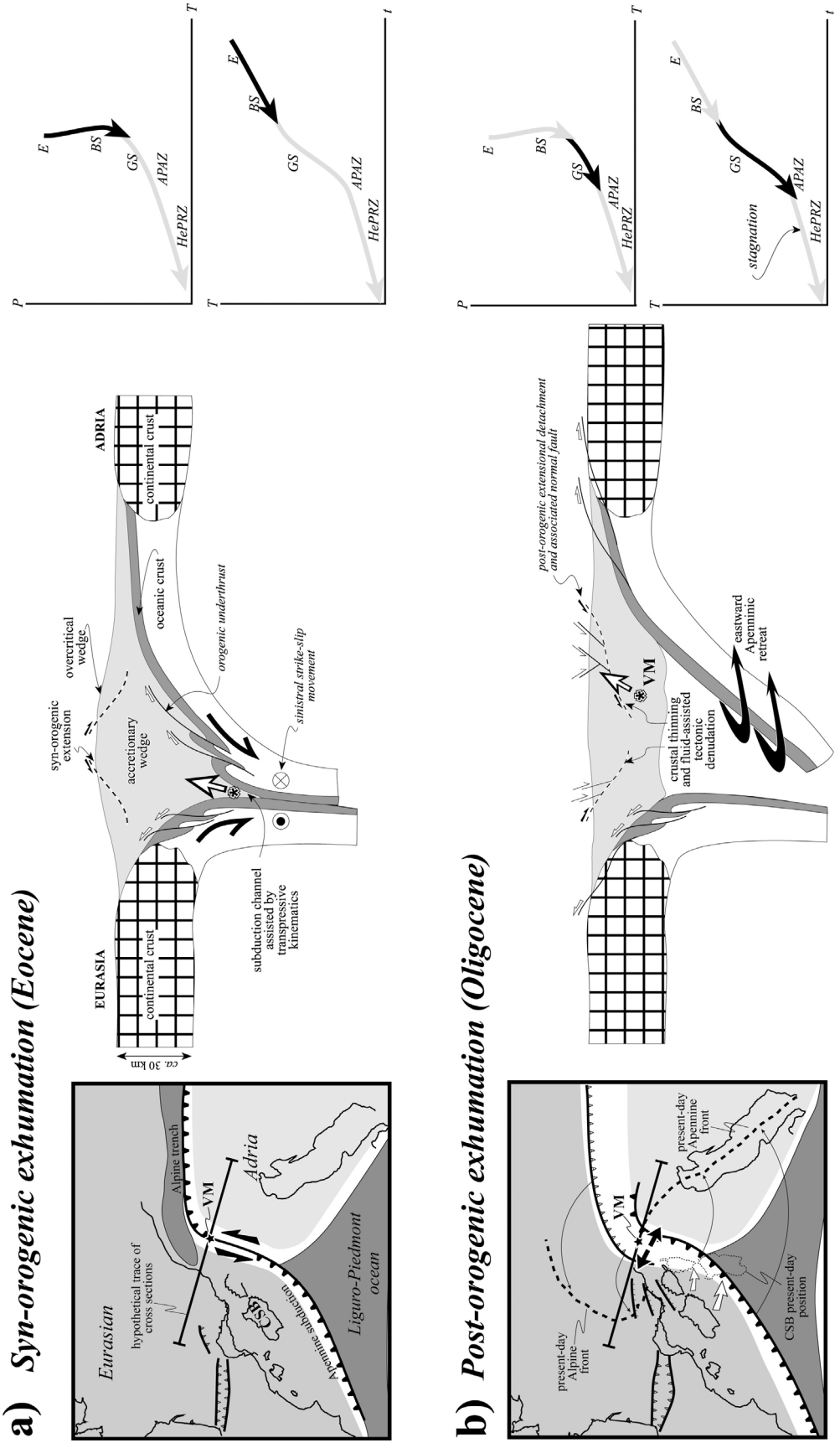

Figure 13. (a, b) Geodynamic sketch illustrating a plausible exhumation mechanism for the Voltri HP complex during synorogenic to postorogenic setting. VM, Voltri Massif; CSB, Corsica-Sardinia block.

Massif HP complex, characterized by decompression and an essentially isothermal (or slightly cooling) path (Figure 12). In this exhumation model, the far-field stress induced by the plate convergence might have also provided suitable conditions to maintain the axial region of the Alps-Apennine orogenic wedge in overcritical conditions, causing synorogenic extension and a further contribution to deep-seated rock exhumation [*Platt*, 1986]. Variable and/or episodic exhumation rates [*Rubatto and Scambelluri*, 2003; *Federico et al.*, 2007b] for the deeply accreted rocks in the subduction zone would be expected in this tectonic scenario.

[59] Postorogenic exhumation resulted from a major geodynamic reorganization in the Mediterranean region, a consequence of slowing Africa-Eurasia convergence [*Jolivet and Faccenna*, 2000]. This produced a transition from orogenic accretion to back-arc extension in the hinterland of the Alps-Apennines wedge and the onset of continental collision at the Apennine trench during eastward retreat of the Apennine slab [*Faccenna et al.*, 2004; *Rosenbaum and Lister*, 2004a] (Figure 13b). At this time, the tectonic regime was dominated by crustal thinning and the activation of diffuse, regional-scale, extensional detachment systems along the hinterland of the Apennine belt [e.g., *Jolivet et al.*, 1998]. In the Voltri Massif, this resulted in activation of major normal-sense displacements during E-W crustal stretching [*Vignaroli et al.*, 2008], concomitant with intense fluid-rock interaction as indicated by the high rate of (post-33 Ma) cooling recorded in the exhumed HP rocks. High cooling rates are a typical signature of lower plate rocks exhumed below extensional detachment faults [*Morrison and Anderson*, 1998; *Augier et al.*, 2005]. Extensional tectonics produced the regional D_2 syngreenschist mylonitic fabric overprinting the earlier HP fabric in both the Voltri and other distinctive units (such as the Palmaro-Caffarella Unit; see also the discussions by *Capponi et al.* [2009] and *Vignaroli et al.* [2009b]), consistent with a common postorogenic evolution.

[60] Postorogenic extension dominantly operated during the Oligocene, when a major regional cooling/exhumation episode is recorded throughout the Ligurian Alps [*Barbieri et al.*, 2003; *Bertotti et al.*, 2006], which continued until the Early Miocene when the Voltri HP complex entered the APAZ. In the Early Oligocene (at ~ 30 Ma), the Corsica-Sardinia block started to rotate away from Europe, causing rifting of the Ligurian-Provençal Basin [*Faccenna et al.*, 1997; *Rosenbaum and Lister*, 2004b]. After breakup (at ~ 20 Ma), the Ligurian Alps became part of the northern passive continental margin of the Ligurian-Provençal ocean and rotated about 50°CCW with respect to nearby plates during Aquitanian-Serravallian times [*Maffione et al.*, 2008]. Drifting ended at ~ 16 Ma when extension migrated east of the Corsica-Sardinia block, causing opening of the Tyrrhenian Sea [*Patacca et al.*, 1990; *Faccenna et al.*, 1997]. *Bertotti et al.* [2006] have demonstrated that the rifting/drifting episodes cannot explain the spatial and temporal pattern of vertical movements recorded in the Ligurian Alps and the TPB. Our preliminary AFT data confirm this scenario and argue for stagnation of the exhumation process (T-t path in Figure 13b) after the Early Miocene. We conclude that the T-t exhumation trajectory starting from greenschist facies conditions can be reconciled with the transition from the rifting phase in the Ligurian-Provençal Basin (33–24 Ma) to the drifting of the Corsica-Sardinia block (20–16 Ma), and to the final assembly of the already exhumed Voltri units in the Pliocene-Quaternary compressional setting of the Po Plain area [e.g., *Dela Pierre et al.*, 1995; *Mosca et al.*, 2010].

10. Conclusions

[61] The data presented in this paper provide the basis for proposing a unitary P-T-d-t exhumation path for the Voltri HP units. The exhumation scenario proposed here involves a two-stage process, evolving from a synorogenic to postorogenic setting, occurred at the Alps-Apennines junction during the Tertiary. Early synorogenic exhumation (Eocene) occurred within the subduction zone and was driven by the circulation path imposed at depth by the transpressive kinematics at the convergent plate boundaries. Subsequent postorogenic exhumation (from syngreenschist metamorphic facies to upper crustal conditions) occurred during crustal thinning linked to a regional geodynamic reorganization of the Mediterranean region and concurrent opening of the Liguro-Provençal Basin (Oligocene). This two-stage exhumation history was accomplished by variable exhumation/cooling rates during the synorogenic stage and by a relatively high cooling rate (up to 40°C Ma^{-1}) during the postorogenic stage.

[62] Our data also have implications for the tectonic regime in the internal portions of the Western Alps during the Late Eocene/Early Oligocene time period. In fact, the Late Eocene/Early Oligocene age clusters from the exposed (U)HP units have been interpreted as evidence for either subduction-related [e.g., *Duchêne et al.*, 1997; *Gebauer et al.*, 1997; *Rubatto and Hermann*, 2001; *Rubatto and Scambelluri*, 2003; *Di Vincenzo et al.*, 2006] or exhumation-related tectonics [e.g., *Barnicoat et al.*, 1995; *Freeman et al.*, 1997; *Agard et al.*, 2002; *Cartwright and Barnicoat*, 2002; *Reddy et al.*, 2003; *Meffan-Main et al.*, 2004]. Our arguments, in terms of age, style and kinematics of postorogenic deformation, support a major Early Oligocene tectonic unroofing stage for the entire Western Alps orogenic belt, likely corresponding to activation of regional-scale extensional detachment tectonics [see also *Philippot*, 1990; *Wheeler and Butler*, 1993; *Agard et al.*, 2002; *Reddy et al.*, 2003].

Appendix A: Analytical Techniques

A1. Electron Microprobe

[63] Mineral compositions for ARESCI, DES, 8D, BEIG and VOL samples were determined using a CAMECA SX100 electron microprobe at the University of Stuttgart. Mineral compositions for FAB, FADO and MAS samples were determined using a CAMECA SX 50 electron microprobe at the CNR laboratories (Istituto di Geologia Ambientale e Geoingegneria, c/o Dipartimento di Scienze della Terra, University of Rome "La Sapienza"). Both sets of analyses were performed in static beam mode (focused or 5 μm in size) at 15 kV and 15 nA, using natural minerals and synthetic

phases as standards. Raw data were processed with the PAP software module delivered by CAMECA.

A2. U-Pb SHRIMP and Trace Elements

[64] Zircon and titanite crystals were separated on the basis of their magnetic properties and density. Separated grains were mounted in epoxy and polished to expose the grain centers. Zoning of zircon was investigated by cathodoluminescence imaging, using a HITACHI S2250-N scanning electron microscope at the Electron Microscope Unit (Australian National University), operated at 15 kV, ~60 μA and using a ~20 mm working distance. Titanite internal structures were revealed by backscattered electron images using a Cambridge S360 scanning electron microscope operated at 20 kV, 3 nA and using a ~20 mm working distance.

[65] Selected zircon and titanite domains were analyzed for U, Th and Pb using the sensitive high-resolution ion microprobe (SHRIMP II) at the Research School of Earth Sciences (ANU). Operating and instrumental conditions and data acquisition methods are described by *Compston et al.* [1992] and *Rubatto and Hermann* [2001]. For zircon, the $^{206}Pb/^{238}U$ ratios were corrected using a reference zircon from the Temora granodiorite (TEM, 417 Ma [*Black et al.*, 2003]), whereas the U contents were determined based on a zircon of known composition from Sri Lanka (SL13). For titanite, the measured $^{206}Pb/^{238}U$ ratios were corrected using a reference titanite (BLR, 1050 Ma). The data were corrected for common Pb using the measured $^{207}Pb/^{206}Pb$, as described by *Williams* [1998]. Age calculations were carried out with the Isoplot software [*Ludwig*, 2000]. Mean ages are reported at the 95% confidence level.

[66] Trace element concentrations in zircon and titanite were acquired by Laser Ablation ICP-MS at the Research School of Earth Sciences employing an ArF (193 nm) EXCIMER laser [*Eggins et al.*, 1998] combined with a Hewlett Packard Agilent 7500 ICP-MS. A spot size of between 19 and 40 μm was used and the counting time was 25 s for the background and 60 s for samples. The analyses were calibrated against a synthetic glass (NIST 612). The internal standard was Si for both zircon and titanite.

A3. The $^{40}Ar/^{39}Ar$ Geochronology

[67] Phengite separates were prepared from samples DES, ARESCI and BEIG using standard crushing, sieving, desliming, magnetic separation and heavy liquid techniques. Final separation was achieved by handpicking to > 99% purity. The samples were individually packed in aluminum foil packets and irradiated in position 5c (cadmium lined) of the McMaster University reactor, Canada, together with aliquots of the fluence monitor GA1550 (98.8 ± 0.5 Ma [*Renne et al.*, 1998]).

[68] The $^{40}Ar/^{39}Ar$ analyses were performed at the University of Melbourne, following procedures described by *Reid et al.* [2005] and *Phillips et al.* [2007]. Step heating analyses were undertaken using a tantalum resistance furnace connected to a VG3600 mass spectrometer, equipped with a Daly detector. Mass discrimination was monitored by measuring air aliquots from a calibrated pipette system. Correction factors for interfering isotopes were $(^{39}Ar/^{37}Ar)_{Ca}$ = 6.80 (±0.05), × 10^{-4}; $(^{36}Ar/^{37}Ar)_{Ca}$ = 2.89 (±0.19) × 10^{-4} and $(^{40}Ar/^{39}Ar)_{K}$ = 4.0 (±4.0) × 10^{-4}. Apparent age spectra were plotted using ISOPLOT v.3 [*Ludwig*, 2000]. Unless otherwise stated, $^{40}Ar/^{39}Ar$ ages are reported at the 1σ level.

A4. AFTA

[69] Apatite mineral concentrates from the samples were separated, mounted and etched following the procedures described by *Gleadow* [1984]. The samples were then irradiated using the well-thermalized reactor facility FRM II (Garching, Germany). The fission track analyses were performed by FL at the Universität Bremen, following the methods described by *Hurford and Green* [1982]. Standard and induced track densities were measured on mica external detectors. For dating, the FT Stage program of *Dumitru* [1993] was used. Apatite fission tracks were counted and measured with a Zeiss Axioplan microscope at magnifications of 1250 × and 2000 × , using dry objectives. Ages were calculated using the zeta method (ζ = 352 ± 12) for the dosimeter glass IRMM 540. Errors are quoted as ± 1σ (conventional method [*Green*, 1981]). Standards are Mt. Dromedary, Fish Canyon and Durango apatite. Confined fission tracks were measured following the recommendations of *Laslett et al.* [1982] whenever possible.

[70] **Acknowledgments.** F. Rossetti and G. Vignaroli dedicate this manuscript to the memory of R. Funiciello. We thank G. De Grandis (CNR Pisa) for assistance during zircons and titanites separation, M. Serracino for assistance during microprobe analyses, the Electron Microscope Unit at the Australian National University, B. Ventura for the preparation of the FT samples, S. Szczepanski for support with the $^{40}Ar/^{39}Ar$ analyses, and C. Faccenna for suggestions and constant encouragement. A. Liati is also thanked for comments on a previous version. This manuscript has also benefited from the thoughtful comments by P. Agard and an anonymous reviewer.

References

Agard, P., O. Vidal, and B. Goffé (2001), Interlayer and Si content of phengite in HP-LT carpholite-bearing metapelites, *J. Metamorph. Geol.*, *19*, 479–495, doi:10.1046/j.0263-4929.2001.00322.x.

Agard, P., P. Monié, L. Jolivet, and B. Goffé (2002), Exhumation of the Schistes Lustrés complex: In situ laser probe $^{40}Ar/^{39}Ar$ constraints and implications for the Western Alps, *J. Metamorph. Geol.*, *20*, 599–618, doi:10.1046/j.1525-1314.2002.00391.x.

Agard, P., P. Yamato, L. Jolivet, and E. Burov (2009), Exhumation of oceanic blueschists and eclogites in subduction zones: Timing and mechanisms, *Earth Sci. Rev.*, *92*, 53–79, doi:10.1016/j.earscirev.2008.11.002.

Allasinaz, A., R. Gelati, M. Gnaccolini, B. Martinis, G. Orombelli, G. Pasquarè, and P. M. Rossi (1971), *Note Illustrative Della Carta Geologica d'Italia alla Scala 1/100000: Foglio 82 Genova*, 134 pp., Serv. Geol. Ital., Rome.

Alvarez, W., T. Cocozza, and F. C. Wezel (1974), Fragmentation of the Alpine orogenic belt by microplate dispersal, *Nature*, *248*, 309–314, doi:10.1038/248309a0.

Amato, J. M., C. M. Johnson, L. P. Baumgartner, and B. L. Beard (1999), Rapid exhumation of the Zermatt-Saas ophiolite deduced from high-precision Sm-Nd and Rb-Sr geochronology, *Earth Planet. Sci. Lett.*, *171*, 425–438, doi:10.1016/S0012-821X(99)00161-2.

Augier, R., P. Agard, P. Monié, L. Jolivet, C. Robin, and G. Booth-Rea (2005), Exhumation, doming and slab retreat in the Betic Cordillera (SE Spain): In situ $^{40}Ar/^{39}Ar$ ages and P-T-d-t paths for the Nevado-Filabride complex, *J. Metamorph. Geol.*, *23*, 357–381, doi:10.1111/j.1525-1314.2005.00581.x.

Barbieri, C., B. Carrapa, A. Di Giulio, J. Wijbrans, and G. R. Murrell (2003), Provenance of Oligocene synorogenic sediments of the Ligurian Alps (NW Italy): Inferences on belt age and cooling history, *Int. J. Earth Sci.*, *92*, 758–778, doi:10.1007/s00531-003-0351-x.

Barnicoat, A. C., D. C. Rex, P. G. Guise, and R. A. Cliff (1995), The timing of and the nature of greenschist

facies deformation and metamorphism in the upper Pennine Alps, *Tectonics*, *14*, 279–293, doi:10.1029/94TC02017.

Beccaluva, L., G. Macciotta, B. Messiga, and G. B. Piccardo (1979), Petrology of the blue-schists metamorphic ophiolites of the Montenotte Nappe (western Liguria, Italy), *Ofioliti*, *4*, 239–268.

Berman, R. G. (1988), Internally-consistent thermodynamic data for minerals in the system Na_2O-K_2O-CaO-MgO-FeO-Fe_2O_3-Al_2O_3-SiO_2-TiO_2-H_2O-CO_2, *J. Petrol.*, *29*, 445–522.

Berman, R. G. (1991), Thermobarometry using multiequilibrium calculations: A new technique, with petrological applications, *Can. Mineral.*, *29*, 833–855.

Bertotti, G., P. Mosca, J. Juez, R. Polino, and T. Dunai (2006), Oligocene to present kilometres scale subsidence and exhumation of the Ligurian Alps and the Tertiary Piedmont Basin (NW Italy) revealed by apatite (U-Th)/He thermochronology: Correlation with regional tectonics, *Terra Nova*, *18*, 18–25, doi:10.1111/j.1365-3121.2005.00655.x.

Black, L. P., S. L. Kamo, C. M. Allen, J. M. Aleinikoff, D. W. Davis, R. J. Korsch, and C. Foudoulis (2003), TEMORA 1: A new zircon standard for Phanerozoic U-Pb geochronology, *Chem. Geol.*, *200*, 155–170, doi:10.1016/S0009-2541(03)00165-7.

Borghini, G., E. Rampone, L. Crispini, R. De Ferrari, and M. Godard (2007), Origin and emplacement of ultramafic-mafic intrusions in the Erro-Tobbio mantle peridotite (Ligurian Alps, Italy), *Lithos*, *94*, 210–229, doi:10.1016/j.lithos.2006.06.014.

Bousquet, R., B. Goffé, O. Vidal, R. Oberhänsli, and M. Patriat (2002), The tectono-metamorphic history of the Valaisan domain from the Western to the Central Alps: New constraints on the evolution of the Alps, *Geol. Soc. Am. Bull.*, *114*, 207–225, doi:10.1130/0016-7606(2002)114<0207:TTMHOT>2.0.CO;2.

Bowtell, S. A., R. A. Cliff, and A. C. Barnicoat (1994), Sm-Nd isotopic evidence on the age of eclogitization in the Zermatt-Saas ophiolite, *J. Metamorph. Geol.*, *12*, 187–196, doi:10.1111/j.1525-1314.1994.tb00013.x.

Brouwer, F. M., R. L. M. Vissers, and W. M. Lamb (2002), Metamorphic history of eclogitic metagabbro blocks from a tectonic mélange in the Voltri Massif, Ligurian Alps, Italy, *Ofioliti*, *27*, 1–16.

Brunet, C., P. Monié, L. Jolivet, and J. P. Cadet (2000), Migration of compression and extension in the Tyrrhenian Sea, insights from $^{40}Ar/^{39}Ar$ ages on micas along a transect from Corsica to Tuscany, *Tectonophysics*, *321*, 127–155, doi:10.1016/S0040-1951(00)00067-6.

Bucher, K., and M. Frey (2002), *Petrogenesis of Metamorphic Rocks*, 341 pp., Springer, Berlin.

Bucher, K., Y. Fazis, C. de Capitani, and R. Grapes (2005), Blueschists, eclogites, and decompression assemblages of the Zermatt-Saas ophiolite: High-pressure metamorphism of subducted Tethys lithosphere, *Am. Mineral.*, *90*, 821–835, doi:10.2138/am.2005.1718.

Burov, E., L. Jolivet, L. Le Lepourhiet, and A. Poliakov (2001), A thermomechanical model of exhumation of HP and UHP metamorphic rocks in Alpine mountain belt, *Tectonophysics*, *342*, 113–136, doi:10.1016/S0040-1951(01)00158-5.

Capponi, G. (1991), Megastructure of the south-eastern part of the Voltri Group (Ligurian Alps): A tentative interpretation, *Boll. Soc. Geol. Ital.*, *110*, 391–403.

Capponi, G., and L. Crispini (2002), Structural and metamorphic signature of alpine tectonics in the Voltri Massif (Ligurian Alps, north-western Italy), *Eclogae Geol. Helv.*, *95*, 31–42.

Capponi, G., and L. Crispini (2005), Elemento 213-4 "Campoligure," scale 1:25,000, Progetto CARG, Reg. Liguria, Genova, Italy. (Available at http://www.cartografia.regione.liguria.it/.)

Capponi, G., and L. Crispini (2006a), Elemento 213-1 "Campomorone," scale 1:25,000, Progetto CARG, Reg. Liguria, Genova, Italy. (Available at http://www.cartografia.regione.liguria.it/.)

Capponi, G., and L. Crispini (2006b), Elemento 213-2 "Genova," scale 1:25,000, Progetto CARG, Reg. Liguria, Genova, Italy. (Available at http://www.cartografia.regione.liguria.it/.)

Capponi, G., and L. Crispini (2006c), Elemento 213-3 "Pegli," scale 1:25,000, Progetto CARG, Reg. Liguria, Genova, Italy. (Available at http://www.cartografia.regione.liguria.it/.)

Capponi, G., and S. Giammarino (1982), L'affioramento oligocenico del Rio Siria (Bacino di Santa Giustina, provincia di Savona), nel quadro dei movimenti tardivi della falda di Montenotte, *Atti Soc. Tosc. Sci. Nat., Ser. A*, *89*, 101–113.

Capponi, G., M. Scambelluri, and S. Tallone (1986), Distinzione di fasi tettoniche al contatto tra le Unità Ponzema, Voltri-Rossiglione e la Falda Erro-Tobbio, Gruppo di Voltri, Alpi Liguri, *Ofioliti*, *11*, 221–234.

Capponi, G., G. Gosso, M. Scambelluri, G. B. Siletto, and S. Tallone (1994), Carta geologico-strutturale del settore centro-meridionale del Gruppo di Voltri (Alpi Liguri) e note illustrative, *Boll. Soc. Geol. Ital.*, *113*, 383–394.

Capponi, G., L. Crispini, and I. Ferrarazzo (1998), New field data on the Case Ferrere area (Voltri Massif, Ligurian Alps), *Boll. Soc. Geol. Ital.*, *117*, 87–92.

Capponi, G., L. Crispini, R. Silvestri, and E. Vigo (1999), The role of Early Miocene thrust tectonics in the structural arrangement of the Voltri Group (Ligurian Alps, Italy): Evidence from the Bandita area, *Ofioliti*, *24*, 13–19.

Capponi, G., L. Crispini, and M. Scambelluri (2009), Comment on "Subduction polarity reversal at the junction between the Western Alps and the northern Apennines, Italy," by G. Vignaroli, C. Faccenna, L. Jolivet, C. Piromallo, F. Rossetti, *Tectonophysics*, *465*, 221–226, doi:10.1016/j.tecto.2008.10.019.

Carrapa, B., A. Di Giulio, and J. Wijbrans (2004), The early stages of the Alpine collision: An image derived from the upper Eocene-lower Oligocene record in the Alps-Apennines junction area, *Sediment. Geol.*, *171*, 181–203, doi:10.1016/j.sedgeo.2004.05.015.

Cartwright, I., and A. C. Barnicoat (2002), Petrology, geochronology, and tectonics of the shear zones in the Zermatt-Saas and Combin zones of the Western Alps, *J. Metamorph. Geol.*, *20*, 263–281, doi:10.1046/j.0263-4929.2001.00366.x.

Challandes, N., D. Marquer, and I. M. Villa (2003), Dating the evolution of C-S microstructures: A combined $^{40}Ar/^{39}Ar$ step-heating and UV laser-probe analysis of the Alpine Roffna shear zone, *Chem. Geol.*, *197*, 3–19, doi:10.1016/S0009-2541(02)00354-6.

Charrier, G., D. Fernandez, and R. Malaroda (1964), La formazione di Pianfolco (Bacino Oligocenico Ligure-Piemontese), *Atti Accad. Naz. Lincei*, *8*(2), 25–81.

Chemenda, A. I., M. Mattauer, J. Malavieille, and A. N. Bokun (1995), A mechanism for syn-collision rock exhumation and associated normal faulting: Results from physical modelling, *Earth Planet. Sci. Lett.*, *132*, 225–232, doi:10.1016/0012-821X(95)00042-B.

Chiesa, S., L. Cortesogno, F. Forcella, M. Galli, B. Messiga, G. Pasquaré, G. M. Pedemonte, G. B. Piccardo, and P. M. Rossi (1975), Assetto strutturale ed interpretazione geodinamica del Gruppo di Voltri, *Boll. Soc. Geol. Ital.*, *94*, 555–581.

Chopin, C. (1984), Coesite and pure pyrope in high-grade blueschists of the Western Alps: A first record and some consequences, *Contrib. Mineral. Petrol.*, *86*, 107–118, doi:10.1007/BF00381838.

Chopin, C. (2003), Ultrahigh-pressure metamorphism: Tracing continental crust into the mantle, *Earth Planet. Sci. Lett.*, *212*, 1–14, doi:10.1016/S0012-821X(03)00261-9.

Cimmino, F., and B. Messiga (1979), I calcescisti del Gruppo di Voltri (Liguria Occidentale): Le variazioni composizionali delle miche bianche in rapporto alla evoluzione tettonico-metamorfica alpina, *Ofioliti*, *4*, 269–294.

Cliff, R. A., A. C. Barnicoat, and S. Inger (1998), Early Tertiary eclogite-facies metamorphism in the Monviso Ophiolite, *J. Metamorph. Geol.*, *16*, 447–455.

Cloos, M. (1982), Flow melanges: Numerical modeling and geologic constraints on their origin in the Franciscan subduction complex, California, *Geol. Soc. Am. Bull.*, *93*, 330–345, doi:10.1130/0016-7606(1982)93<330:FMNMAG>2.0.CO;2.

Compston, W., I. S. Williams, J. L. Kirschvink, Z. Zhang, and M. A. Guogan (1992), Zircon U-Pb ages for the Early Cambrian time-scale, *J. Geol. Soc. London*, *149*, 171–184, doi:10.1144/gsjgs.149.2.0171.

Cortesogno, L., and D. Haccard (1984), Note illustrative alla carta geologica della Zona Sestri-Voltaggio, *Mem. Soc. Geol. Ital.*, *28*, 115–150.

Crispini, L., and G. Capponi (1997), Quartz fabric and strain partitioning in sheath folds: An example from the Voltri Group (Western Alps, Italy), *J. Struct. Geol.*, *19*, 1149–1157, doi:10.1016/S0191-8141(97)00035-7.

Crispini, L., and M. L. Frezzotti (1998), Fluid inclusion evidence for progressive folding during decompression in metasediments of the Voltri Group (Western Alps, Italy), *J. Struct. Geol.*, *20*, 1733–1746, doi:10.1016/S0191-8141(98)00087-X.

Dal Piaz, G. V., G. Cortiana, A. Del Moro, S. Martin, G. Pennacchioni, and P. Tartarotti (2001), Tertiary age and paleostructural inferences of the eclogitic imprint in the Austroalpine outliers and Zermatt-Saas ophiolite, western Alps, *Int. J. Earth Sci.*, *90*, 668–684.

Daniel, J.-M., L. Jolivet, B. Goffé, and C. Poinssot (1996), Crustal-scale strain partitioning: Footwall deformation below the Alpine Oligo-Miocene detachment of Corsica, *J. Struct. Geol.*, *18*, 41–59, doi:10.1016/0191-8141(95)00075-O.

Dela Pierre, F., V. Mikhailov, and R. Polino (1995), The tectonosedimentary evolution of the tertiary basins in the western Po plain: Kinematics inferred from subsidence curves: Atti del convegno—"Rapporti tra Alpi e Appennino," *Acc. Naz. Sci.*, *11*, 129–146.

Dewey, J. F., M. L. Helman, E. Turco, D. H. W. Hutton, and S. D. Knott (1989), Kinematics of the western Mediterranean, in *Alpine Tectonics*, edited by M. P. Coward, D. Dietrich, and R. G. Park, *Geol. Soc. Spec. Publ.*, *45*, 265–283.

Di Biase, D., and L. Pandolfi (1999), I Conglomearti della Val Borbera (Bacino Terziario Piemontese) e relative implicazioni per l'esumazione di unita' alpine a metamorfismo di alta pressione/bassa temperature: Riunione del Gruppo Informale di Sedimentologia, Rimini, *G. Geol.*, *61*, 178–181.

Di Vincenzo, G., S. Tonarini, B. Lombardo, D. Castelli, and L. Ottolini (2006), Comparison of ^{40}Ar-^{39}Ar and Rb-Sr data on phengites from the UHP Brossasco-Isasca Unit (Dora Maira Massif, Italy): Implications for dating white mica, *J. Petrol.*, *47*, 1439–1465, doi:10.1093/petrology/egl018.

Dodson, M. H. (1973), Closure temperature in cooling geochronological and petrological systems, *Contrib. Mineral. Petrol.*, *40*, 259–274, doi:10.1007/BF00373790.

Duchêne, S., J. Blichert-Toft, B. Luais, P. Télouk, J.-M. Lardeaux, and F. Albarède (1997), The Lu-Hf dating of garnets and the ages of the Alpine high-pressure metamorphism, *Nature*, *387*, 586–589, doi:10.1038/42446.

Dumitru, T. A. (1993), A new computer-automated microscope stage system for fission-track analysis, *Nucl. Tracks Radiat. Meas.*, *21*(4), 575–580, doi:10.1016/1359-0189(93)90198-I.

Eggins, S. M., R. L. Rudnick, and W. F. McDonough (1998), The composition of peridotites and their minerals: A laser ablation ICP-MS study, *Earth Planet. Sci. Lett.*, *154*, 53–71, doi:10.1016/S0012-821X(97)00195-7.

Ernst, W. G. (1981), Petrogenesis of eclogites and peridotites from the Western and Ligurian Alps, *Am. Mineral.*, *66*, 443–472.

Ernst, W. G. (1988), Tectonic history of subduction zones inferred from retrograde blueschist P-T paths, *Geology*, *16*, 1081–1084, doi:10.1130/0091-7613(1988)016<1081:THOSZI>2.3.CO;2.

Faccenna, C., M. Mattei, R. Funiciello, and L. Jolivet (1997), Styles of back-arc extension in the central Mediterranean, *Terra Nova*, *9*, 126–130.

Faccenna, C., C. Piromallo, A. Crespo-Blanc, L. Jolivet, and F. Rossetti (2004), Lateral slab deformation and the origin of the western Mediterranean arcs, *Tectonics*, *23*, TC1012, doi:10.1029/2002TC001488.

Federico, L., G. Capponi, L. Crispini, and M. Scambelluri (2004), Exhumation of alpine high-pressure rocks: Insights from petrology of eclogite clasts in the Tertiary Piedmontese basin (Ligurian Alps, Italy), *Lithos*, *74*, 21–40, doi:10.1016/j.lithos.2003.12.001.

Federico, L., G. Capponi, L. Crispini, M. Scambelluri, and I. M. Villa (2005), $^{39}Ar/^{40}Ar$ dating of high-pressure rocks from the Ligurian Alps: Evidence for a continuous subduction-exhumation cycle, *Earth Planet. Sci. Lett.*, *240*, 668–680, doi:10.1016/j.epsl.2005.09.062.

Federico, L., L. Crispini, M. Scambelluri, and G. Capponi (2007a), Different PT paths recorded in a tectonic mélange (Voltri Massif, NW Italy): Implications for the exhumation of HP rocks, *Geodin. Acta*, *20*, 3–19, doi:10.3166/ga.20.3-19.

Federico, L., L. Crispini, M. Scambelluri, and G. Capponi (2007b), Ophiolite mélange zone records exhumation in a fossil subduction channel, *Geology*, *35*, 499–502, doi:10.1130/G23190A.1.

Fitzgerald, P.G., S. L. Baldwin, L. E. Webb, and P. B. O'Sullivan (2006), Interpretation of (U-Th)/He single grain ages from slowly cooled crustal terranes: A case study from the Transantarctic Mountains of southern Victoria Land, *Chem. Geol.*, *225*, 91–120.

Franceschetti, B. (1967), Studi geologici sulla regione ad ovest di Ovada (provincia di Alessandria), *Mem. Soc. Geol. Ital.*, *6*, 379–420.

Freeman, S. R., S. Inger, R. W. H. Butler, and R. A. Cliff (1997), Dating deformation using Rb-Sr in white mica: Greenschist facies deformation ages from the Entrelor shear zone, Italian Alps, *Tectonics*, *16*, 57–76, doi:10.1029/96TC02477.

Fügenschuh, B., and S. M. Schmid (2003), Late stages of deformation and exhumation of an orogen constrained by fission-track data: A case study in the Western Alps, *Geol. Soc. Am. Bull.*, *115*, 1425–1440, doi:10.1130/B25092.1.

Fügenschuh, B., D. Seward, and N. Mancktelow (1997), Exhumation in a convergent orogen: The western Tauern window, *Terra Nova*, *9*, 213–217.

Gabudianu Radulescu, I., D. Rubatto, C. Gregory, and R. Compagnoni (2009), The age of HP metamorphism in the Gran Paradiso Massif, Western Alps: A petrological and geochronological study of "silvery micaschists", *Lithos*, *110*, 95–108, doi:10.1016/j.lithos.2008.12.008.

Gebauer, D., H. P. Schertl, M. Brix, and W. Schreyer (1997), 35 Ma old ultrahigh-pressure metamorphism and evidence for very rapid exhumation in the Dora Maira Massif, Western Alps, *Lithos*, *41*, 5–24, doi:10.1016/S0024-4937(97)82002-6.

Geisler, T., U. Schaltegger, and F. Tomaschek (2007), Re-equilibration of zircon in aqueous fluids and melts, *Elements*, *3*, 43–50, doi:10.2113/gselements.3.1.43.

Gelati, R., and M. Gnaccolini (1998), Sedimentary tectonics and sedimentation in the Tertiary Piedmont Basin, north-western Italy, *Riv. Ital. Paleontol. Stratigr.*, *104*, 193–214.

Gelati, R., M. Gnaccolini, P. Falletti, and D. Citrullo (1993), Stratigrafia sequenziale della successione Oligo-Miocenica delle Langhe, Bacino Terziario Ligure-Piemontese, *Riv. Ital. Paleontol. Stratigr.*, *98*, 425–452.

Gerya, T. V., B. Stöckhert, and A. L. Perchuk (2002), Exhumation of high-pressure metamorphic rocks in a subduction channel: A numerical simulation, *Tectonics*, *21*(6), 1056, doi:10.1029/2002TC001406.

Gleadow, A. J. W. (1984), Fission track dating methods II—A manual of principles and techniques, paper presented at Workshop on Fission Track Analysis: Principles and Applications, James Cook Univ., Townsville, Qld., Australia.

Green, P. F. (1981), A new look at statistics in fission-track dating, *Nucl. Tracks*, *5*(1–2), 77–86, doi:10.1016/0191-278X(81)90029-9.

Green, P. F., I. R. Duddy, A. J. W. Gleadow, and J. F. Lovering (1989), Apatite fission-track analysis as palaeotemperature indicator for hydrocarbon exploration, in *Thermal History of Sedimentary Basins*, edited by N. D. Naeser and T. H. McCulloh, pp. 181–195, Springer, New York.

Harley, S. L., N. M. Kelly, and A. Möller (2007), Zircon behaviour and the thermal histories of mountain chains, *Elements*, *3*, 25–30, doi:10.2113/gselements.3.1.25.

Hermann, J., O. Müntener, and M. Scambelluri (2000), The importance of serpentinite mylonites for subduction and exhumation of oceanic crust, *Tectonophysics*, *327*, 225–238, doi:10.1016/S0040-1951(00)00171-2.

Hoogerduijn Strating, E. H. (1991), The evolution of the Piemonte-Ligurian Ocean: A structural study of ophiolite complexes in Liguria (NW Italy), Ph.D. thesis, 127 pp., Univ. of Utrecht, Utrecht, Netherlands.

Hoogerduijn Strating, E. H. (1994), Extensional faulting in an intraoceanic subduction complex—Working hypothesis for the Palaeogene of the Alps-Apennine system, *Tectonophysics*, *238*, 255–273, doi:10.1016/0040-1951(94)90059-0.

Hoogerduijn Strating, E. H., E. Rampone, G. B. Piccardo, M. R. Drury, and R. L. M. Vissers (1993), Subsolidus emplacement of mantle peridotites during incipient oceanic rifting and opening of the Mesozoic Tethys (Voltri Massif, NW Italy), *J. Petrol.*, *34*, 901–927.

Hoskin, P. W. O., and U. Schaltegger (2003), The composition of zircon and igneous and metamorphic petrogenesis, in *Zircon: Reviews in Mineralogy and Geochemistry*, vol. 53, edited by J. M. Hanchar and P. W. O. Hoskin, pp. 27–62, Mineral. Soc. of Am., Washington, D. C.

Hurford, A. J., and P. F. Green (1982), A users guide to fission track dating calibration, *Earth Planet. Sci. Lett.*, *59*, 343–354, doi:10.1016/0012-821X(82)90136-4.

Hurford, A. J., J. C. Hunziker, and B. Stöckhert (1991), Constraints on the late thermotectonic evolution of the Western Alps: Evidence for episodic rapid uplift, *Tectonics*, *10*, 758–769, doi:10.1029/91TC00167.

Inger, S., W. Ramsbotham, R. A. Cliff, and D. C. Rex (1996), Metamorphic evolution of the Sesia-Lanzo Zone, Western Alps: Time constraints from multi-system geochronology, *Contrib. Mineral. Petrol.*, *126*, 152–168, doi:10.1007/s004100050241.

Jolivet, L., and C. Faccenna (2000), Mediterranean extension and the Africa-Eurasia collision, *Tectonics*, *19*, 1095–1106.

Jolivet, L., B. Goffé, R. Bousquet, R. Oberhänsli, and A. Michard (1998), Detachments in high-pressure mountain belts: Tethyan examples, *Earth Planet. Sci. Lett.*, *160*, 31–47, doi:10.1016/S0012-821X(98)00079-X.

Jolivet, L., C. Faccenna, B. Goffé, E. Burov, and P. Agard (2003), Subduction tectonics and exhumation of high-pressure metamorphic rocks in the Mediterranean orogens, *Am. J. Sci.*, *303*, 353–409, doi:10.2475/ajs.303.5.353.

Kelley, S. (2002), Excess argon in K-Ar and Ar-Ar geochronology, *Chem. Geol.*, *188*, 1–22, doi:10.1016/S0009-2541(02)00064-5.

Kretz, R. (1983), Symbols for rock-forming minerals, *Am. Mineral.*, *68*, 277–279.

Laslett, G. M., W. S. Kendall, A. J. W. Gleadow, and I. R. Duddy (1982), Bias in measurement of fission-track length distributions, *Nucl. Tracks Radiat. Meas.*, *6*(2–3), 79–85.

Laubscher, H. P. (1988), The arcs of the Western Alps and the northern Apennines: An updated review, *Tectonophysics*, *146*, 67–78, doi:10.1016/0040-1951(88)90082-0.

Liati, A., and D. Gebauer (1999), Constraining the prograde and retrograde P-T-t path of Eocene HP rocks by SHRIMP dating of different zircon domains: Inferred rates of heating, burial, cooling and exhumation for central Rhodope, northern Greece, *Contrib. Mineral. Petrol.*, *135*, 340–354.

Liou, J. G., R. Zhang, W. G. Ernst, J. Liu, and R. McLimans (1998), Mineral parageneses in the Piampaludo eclogitic body, Gruppo di Voltri, western Ligurian Alps, *Schweiz. Mineral. Petrogr. Mitt.*, *78*, 317–355.

Lips, A. L. W., S. H. White, and J. R. Wijbrans (1998), $^{40}Ar/^{39}Ar$ laserprobe direct dating of discrete deformational events: A continuous record of early Alpine tectonics in the Pelagonian Zone, NW Aegean area, Greece, *Tectonophysics*, *298*, 133–153, doi:10.1016/S0040-1951(98)00181-4.

Ludwig, K. R. (2000), *Isoplot/Ex Version 2.4: A Geochronological Toolkit for Microsoft Excel*, 56 pp., Berkeley Geochronol. Cent., Berkeley, Calif.

Maffione, M., F. Speranza, C. Faccenna, A. Cascella, G. Vignaroli, and L. Sagnotti (2008), A synchronous Alpine and Corsica-Sardinia rotation, *J. Geophys. Res.*, *113*, B03104, doi:10.1029/2007JB005214.

Malusà, M. G., and G. Vezzoli (2006), Interplay between erosion and tectonics in the Western Alps, *Terra Nova*, *18*, 104–108, doi:10.1111/j.1365-3121.2006.00669.x.

Malusà, M. G., R. Polino, M. Zattin, G. Bigazzi, S. Martin, and F. Piana (2005), Miocene to present differential exhumation in the Western Alps: Insights from fission track thermochronology, *Tectonics*, *24*, TC3004, doi:10.1029/2004TC001782.

Markley, M. J., C. Teyssier, M. A. Cosca, R. Caby, J. C. Hunziker, and M. Sartori (1998), Alpine deformation and $^{40}Ar/^{39}Ar$ geochronology of synkinematic white mica in the Siviez-Mischabel Nappe, western Pennine Alps, Switzerland, *Tectonics*, *17*, 407–425, doi:10.1029/98TC00560.

Massonne, H. J., and W. Schreyer (1987), Phengite geobarometry based on the limiting assemblage with K-feldspar, phlogopite, and quartz, *Contrib. Mineral. Petrol.*, *96*, 212–224, doi:10.1007/BF00375235.

Meffan-Main, S., R. A. Cliff, A. C. Barnicoat, B. Lombardo, and R. Compagnoni (2004), A Tertiary age for Alpine high-pressure metamorphism in the Gran Paradiso massif, Western Alps: A Rb-Sr microsampling study, *J. Metamorph. Geol.*, *22*, 267–281, doi:10.1111/j.1525-1314.2004.00512.x.

Messiga, B., and M. Scambelluri (1991), Retrograde P-T-t path for the Voltri Massif eclogites (Ligurian Alps, Italy): Some tectonic implications, *J. Metamorph. Geol.*, *9*, 93–109, doi:10.1111/j.1525-1314.1991.tb00506.x.

Messiga, B., G. Piccardo, and A. Mazzuccotelli (1977), Le prasiniti del Gruppo di Voltri: Le caratteristiche petrografiche e chimiche, *Rend. Soc. Ital. Mineral. Petrol.*, *33*, 549–581.

Messiga, B., G. B. Piccardo, and W. G. Ernst (1983), High-pressure Eo-Alpine parageneses developed in magnesian metagabbros, Gruppo di Voltri, western Liguria, Italy, *Contrib. Mineral. Petrol.*, *83*, 1–15, doi:10.1007/BF00373074.

Messiga, B., G. B. Piccardo, E. Rampone, and M. Scambelluri (1989), Primary characters and high pressure metamorphic evolution of the subducted oceanic lithosphere of the Voltri Massif (Ligurian Alps-Northern Italy), *Ofioliti*, *14*, 157–175.

Monié, P., and C. Chopin (1991), $^{40}Ar/^{39}Ar$ dating in coesite-bearing and associated units of the Dora Maira massif, Western Alps, *Eur. J. Mineral.*, *3*, 239–262.

Monié, P., J. Galindo-Zaldìvar, F. Gonzalez Lodeiro, B. Goffé, and A. Jabaloy (1991), $^{40}Ar/^{39}Ar$ geochronology of Alpine tectonism in the Betic Cordilleras (southern Spain), *J. Geol. Soc. London*, *148*, 288–297.

Morrison, J., and J. L. Anderson (1998), Footwall refrigeration along a detachment fault: Implications for the thermal evolution of core complexes, *Science*, *279*, 63–66, doi:10.1126/science.279.5347.63.

Mosca, P., R. Polino, S. Rogledi, and M. Rossi (2010), New data for the kinematic interpretation of the Alps-Apennines junction (northwestern Italy), *Int.*

J. Earth Sci., *99*, 833–849, doi:10.1007/s00531-009-0428-2.

Mutti, E., L. Papani, B. Di, D. Iase, G. Davoli, S. Mora, S. Segadelli, and R. Tinterri (1995), Il Bacino Terziario Epimesoalpino e le sue implicazioni sui rapporti tra Alpi e Appennino, *Mem. Sci. Geol.*, *47*, 217–244.

Oberhänsli, R., B. Goffé, and R. Bousquet (1995), Record of a HP-LT metamorphic evolution in the Valais zone: Geodynamic implications, *Boll. Mus. Reg. Sci. Nat.*, *13*, 221–239.

Otsuki, M., and S. Banno (1990), Prograde and retrograde metamorphism of hematite-bearing basic schists in the Sanbagawa belt in central Shikoku, *J. Metamorph. Geol.*, *8*, 425–439, doi:10.1111/j.1525-1314.1990.tb00629.x.

Paquette, J.-L., C. Chopin, and J.-J. Peucat (1989), U-Pb zircon, Rb-Sr and Sm-Nd geochronology of high- to very-high-pressure meta-acidic rocks from the Western Alps, *Contrib. Mineral. Petrol.*, *101*, 280–289, doi:10.1007/BF00375313.

Parra, T., O. Vidal, and L. Jolivet (2002), Relation between the intensity of deformation and retrogression in blueschist metapelites of Tinos Island (Greece) evidenced by chlorite-mica local equilibria, *Lithos*, *63*, 41–66, doi:10.1016/S0024-4937(02)00115-9.

Passchier, C. W., and R. A. J. Trouw (2005), *Microtectonics*, 371 pp., Springer, Berlin.

Patacca, E., R. Sartori, and P. Scandone (1990), Tyrrhenian basin and Apenninic arcs: Kinematic relation since late Tortonian times, *Mem. Soc. Geol. Ital.*, *45*, 425–451.

Philippot, P. (1990), Opposite vergence of nappes and crustal extension in the French-Italian Western Alps, *Tectonics*, *9*, 1143–1164, doi:10.1029/TC009i005p01143.

Phillips, G., C. J. L. Wilson, D. Phillips, and S. Szczepanski (2007), Thermochronological ($^{40}Ar/^{39}Ar$) evidence for Early Palaeozoic basin inversion within the southern Prince Charles Mountains, East Antarctica: Implications for East Gondwana, *J. Geol. Soc.*, *164*, 771–784, doi:10.1144/0016-76492006-073.

Piana, F., S. Tallone, S. Cavagna, and A. Conti (2006), Thrusting and faulting in metamorphic and sedimentary units of Ligurian Alps: An example of integrated field work and geochemical analyses, *Int. J. Earth Sci.*, *95*, 413–430, doi:10.1007/s00531-005-0040-z.

Platt, J. P. (1986), Dynamics of orogenic wedges and the uplift of high-pressure metamorphic rocks, *Geol. Soc. Am. Bull.*, *97*, 1037–1053, doi:10.1130/0016-7606(1986)97<1037:DOOWAT>2.0.CO;2.

Platt, J. P. (1993), Exhumation of high-pressure rocks: A review of concepts and processes, *Terra Nova*, *5*, 119–133, doi:10.1111/j.1365-3121.1993.tb00237.x.

Rasmussen, B. (2005), Zircon growth in very low grade metasedimentary rocks: Evidence for zirconium mobility at ~250°C, *Contrib. Mineral. Petrol.*, *150*, 146–155, doi:10.1007/s00410-005-0006-y.

Reddy, S. M., J. Wheeler, and R. A. Cliff (1999), The geometry and timing of orogenic extension: An example from the Western Italian Alps, *J. Metamorph. Geol.*, *17*, 573–590.

Reddy, S. M., J. Wheeler, R. W. H. Butler, R. A. Cliff, S. Freeman, S. Inger, C. Pickles, and S. P. Kelley (2003), Kinematic reworking and exhumation within the convergent Alpine orogen, *Tectonophysics*, *365*, 77–102, doi:10.1016/S0040-1951(03)00017-9.

Reid, A. J., A. P. Fowler, D. Phillips, and C. J. L. Wilson (2005), Thermochronology of the Yidun Arc, central eastern Tibetan Plateau: Constraints from $^{40}Ar/^{39}Ar$ K-feldspar and apatite fission track data, *J. Asian Earth Sci.*, *25*, 915–935, doi:10.1016/j.jseaes.2004.09.002.

Reinecke, T. (1998), Prograde high- to ultrahigh-pressure metamorphism and exhumation of oceanic sediments at Lago di Cignana, Zermatt-Saas Zone, Western Alps, *Lithos*, *42*, 147–189, doi:10.1016/S0024-4937(97)00041-8.

Renne, P. R., C. C. Swisher, A. L. Deino, D. B. Karner, T. L. Owens, and D. J. DePaolo (1998), Intercalibration of standards, absolute ages and uncertainties in $^{40}Ar/^{39}Ar$ dating, *Chem. Geol.*, *145*, 117–152, doi:10.1016/S0009-2541(97)00159-9.

Rimmelé, G., T. Parra, B. Goffé, R. Oberhänsli, L. Jolivet, and O. Candan (2005), Exhumation paths of high-pressure-low-temperature metamorphic rocks from the Lycian Nappes and the Menderes Massif (SW Turkey): A multi-equilibrium approach, *J. Petrol.*, *46*, 641–669, doi:10.1093/petrology/egh092.

Ring, U., M. T. Brandon, S. D. Willett, and G. S. Lister (1999), Exhumation processes, in *Exhumation Processes: Normal Faulting*, *Ductile Flow and Erosion*, edited by U. Ring et al., *Geol. Soc. Spec. Publ.*, *154*, 1–27.

Rosenbaum, G., and G. S. Lister (2004a), Neogene and Quaternary rollback evolution of the Tyrrhenian Sea, the Apennines, and the Sicilian Maghrebides, *Tectonics*, *23*, TC1013, doi:10.1029/2003TC001518.

Rosenbaum, G., and G. S. Lister (2004b), Formation of the arcuate orogenic belts in the western Mediterranean region, *Spec. Pap. Geol. Soc. Am.*, *383*, 41–56.

Rosenbaum, G., and G. S. Lister (2005), The Western Alps from the Jurassic to Oligocene: Spatio-temporal constraints and evolutionary reconstructions, *Earth Sci. Rev.*, *69*, 281–306, doi:10.1016/j.earscirev.2004.10.001.

Rossetti, F., C. Faccenna, L. Jolivet, R. Funiciello, B. Goffé, F. Tecce, C. Brunet, P. Monié, and O. Vidal (2001), Structural signature and exhumation P-T-t path of the Gorgona blueschist sequence (Tuscan Archipelago, Italy), *Ofioliti*, *26*, 175–186.

Rubatto, D. (2002), Zircon trace element geochemistry: Distribution coefficients and the link between U-Pb ages and metamorphism, *Chem. Geol.*, *184*, 123–138, doi:10.1016/S0009-2541(01)00355-2.

Rubatto, D., and J. Hermann (2001), Exhumation as fast as subduction?, *Geology*, *29*, 3–6, doi:10.1130/0091-7613(2001)029<0003:EAFAS>2.0.CO;2.

Rubatto, D., and J. Hermann (2003), Zircon formation during fluid circulation in eclogites (Monviso, Western Alps): Implications for Zr and Hf budget in subduction zones, *Geochim. Cosmochim. Acta*, *67*, 2173–2187.

Rubatto, D., and M. Scambelluri (2003), U-Pb dating of magmatic zircon and metamorphic baddeleyite in the Ligurian eclogites (Voltri Massif, Western Alps), *Contrib. Mineral. Petrol.*, *146*, 341–355, doi:10.1007/s00410-003-0502-x.

Rubatto, D., D. Gebauer, and M. Fanning (1998), Jurassic formation and Eocene subduction of the Zermatt-Saas-Fee ophiolites: Implications for the geodynamic evolution of the Central and Western Alps, *Contrib. Mineral. Petrol.*, *132*, 269–287.

Rubatto, D., D. Gebauer, and R. Compagnoni (1999), Dating of eclogite-facies zircons: The age of Alpine metamorphism in the Sesia-Lanzo Zone (Western Alps), *Earth Planet. Sci. Lett.*, *167*, 141–158, doi:10.1016/S0012-821X(99)00031-X.

Scaillet, S., G. Féraud, Y. Lagabrielle, M. Ballèvre, and G. Ruffet (1990), $^{40}Ar/^{39}Ar$ laser-probe dating by step-heating and spot-fusion of phengites from the Dora Maira nappe of the western Alps, Italy, *Geology*, *18*, 741–744.

Scaillet, S., G. Féraud, M. Ballèvre, and M. Amouric (1992), Mg/Fe and [(Mg, Fe)Si-Al_2] compositional control on Ar behaviour in high-pressure white micas: A $^{40}Ar/^{39}Ar$ continuous laser-probe study from the Dora-Maira nappe of the internal Western Alps, Italy, *Geochim. Cosmochim. Acta*, *56*, 2851–2872, doi:10.1016/0016-7037(92)90364-O.

Scambelluri, M., E. H. Hoogerduijn Strating, G. B. Piccardo, R. L. M. Vissers, and E. Rampone (1991), Alpine olivine- and titanian clinohumite-bearing assemblages in the Erro-Tobbio peridotite (Voltri Massif, NW Italy), *J. Metamorph. Geol.*, *9*, 79–91, doi:10.1111/j.1525-1314.1991.tb00505.x.

Scambelluri, M., O. Müntener, J. Hermann, G. B. Piccardo, and V. Trommsdorff (1995), Subduction of water into the mantle: History of an Alpine peridotite, *Geology*, *23*, 459–462, doi:10.1130/0091-7613(1995)023<0459:SOWITM>2.3.CO;2.

Schamel, S. (1974), Eocene subduction in central Liguria, Italy, Ph.D. thesis, 167 pp., Yale Univ., New Haven, Conn.

Schlunegger, F., and S. Willett (1999), Spatial and temporal variations in exhumation of the central Swiss Alps and implications for exhumation mechanisms, in *Exhumation Processes: Normal Faulting*, *Ductile Flow and Erosion*, edited by U. Ring et al., *Geol. Soc. Spec. Publ.*, *154*, 157–179.

Schumacher, M. E., and H. P. Laubscher (1996), 3D crustal architecture of the Alps-Apennines join—A new view on seismic data, *Tectonophysics*, *260*, 349–363, doi:10.1016/0040-1951(96)00046-7.

Schwartz, S., J.-M. Lardeaux, S. Guillot, and P. Tricart (2000), Diversité du métamorphisme éclogitique dans le massif ophiolitique du Monviso (Alpes occidentales, Italie), *Geodin. Acta*, *13*, 169–188, doi:10.1016/S0985-3111(00)00112-1.

Seward, D., and N. S. Mancktelow (1994), Neogene kinematics of the Central and Western Alps: Evidence from fission-track dating, *Geology*, *22*, 803–806, doi:10.1130/0091-7613(1994)022<0803:NKOTCA>2.3.CO;2.

Spandler, C., J. Hermann, and D. Rubatto (2004), Exsolution of thortveitite, yttrialite, and xenotime during low temperature recrystallization of zircon from New Caledonia, and their significance for trace element incorporation in zircon, *Am. Mineral.*, *89*, 1795–1806.

Spear, F. S. (1993), *Metamorphic Phase Equilibria and Pressure-Temperature-Time Paths*, 799 pp., Mineral. Soc. of Am., Washington, D. C.

Stacey, J. S., and J. D. Kramers (1975), Approximation of terrestrial lead evolution by a two-stage model, *Earth Planet. Sci. Lett.*, *26*, 207–221, doi:10.1016/0012-821X(75)90088-6.

Stüwe, K., and T. D. Barr (1998), On uplift and exhumation during convergence, *Tectonics*, *17*, 80–88, doi:10.1029/97TC02557.

Sun, S. S., and W. F. McDonough (1989), Chemical and isotopic systematics of oceanic basalts: Implications for mantle composition and processes, in *Magmatism in the Ocean Basins*, edited by A. D. Sanders and M. J. Norry, *Geol. Soc. Spec. Publ.*, *42*, 313–345.

Tera, F., and G. Wasserburg (1972), U-Th-Pb systematics in three Apollo 14 basalts and the problem of initial lead in lunar rocks, *Earth Planet. Sci. Lett.*, *14*, 281–304.

Tilton, G. R., W. Schreyer, and H. P. Schertl (1991), Pb-Sr-Nd isotopic behaviour of deeply subducted crustal rocks from the Dora Maira Massif, Western Alps, Italy—II: What is the age of the ultrahigh-pressure metamorphism?, *Contrib. Mineral. Petrol.*, *108*, 22–33.

Trotet, F., L. Jolivet, and O. Vidal (2001), Tectono-metamorphic evolution of Syros and Sifnos islands (Cyclades, Greece), *Tectonophysics*, *338*, 179–206, doi:10.1016/S0040-1951(01)00138-X.

Vanossi, M., L. Cortesogno, B. Galbiati, B. Messiga, G. Piccardo, and R. Vannucci (1984), Geologia delle Alpi Liguri: Dati, problemi, ipotesi, *Mem. Soc. Geol. Ital.*, *28*, 5–75.

Vavra, G., R. Schmid, and D. Gebauer (1999), Internal morphology, habit and U-Th-Pb microanalysis of amphibolite-to-granulite facies zircons: Geochronology of the Ivrea zone (Southern Alps), *Contrib. Mineral. Petrol.*, *134*, 380–404, doi:10.1007/s004100050492.

Ventura, B., G. A. Pini, and G. G. Zuffa (2001), Thermal history and exhumation of the northern Apennines (Italy): Evidence from combined apatite fission track and vitrinite reflectance data from foreland basin sediments, *Basin Res.*, *13*, 435–448, doi:10.1046/j.0950-091x.2001.00159.x.

Vernon, R. H. (1996), Problems with inferring P-T-t paths in low-P granulite facies rocks, *J. Metamorph. Geol.*, *14*, 143–153, doi:10.1046/j.1525-1314.1996.05814.x.

Vidal, O., B. Goffé, T. Parra, and R. Bousquet (1999), Calibration and testing of an empirical chloritoid-chlorite Mg-Fe thermometer and thermodynamic

data for daphnite, *J. Metamorph. Geol.*, *17*, 25–39, doi:10.1046/j.1525-1314.1999.00174.x.

Vidal, O., T. Parra, and F. Trotet (2001), A thermodynamic model for Fe-Mg aluminous chlorite using data from phase equilibrium experiments and natural pelitic assemblages in the 100°–600°C, 1 to 25 kb range, *Am. J. Sci.*, *301*, 557–592, doi:10.2475/ajs.301.6.557.

Vidal, O., T. Parra, and P. Vieillard (2005), Experimental data on the Tschermak solid solution in Fe-chlorites: Application to natural examples and possible role of oxidation, *Am. Mineral.*, *90*, 359–370.

Vignaroli, G., F. Rossetti, M. Bouybaouene, H.-J. Massonne, T. Theye, C. Faccenna, and R. Funiciello (2005), A counter-clockwise P-T path for the Voltri Massif eclogites (Ligurian Alps, Italy), *J. Metamorph. Geol.*, *23*, 533–555, doi:10.1111/j.1525-1314.2005.00592.x.

Vignaroli, G., C. Faccenna, L. Jolivet, C. Piromallo, and F. Rossetti (2008), Subduction polarity reversal at the junction between the Western Alps and the northern Apennines, Italy, *Tectonophysics*, *450*, 34–50, doi:10.1016/j.tecto.2007.12.012.

Vignaroli, G., C. Faccenna, and F. Rossetti (2009a), Retrogressive fabric development during exhumation of the Voltri Massif (Ligurian Alps, Italy): Arguments for an extensional origin and implications for the Alps-Apennine linkage, *Int. J. Earth Sci.*, *98*, 1077–1093, doi:10.1007/s00531-008-0305-4.

Vignaroli, G., C. Faccenna, L. Jolivet, C. Piromallo, and F. Rossetti (2009b), Reply to the comment by G. Capponi et al. on "Subduction polarity reversal at the junction between the Western Alps and the northern Apennines, Italy," by G. Vignaroli et al. (*Tectonophysics*, 2008, *450*, 34–50), *Tectonophysics*, *465*, 227–231, doi:10.1016/j.tecto.2008.11.007.

Villa, I. M. (1998), Isotopic closure, *Terra Nova*, *10*, 42–47, doi:10.1046/j.1365-3121.1998.00156.x.

Vissers, R. L. M., M. R. Drury, E. H. Hoogerduijn Strating, and D. Van der Wal (1991), Shear zones in the upper mantle—A case study in an Alpine lherzolites massif, *Geology*, *19*, 990–993, doi:10.1130/0091-7613(1991)019<0990:SZITUM>2.3.CO;2.

Vissers, R. L. M., E. H. Hoogerduijn Strating, M. Heijmans, and M. Krabbendam (2001), Structures and microstructures in a thrust-related, greenschist facies tectonic mélange, Voltri Group (NW Italy), *Ofioliti*, *26*, 33–46.

Wagner, G., and P. Van den Haute (1992), *Fission Track Dating*, 285 pp., Kluwer Acad., Dordrecht, Netherlands.

Watson, E. B., D. A. Wark, and J. B. Thomas (2006), Crystallization thermometers for zircon and rutile, *Contrib. Mineral. Petrol.*, *151*, 413–433, doi:10.1007/s00410-006-0068-5.

Wheeler, J., and R. W. H. Butler (1993), Evidence for extension in the western Alpine orogen: The contact between the oceanic Piemonte and overlying continental Sesia units, *Earth Planet. Sci. Lett.*, *117*, 457–474, doi:10.1016/0012-821X(93)90097-S.

Williams, I. (1998), U-Th-Pb geochronology by ion microprobe, in *Application of Microanalytical Techniques to Understanding Mineralizing Processes*, edited by M. A. McKibben, W. C. Shanks III, and W. I. Ridley, *Rev. Econ. Geol.*, *7*, 1–35.

Wolf, R. A., K. A. Farley, and D. M. Kass (1998), Modeling of the temperature sensitivity of the apatite (U-Th)/He thermochronometer, *Chem. Geol.*, *148*, 105–114, doi:10.1016/S0009-2541(98)00024-2.

F. Lisker, Fachbereich Geowissenschaften, University of Bremen, PF 330440, D-28334 Bremen, Germany.

D. Phillips, School of Earth Sciences, University of Melbourne, Parkville, Vic 3010, Australia.

F. Rossetti and G. Vignaroli, Dipartimento di Scienze Geologiche, Università Roma Tre, Largo San Leonardo Murialdo 1, I-00146 Roma, Italy. (vignarol@geo.uniroma3.it)

D. Rubatto, Research School of Earth Sciences, Australian National University, Bldg. 6, Mills Road, Canberra, ACT 0200, Australia.

T. Theye, Institut für Mineralogie und Kristallchemie, Universität Stuttgart, Azenbergstr. 18, D-70174 Stuttgart, Germany.